Deuteron and anti–Deuteron Coalescence in $Au + Au$ Collisions at $\sqrt{s_{NN}} = 200$ GeV

Marco Germinario
Niels Bohr Institute
University of Copenhagen

November, 2003

Thesis presented for the Cand. Scient. degree (Master of Science).
Supervisor: Jens Jørgen Gaardhøje

This work is dedicated to my family,
Raffaele Monachesi and Armando Foglio Para.

Acknowledgments

This work marks the end of a very important period of my life. Along this time, I met very special people in Italy and here in Denmark. First, I wish to thank my Italian friends: Valerio, Max and Carlo, who have been, and continue to be, a part of my life. Also Patrizia, who made me see the world in a different way for the first time. In regards to danish friends, I wish first of all to thank Rina, who is one of the persons who most positively influenced me in my life. Thanks to her. Also, Marie Louise, with our friendship we supported each other and grew together in the last 5 years. Thanks to Silvia, Mark, Chiara, Rune, Fabrizio, Stine, Louise, Giorgia, Stefano, Denise, Borja, Jaime, Jose' Alberto, Eduardo, the "old five" kitchen in Egmont, Enrico, Julia and all the others.

A special thank goes to the HEHI group at the Niels Bohr Institute, where I learned what team work is. Special thanks to my supervisor, J.J. Gaardøje, who was always willing to support me and give new, exciting directions to my work. A very special thank to Claus Jørgensen, Djamel Ouerdane and Peter Christiansen for their support and Christian Holm, Ian Bearden, David Sandberg, Boris Tomasik, Jakob Bondorf, Ralf Rapp.

Finally I wish to thank Direktør Ib Henriksens Fond, Ølhander Carl Pedersen og hustrus legat and my family (Milano and Canosa) for the financial support.

Copenhagen, November 2003

Marco Germinario

Preface

The goal of studying ultra–relativistic heavy ion collisions is to explore and understand the properties of matter at extreme temperatures (10^{12} degrees) and densities (more than ten times normal nuclear matter density). The Universe is believed to have been in this state during the first microseconds after the Big–Bang. In such conditions, lattice QCD (Quantum Chromodynamics) predicts the transition from a hadron gas to a quark–gluon plasma phase, where quarks and gluons are no longer confined inside hadrons, but move freely inside a large dense zone.

The Relativistic Heavy Ion Collider (RHIC), located at Brookhaven National Laboratory, Long Island (USA), was built to study nuclear matter at extreme energy density and temperature. During the summer and fall 2001 gold ions were collided at speeds reaching the speed of light and at the center of mass energy $\sqrt{s_{NN}} = 200$ GeV. This is the highest center of mass energy achieved so far by an heavy ion accelerator. The analysis of this work is based on the data taken from that run collected with the BRAHMS detector.

Since the high energy density state ($\gtrsim 1$ GeV/fm^3) of interest lasts only $\sim 10^{-23}$ seconds after the collision, the study of the collision dynamics is done by measuring the final state particles.

The Broad RAnge Hadron Magnetic Spectrometer (BRAHMS) at RHIC has the unique feature among the RHIC experiments to measure charged hadrons over a broad range of rapidity and transverse momentum (-0.1 $< y_\pi <$ 4 and 0.1$< p_T \lesssim$ 5 GeV/c). The particles of interest for this work are (anti–)protons and (anti–)deuterons.

The subject of this thesis is particle *coalescence*. The collision zone is seen as a “fireball”, a very hot and dense volume of matter hadronic matter expanding until the particles stop interacting at the so–called kinetic freeze–out. This occurs at a temperature $T \approx 100 - 130\,\mathrm{MeV}$. At this point, the temperature is low enough to give those protons and neutrons that are close enough in phase–space a chance to coalesce into deuterons. The binding energy is roughly 2.2 MeV. The coalescence model provides information about the size of the fireball at freeze–out from the measured proton and deuteron spectra.

Thus, measuring (anti–)proton and (anti–)neutron coalescence leads to an estimation of the reaction volume and also of the energy density at kinetic freeze–out.

In the first chapter, some basic notions in relativistic heavy ion collisions are given and some of the latest RHIC results are shown. Chap. 2 introduces the coalescence model. In Chap. 3, RHIC and BRAHMS are described. Chap. 4 gives a general introduction of the first part of data analysis i.e. event characterization, track construction and particle identification. Chap. 5 is an analysis of how invariant transverse momentum spectra are constructed and details are given on the various necessary corrections due to the limited spectrometer acceptance and particle contamination from secondary interactions. In Chap. 7 the (anti–)protons and (anti–)deuterons spectra are presented. The coalescence model is applied and the results are compared with other experiments at different energies. A rough estimate of the energy density at the calculated freeze–out volume is also given. Conclusions are drawn in Chap. 8.

The results presented here are preliminary, and as such, not official published BRAHMS results. Before quoting the results please contact the author[1] and the spokesmen[2] of the BRAHMS collaboration.

Research carried out in part at the Relativistic Heavy Ion Collider, Brookhaven National Laboratory, which is supported by the U.S. department of Energy, Division of Nuclear Physics of the Office of Science, under contract with BNL (No. DE-AC02-98CH10886).

[1]germina@nbi.dk
[2]Flemming Videbæk, videbaek@bnl.gov and Jens Jørgen Gaardhøje, gardhoje@nbi.dk

Contents

List of Figures

List of Tables

Chapter 1

Quark Gluon Plasma and Relativistic Heavy Ion Collisions

In this chapter, the fundamental notions on relativistic heavy ion collisions are introduced, namely the Standard Model, Quark Gluon Plasma (QGP), nuclear phase diagram, collision dynamics and space time evolution of the collision.

The second part presents the most recent results from the RHIC experiments.

1.1 The Standard Model

The Standard Model is a theory that describes elementary particles and their interactions. In this model, there are only a few “building blocks”, including **6 quarks**, **6 leptons** and **the carriers of the interactions**.

FERMIONS matter constituents spin = 1/2, 3/2, 5/2, ...

Leptons spin = 1/2			Quarks spin = 1/2		
Flavor	Mass GeV/c^2	Electric charge	Flavor	Approx. Mass GeV/c^2	Electric charge
ν_e electron neutrino	$<1\times10^{-8}$	0	u up	0.003	2/3
e electron	0.000511	−1	d down	0.006	−1/3
ν_μ muon neutrino	<0.0002	0	c charm	1.3	2/3
μ muon	0.106	−1	s strange	0.1	−1/3
ν_τ tau neutrino	<0.02	0	t top	175	2/3
τ tau	1.7771	−1	b bottom	4.3	−1/3

	Gravity	Weak (Electroweak)	Electromagnetic (Electroweak)	Strong
Carried By	Graviton (not yet observed)	$W^+ W^- Z^0$	Photon	Gluon
Acts on	All	Quarks and Leptons	Quarks and Charged Leptons and $W^+ W^-$	Quarks and Gluons

Figure 1.1: Leptons, quarks and the carriers of the interactions.

Leptons and quarks are *fermions* i.e. they have an odd–half integer spin and follow the Pauli exclusion principle. Figure 1.1 depicts the different types of leptons and quarks, including mass and charges. Note that both quarks and leptons exist in three distinct sets. These sets are referred to as “generations”. All observed matter in the Universe is made of the first generation of particles, for example up quarks, down quarks, and electrons.

The heaviest leptons, the muon and the tau, are not found in ordinary matter. This is because all second and third generation particles are unstable and decay into the stable first generation through weak interaction. Thus, fundamental particles can decay only into other fundamental particles.

It is important to note that there are conservation laws that must be respected. In the case of leptons, the electron, muon and tau numbers, are always conserved. It is still unknown why the two unstable generations exist, and why the world we observe seems only to be made of matter and not anti–matter.

Only bound states of quarks are observed. Composite particles made of quarks are called **hadrons**. Although individual quarks have fractional electrical charges, they combine such that hadrons have a net integer electric charge.

The two most important classes of hadrons are **baryons** and **mesons**, illustrated in figure 1.2. Furthermore the **pentaquark** has been recently discovered. It is a hadron composed of 4 valence quarks and one valence anti–quark (see [1]).

Baryons qqq and Antibaryons $\bar{q}\bar{q}\bar{q}$

Baryons are fermionic hadrons.
There are about 120 types of baryons.

Symbol	Name	Quark content	Electric charge	Mass GeV/c^2	Spin
p	proton	uud	1	0.938	1/2
$\bar{p}$	anti-proton	$\bar{u}\bar{u}\bar{d}$	–1	0.938	1/2
n	neutron	udd	0	0.940	1/2
Λ	lambda	uds	0	1.116	1/2
Ω^-	omega	sss	–1	1.672	3/2

Mesons $q\bar{q}$

Mesons are bosonic hadrons.
There are about 140 types of mesons.

Symbol	Name	Quark content	Electric charge	Mass GeV/c^2	Spin
π^+	pion	$u\bar{d}$	+1	0.140	0
K^-	kaon	$s\bar{u}$	–1	0.494	0
ρ^+	rho	$u\bar{d}$	+1	0.770	1
B^0	B-zero	$d\bar{b}$	0	5.279	0
η_c	eta-c	$c\bar{c}$	0	2 .980	0

Figure 1.2: Baryons, mesons and respective anti–particles.

Baryons (e.g. protons and neutrons) contain three valence quarks, whereas mesons contain one quark and one anti–quark, making them unstable. However, the kaon lives longer than most other mesons. It is therefore called "strange" and actually carries the strange quark. Only a very small part of the mass of a hadron is due to the constituent quarks, the majority is attributed to their kinetic energy.

Interactions between particles are mediated by several forces, including **gravity** (not included in the standard model), **weak**, **electromagnetic** and **strong** forces. Each of these interactions has its respective carrier particle, which are shown in figure 1.1.

Interaction carriers are bosons, i.e. they have an integer spin and are not subject to the Pauli exclusion principle. The electromagnetic force acts between electrically charged particles. It allows for example atoms to bind and form molecules. The weak interaction is responsible for the decay of massive quarks and leptons into lighter ones. The strong interaction is responsible for nucleon stability (residual strong force), which at quark level means confinement by color interaction (gluon exchange between quarks – see next section). The theory that describes the strong interaction between quarks and gluons is **Quantum**

Chromo Dynamics (QCD).

1.2 QCD, Quark Gluon Plasma and Nuclear Phase Diagram

The QCD theory assigns quarks and gluons a new quantum number, described as the *color charge*. Each quark has a color (red, green, blue,) and each anti–quark an "anti–color" (anti–red, anti–green, anti–blue). Color–charged particles cannot exist individually. Furthermore, only systems of quarks which are "colorless" can be observed. Hence, the system will either have all three colors (baryon) or a color and anti–color (mesons). This explains why only baryons and mesons have been observed so far.

The fact that gluons carry color charges gives rise to a color self–interaction, leading to a "running" coupling constant α_s, which depends on the momentum transfer involved in the strong process. By looking at figure 1.3, it can be seen that α_s depend on the momentum transfer in the strong interaction. If the momentum transfer between the quarks decreases, due to large distances, α_s increases, and the quarks become more tightly bound. At short distances or large momentum transfer, however, α_s approaches to zero. At that point, two quarks hardly experience the strong force between each other, and reach the *asymptotic freedom*.

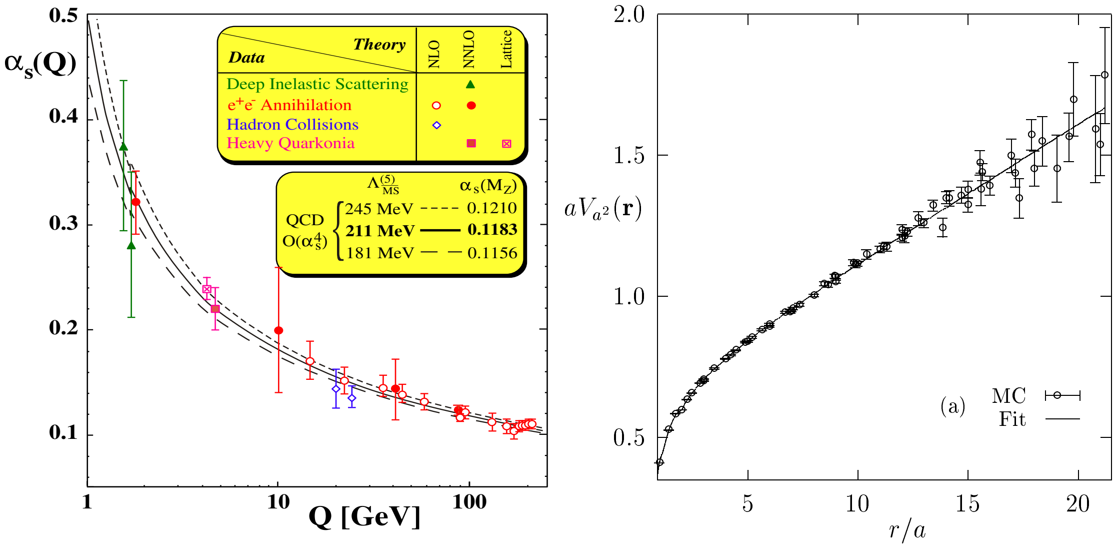

Figure 1.3: Left: Experimentally determined values of strong coupling constant α_s as a function of the momentum transfer Q (figure taken from [2]). Right: Quark–quark potential as a function of their relative distance. The parameter a is the string tension (figure taken from [3]).

The picture on the right panel of figure 1.3 shows the form of the potential between two heavy quarks as a function of their relative distance. If one tries to separate two quarks, the potential between them increases, counteracting the separation, or color confinement. If the distance becomes large (quarks are separated) more and more energy is added to the color–force field as the quarks are pulled apart. At some point, it is energetically “cheaper” for the color–force field to “snap” into a new quark-anti–quark pair. In so doing, energy is conserved because the energy of the color field is converted into the mass of the new quarks. The color field formed between the quarks breaks up forming new hadrons. This is the reason why it is impossible to observe “free” quarks.

This issue can be partially solved by studying the coupling constant α_s and the form of the potential between quarks. Figure 1.3 demonstrates that if the distance between quarks is very small then the binding force nearly vanishes.

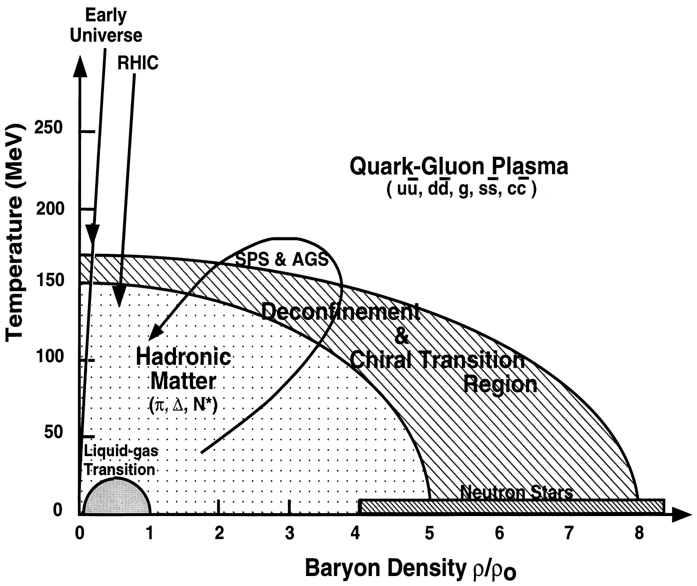

Figure 1.4: Schematic phase diagram of nuclear matter [4]. Nuclear density ρ_0 is approximately 0.15 baryons/fm^3.

The solution is therefore to collide protons and neutrons together at high energies in a small volume to bring quarks as close as possible. The goal is to obtain a state in which quarks and gluons can move freely relative to each other.

This predicted new state of matter is called *Quark Gluon Plasma* (*QGP*). Figure 1.4 shows a schematic phase diagram of nuclear matter. The behavior of nuclear matter as a function of temperature and density is described by its equation of state.

Conventional nuclear physics is concerned primarily with the lower left portion of the diagram which portrays lower temperatures and near normal nuclear matter density. At low excitation energies, a liquid–gas phase transition is expected to occur. This is the focus of experimental studies using low energy heavy ion collisions ($E \sim 10\,\mathrm{MeV}$).

At somewhat higher excitation, nucleons are excited into baryonic resonance states, favoring particle production (mostly pions). This region has been accessible in heavy ion studies at the SIS and AGS accelerator facility at BNL and at SPS at CERN. As illustrated in figure 1.4, some part of these collisions may traverse the transition region into the quark–gluon plasma regime, which is the major focus of the Relativistic Heavy Ion Collider (RHIC) and associated experiments.

Knowledge of heavy ion collisions therefore allows a better understanding of the properties of nuclear matter when far from its stable state. The region of high baryon densities and very low temperatures is important for understanding various aspects of stellar evolution. The nuclear matter equation of state explains partially neutron star collapse and supernova expansion dynamics. The region of low baryon densities and very high temperatures is closer to the conditions prevailing in the early Universe. RHIC experiments aim to reproduce these conditions.

The transition from quark to hadron phase is predicted to have occurred at approximately ten micro–seconds after the Big Bang, when the quarks and gluons were glued into new composite particles (hadrons). The critical temperature at which the transition should take place is predicted by lattice QCD calculations, and is between 150–200 MeV (10^{12} Kelvin) [5].

The temperatures achieved in collisions at RHIC are in the same order of magnitude as the predicted critic temperature [6]. The duration of the predicted QGP is 10^{-23} s in the laboratory and 10^{-6} s for the early Universe.

1.3 Heavy Ion Collisions and Collision Dynamics

One of the goals of RHIC is to produce a quark–gluon plasma state, and study its properties and subsequent hadronization.

RHIC is a *collider* i.e. a storage and accelerator ring in which colliding nuclei move at the same speed in opposite directions so that all incident energy is available for bringing the colliding matter into a highly excited state.

In table 1.1 the different energies achieved from the different accelerators are shown. For a reference to the relativistic gamma factor γ see B, equation B.1.

Accelerator	E_{beam}^{max} [AGeV]	$\sqrt{s_{NN}}$ [GeV]	γ_{cm}
AGS(BNL)	10	5	2
SPS(CERN)	160	17	9
RHIC(BNL)	100+100	200	100
LHC(CERN)	2 x 5500	11000	5500

Table 1.1: Accelerators status and energies for heavy systems.

To characterize the "violence", or centrality of the collision, the *participant–spectator model* is generally used (see figure 1.5). The nucleons outside the overlapping region of the two nuclei are called *spectators*. The nucleons that participate in the collision are the *participants*. The number of participants is related to the *impact parameter* b, which is the transverse distance between the centers of the initial nuclei. A small impact parameter leads to many participants nucleons. Experimentally, b is not measured, and researchers often refer to a centrality percentage (see 4.2.1).

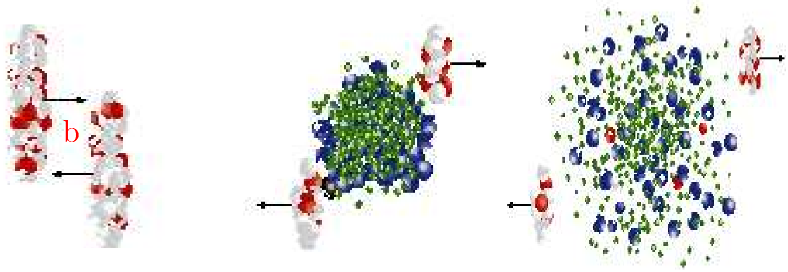

Figure 1.5: The Participant–Spectator Model.

The centrality is experimentally determined by evaluating the *multiplicity*, which is the number of final state particles detected. A high multiplicity corresponds to a central event whereas a low multiplicity is characteristic of a peripheral collision. Hence, by investigating a large set of events, one can identify events within a given centrality range.

1.3.1 Space Time Evolution of the Collisions

The space–time evolution of the collision strongly depends on the energy of the colliding nuclei. Two models are generally used: the full stopping scenario and the transparent scenario.

At low or intermediate energies ($\sqrt{s_{NN}}$ = A 5-10 GeV) the participants are partly or fully stopped in the collision, and all the available kinetic energy for the colliding nuclei is converted into internal degrees of freedom in the collision zone. This is the Landau model, illustrated in figure 1.6. The degree of stopping is examined by measuring the net–baryon density in the mid–rapidity region and the average rapidity (see appendix B for definition) loss of the primary nucleons.

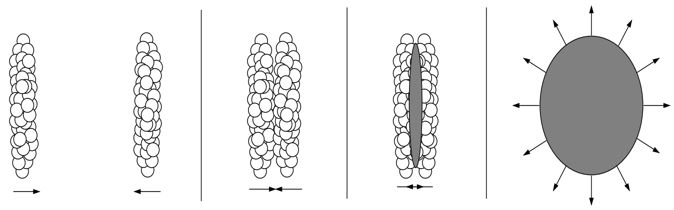

Figure 1.6: Landau scenario: central collision with high degree of stopping. The "pan–cake" shape of the ions is due to the relativistic effects (Lorentz contraction) at high velocities (see appendix B).

The collision zone is often referred as the *fireball*. This is the region where the quark–gluon plasma is supposed to occur if the energy density is high enough. After the eventual quark–gluon plasma formation, a cooling phase follows in which quarks will recombine into hadrons.

At higher energies ($\sqrt{s_{NN}} \geq 100$ A GeV) the *Bjorken* model is thought to be appropriate, where the nuclei are expected to inter-penetrate. In this model the reaction is characterized by a high degree of transparency.

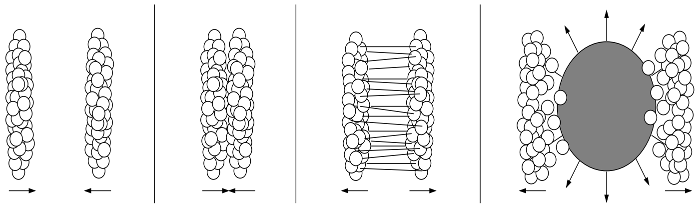

Figure 1.7: Schematic view of Bjorken scenario (collision with high degree of transparency). The two colliding nucleons looses only a fraction of their kinetic energy during the initial interaction of the nuclei. The excited color–charged field created condensates and gives rise to a region of hot, dense matter.

In the transparent scenario the two nuclei interpenetrate and a highly excited color field is built up in the intermediate zone (see figure 1.7). As the distance grows, the field will break up and produce a large number of $q\bar{q}$ pairs and gluons, possibly formed in a quark–gluon plasma phase. The system then expands and cools off and eventually freezes–out. For Au+Au collisions at $\sqrt{s_{NN}} = 200$ A GeV the predicted scenario is dominantly transparent (see [7] for a recent study on stopping at RHIC energies).

1.4 Recent Results from RHIC

1.4.1 Nuclear Stopping

The study of nuclear stopping in heavy ion collisions provides information on the dynamics of the collision. The measure of the rapidity distribution of the final state net–baryon over the full rapidity range rapidities, permits the quantification of the stopping degree [8]. Figure 1.8 shows a very recent comparison of energy systematics of the net–proton yields measured at AGS, SPS and RHIC in the most central heavy–ion collisions.

Almost full stopping is observed in Au+Au collisions at AGS energies ($\sqrt{s_{NN}} = 5$ GeV). In collisions between Pb at SPS energies, $\sqrt{s_{NN}} = 17$ GeV, transparency begin to set in, and systematics suggest that a maximum baryon density occurs at intermediate energies between AGS and SPS. At RHIC energies, a minimum (dN/dy net–protons = 6.4 [7]) over a broad rapidity range is observed at mid–rapidity, revealing the highest transparency.

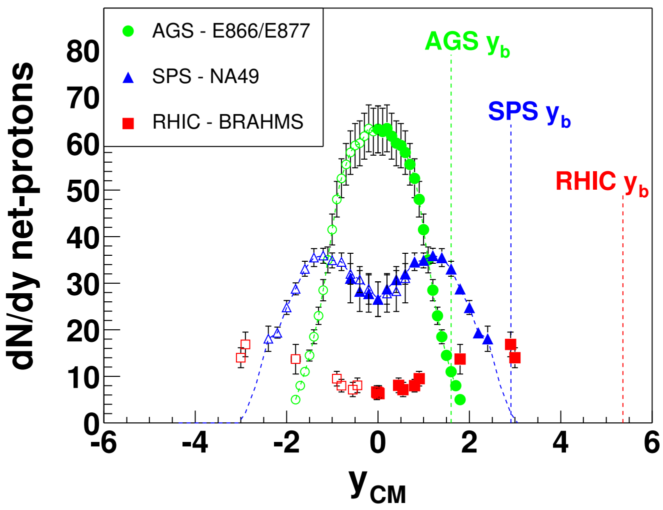

Figure 1.8: Net–proton yields at rapidity densities measured at AGS, SPS and RHIC. The data has been reflected around $y = 0$ (picture taken from [7]).

1.4.2 Ratios of Charged Particles

Another interesting aspect of heavy ion collision is the study of the ratios of yields of anti–particles to particles. In particular, the rapidity dependence of such ratios provides significant informations about the dynamic of the collision.

The ratio $N(\bar{p})/N(p)$ describes the transparency of the collision. Because of baryon number conservation, an equal number of particles and anti–particles are created in the collision. Therefore, if the ratio $N(\bar{p})/N(p)$ is less than one at mid–rapidity, it means that some of the primary nucleons have been stopped. In contrast, a $N(\bar{p})/N(p)$ close to one means high transparency. Figure 1.9 shows anti–particles to particles ratios as a function of center of mass energy (left) and rapidity (right). An increase in the transparency of the collision with the center of mass energy is observed. The ratios in figure 1.9 (right) are (within the range of errors) constant in the rapidity range $0 \lesssim \mathrm{y} \lesssim 1$. This is consistent with a boost invariant plateau scenario dominated by particle production from the color field. A decrease of $N(K^-)/N(K^+)$ and $N(\bar{p})/N(p)$ ratios toward forward rapidities is also observed. This agrees with the statistical model calculations, where the baryon chemical potential decreases dramatically from higher rapidities. A small value of chemical potential indicates a small–net baryon density at mid–rapidity.

1.4.3 QGP Signatures

If a QGP phase occurs, its lifetime is in the order of 10^{-23} s – a duration that forbids direct observation of such a phase. Thus only indirect indications from the plasma, the so–called *signatures*, can provide insights of such a phase.

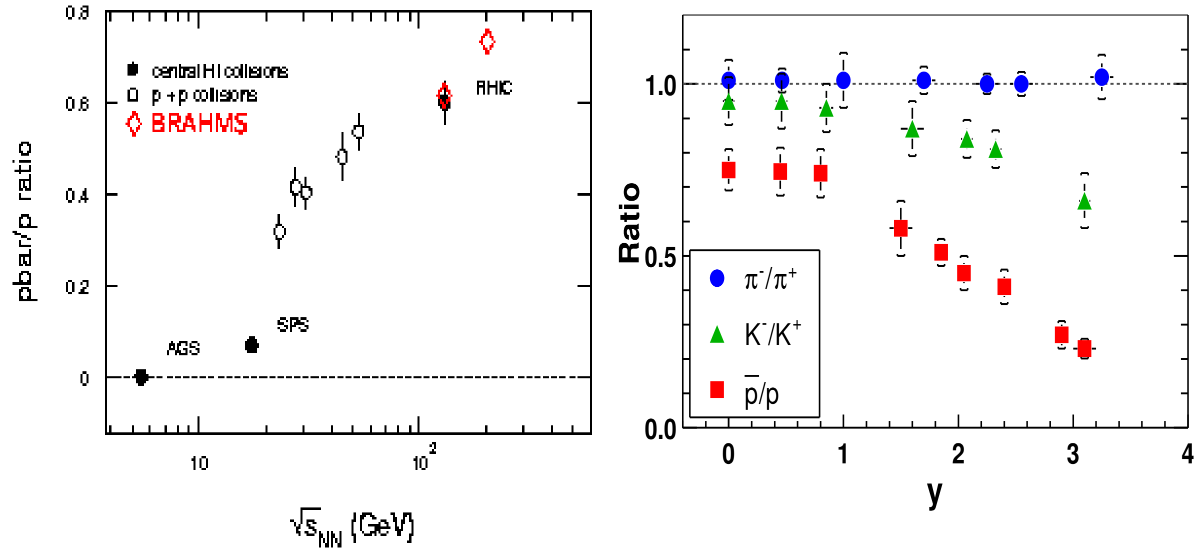

Figure 1.9: $N(\bar{p})/N(p)$ ratios at mid–rapidity as a function of center of mass energy for different experiments (left) and $N(\pi^-)/N(\pi^+)$, $N(K^-)/N(K^+)$ and $N(\bar{p})/N(p)$ ratios as a function of rapidity measured by BRAHMS experiment at $\sqrt{s_{NN}} = 200$ GeV (right). The figures are from [9] and [10] respectively.

High–p_T Jet Suppression

Most hadrons with high transverse momentum (more than 2 GeV/c) are produced in hard processes i.e. initial collisions between primary nucleons. From small collision systems like pp, $p\bar{p}$, e^+e- these *jets* of highly energetic particles can be observed. For large collision systems, one should expect a *suppression* of high p_T particles due to an eventual phase–transition, where the highly energetic quarks are slowed by traversing a very dense medium, eventually a QGP. This effect could be seen as a signature of a QGP phase transition.

Figure 1.10 shows high p_T suppression measured by BRAHMS at two different locations in the rapidity space ($y = 0$ and $y \sim 2$) for Au + Au collisions at $\sqrt{s_{NN}} = 200$ GeV/c. From the figure one can argue that the suppression of high p_T particles at these conditions extends at least until $\eta \sim 2.2$.

Lattice QCD

Figure 1.11 shows the results of a lattice QCD calculation using two light quark flavors. Plotted are the energy density ϵ/T^4 (circles) and the pressure P/T^4 (squares) as a function of the temperature T. If a first order phase transition occurs, a rapid rise in the effective numbers of degrees of freedom, expressed by ϵ/T^4 or P/T^4, should be observed over a small variation of T, around T_c.

In the figure a phase transition is observed in the calculation at $T \approx 150$ MeV. The experimentally charged multiplicity can be related to the initial entropy of the system.

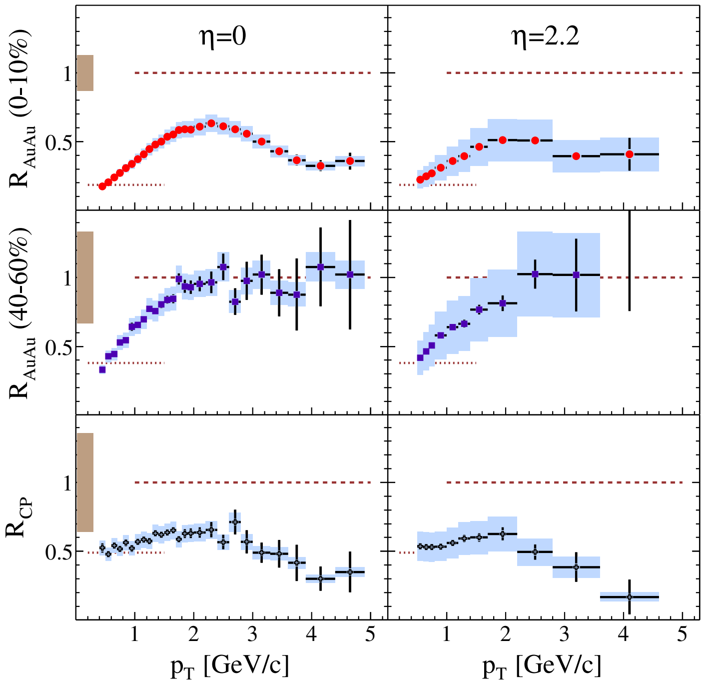

Figure 1.10: High p_T suppression measured by BRAHMS at mid–rapidity and rapidity ~ 2 for Au+Au collisions at $\sqrt{s_{NN}} = 200$ GeV/c. The panels in the bottom show the ratio between the nuclear modification factors from the first and second panels. The nuclear modification factor is a scaling factor which takes into account the fact that the number of hard scatterings is proportional to the number of binary collisions (figure from [11]).

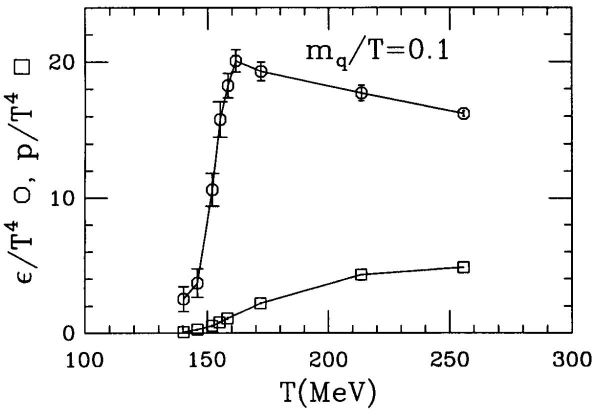

Figure 1.11: Lattice QCD calculations based on light quarks flavors. The circles shows the energy density and the squares the pressure as a function of the temperature [12].

Strangeness Production

Enhanced abundance of strange hadrons (hadrons containing strange quarks as for example kaons) after collision as been proposed as an indicator for the formation of QGP [13].

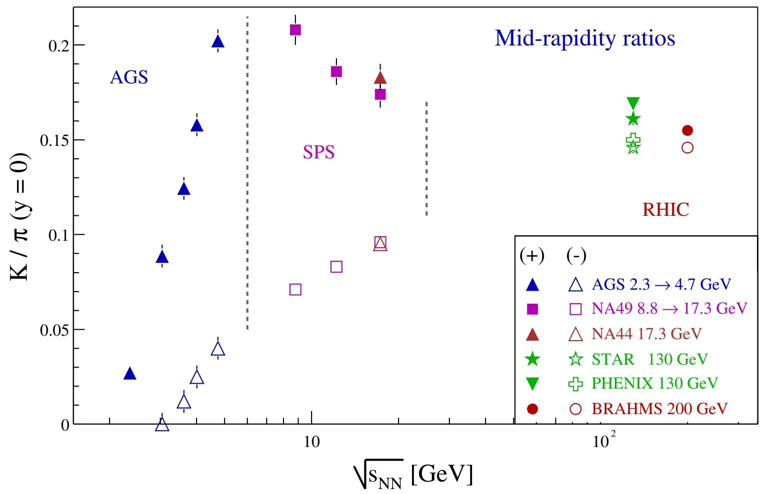

Figure 1.12: Positive and negative kaon to pion ratio for different beam energy at mid–rapidity [14].

In relativistic heavy ion collisions, the initial state particles are nucleons made of u and d quarks (the constituents of the two colliding nuclei), so all strange matter detected must have been produced in the collision. Gluon fusion causes the emission of quarks, anti–quarks pairs. More energetic gluon pairs are able to emit more energetic (massive) quark pairs. The gluons in the QGP, being much more energetic than gluons found in average matter, are able to emit the more massive strange, anti–strange quark pairs. Furthermore, strangeness production is more energy convenient in a QGP phase (production of strange quark-anti–quark pairs) than in a hadron phase, where kaons (the lightest hadrons containing strangeness) production requires much more energy. Thus, if the QGP has been produced, strangeness enhancement should be observed.

A large enhancement of multi strange anti–baryons (strange baryons are also called also *hyperons*) is proposed as characteristic, and a nearly background–free signature of QGP [15]. Such a systematic enhancement has in fact been observed, depending on the strangeness content of the studied hyperon specie [16]. Another way to examine strangeness enhancement is to study the mesons (anti–)kaon (containing strangeness) to (anti–)pion (which do not contain strangeness) multiplicity ratios and therefore characterizes strangeness production.

Figure 1.12 shows one of the recent measurements of kaon to pion ratios. An increase of the anti–particles ratio can be observed at low beam energies. For positive particles there is a saturation peak at AGS–SPS energies (rapidity zero) due the presence of primary baryons, which favors “associated strangeness production” (see [14]).

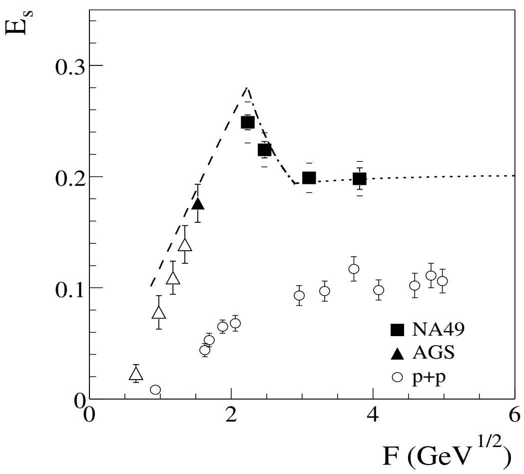

Figure 1.13: Comparison between predicted statistical model and experimental data of energy systematics of strangeness to entropy ratio as a function of the *Fermi variable* F, which is proportional to the total entropy before expansion (figure from [17]).

The positive and negative ratio at 200 GeV at mid–rapidity are within the range of statistical errors from 130 to 200 GeV, and seem not to change dramatically from top SPS to RHIC energies. Thus, a strangeness saturation appears to be reached, with respect to light flavors.

In the Statistical Model of Early Stage (SMES) [18] quark and gluons are used as degrees of freedom of a QGP phase in statistical equilibrium. The aim is to compare the evolution of entropy as a function of the center of mass energy to data, with and without the assumption of QGP phase–state and to see whether the strangeness to entropy ratio exhibits a discontinuity as the center of mass energy increases. Figure 1.13 shows the energy systematics of strangeness to entropy ratio predicted using the statistical model of the early stage.

Charmonium Suppression

Bound states of charm and anti–charm ($c\bar{c}$) quarks are generally referred to as *charmonium* (J/ψ). The production of this meson in a quark–gluon plasma is predicted to be suppressed [19]. This is a result of the "Debye" screening of the color interaction in a $c\bar{c}$ pair, initially formed in the QGP by fusion of two incident gluons [20].

Identification of J/ψ is done indirectly by analyzing its decay products. This require high accuracy in vertex determination. This has not been measured at RHIC yet, but will be by the PHENIX experiment in run IV. Figure 1.14 shows results from the NA50 (SPS) experiment. The horizontal line at one shows J/ψ production prediction based on data for small collision systems. A clear suppression of J/ψ production can be seen above $\epsilon \sim 2.3$ GeV/fm^3.

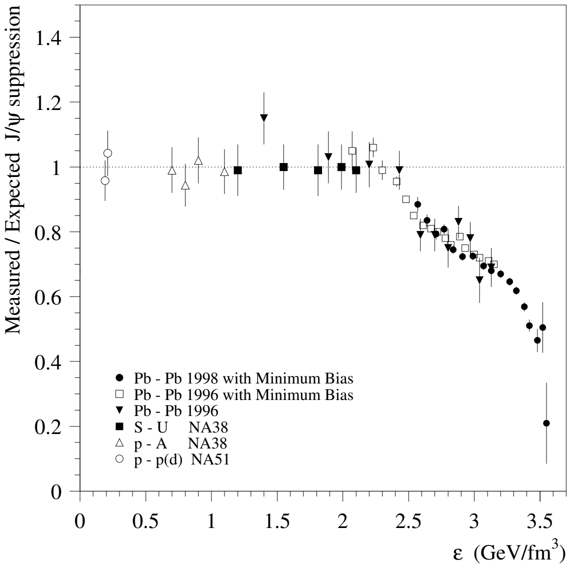

Figure 1.14: J/ψ suppression from NA50 measurements at SPS.

Other signatures

There are other kinds of indirect signatures which offer informations about the existence of QGP: electromagnetic probes (dileptons, direct photons), disoriented chiral condensates, exotic signals, etc. However, no clear signals from these probes have been found yet.

Chapter 2

Coalescence

In order to study intensive variables such as energy and entropy densities knowledge of the system volume is necessary. Coalescence and HBT (Hanbury Brown–Twiss, which is two–particle Bose Einstein interferometry) are methods to study volumes in the late stages of the expansion. In this chapter different models of light cluster formation are presented.

2.1 Coalescence

As previously explained, the collision zone is described as a "fireball", a very hot and dense volume of matter expanding until the particles stop interacting at the so–called kinetic "freeze–out" (T≈100-130 MeV). At this point, the temperature is low enough to give protons and neutrons (close enough in phase space) a chance to coalesce into deuterons, which binding energy is $\sim$ 2.2 MeV. Because deuterons have "low" binding energy and follow energy–momentum conservation, deuterons must be formed at kinetic freeze–out. Furthermore deuteron production is also sensitive to the nucleon density. Likewise anti–deuteron depends on the production and annihilation of anti–protons and anti–neutrons.

Therefore by measuring (anti–)proton and (anti–)deuteron yields it is possible to get information about the size and dynamics of the source at freeze–out. The relation to volume must be proceeded via a comparison to a model.

The *coalescence parameter* B_2 characterizes the probability that two nucleons with similar momentum form a bound state:

$$B_2 = \frac{(E_d \frac{d^3 N_d}{dp_d^3})}{(E_p \frac{d^3 N_p}{dp_p^3})^2} \propto \frac{1}{V} \tag{2.1}$$

where d^3N_d/dp_d^3 and d^3N_p/dp_p^3 are the deuteron, proton density in momentum space respectively, and E_d, E_p the deuteron and proton energies respectively. V is the volume of the source size at freeze–out (under conditions of thermodynamical equilibrium), assuming that proton and neutron spectra have at least the same form.

The main characteristics of the coalescence models are:

- As a consequence of energy–momentum conservation, deuterons (light nuclei in general) cannot be formed by scattering nucleons in free space. The formation of the two bound nucleons state requires the presence of a third body to conserve energy and momentum (e.g. it could be a pion in the process $p+n+\pi \rightarrow d+\pi$.).

- Because of the small binding energy of the deuteron (2.2 MeV) compared to typical energies of the particles in the fireball (GeV), deuterons can survive only when the probability for collisions within the expanding source is very small i.e. at kinetic freeze–out temperature ($\sim$ 100 MeV).

- The formation of a bound state is sensitive to the presence of correlations between the space–time and momentum vectors of the coalescing nucleons, because of their large masses. Thus from a coalescence model which includes the dynamic of the source (collective flow) it is possible to get information about the flow and density profile of the source.

2.2 Simple Coalescence Model

The first time that light nuclei production and source size were related was in 1960. The idea was that the probability of deuterons formation was proportional to the interaction volume of the collision [21].

The first model was developed in 1963 [22]. In this model, the proton–neutron pair interacts with the static nuclear optical potential and due to the two–body strong force, binds together to form a deuteron.

$$\gamma \frac{d^3 N_d}{d\overrightarrow{p}_d^3} = B_2 \gamma \frac{d^3 N_p}{d\overrightarrow{p}_p^3} \gamma \frac{d^3 N_n}{d^3 \overrightarrow{p}_n^3} \tag{2.2}$$

where $\overrightarrow{p}_d$ is the deuteron momentum, $\overrightarrow{p}_p$ is the nucleon momentum and γ is the relativistic factor. In this model B_2 is thought to represent the binding energy and the nuclear optical potential of the nucleus. Equation 2.2 shows that the deuteron density in momentum space is proportional to the proton density times the neutron density at the same momentum per nucleon.

Because of the fact that most experiments, especially BRAHMS, only measure charged particles, neutron and proton distributions are assumed to be identical[3]:

$$E_d \frac{d^3 N_d}{d\overrightarrow{p}_d^3} = B_2 (E_p \frac{d^3 N_p}{d\overrightarrow{p}_p^3})^2 \tag{2.3}$$

An extension of this model was made by A. Schwarzschild and C. Zupancic (see [23]) by generalizing equation 2.2 within a small momentum sphere to clusters produced in nucleus–nucleus collisions:

[3]From now on the invariant form is used, knowing that $E = \gamma m$

$$E_A \frac{d^3 N_A}{d\overrightarrow{p}_A^3} = B_A (E_p \frac{d^3 N_p}{d\overrightarrow{p}_p^3})^A \tag{2.4}$$

Where A is the cluster mass, $\overrightarrow{p}_A = A\overrightarrow{p}_p$ is the total momentum of the cluster. B_A is given by equation 2.6. Infact, if one considers a momentum sphere with radius p_0, the probability of finding a nucleon in this sphere is:

$$P = \frac{1}{M}\frac{4\pi}{3}p_0^3 \frac{d^3 N_N}{d\overrightarrow{p}^3} \tag{2.5}$$

where M is the mean nucleon multiplicity. If one assumes $M \gg 1$, $M \cdot P \gg 1$ (mean number of nucleons in the sphere is small), that the cluster is small compared to the number of nucleons ($A \ll M$), and taking into account spin and isospin (see [24] for details), B_A will have the following expression:

$$B_A = \frac{2s_A + 1}{2^A}\frac{1}{N!}\frac{1}{Z!}(R_{np})^N (\frac{4\pi}{\gamma 3 m_p} p_0^3)^{A-1} \tag{2.6}$$

where N and Z are the number of neutrons and protons in the cluster, R_{np} is the ratio of neutrons to protons participating in the collision, s_A is the cluster spin and m_p the proton mass. This model assumes that the proton and and neutron densities are the same except for the proportionality factor R_{np}.

Equation 2.6 shows the relationship between the proportionality constant, B_A, momentum densities, and the momentum space volume of radius p_0. The idea is that if two nucleons have a small relative momentum (within the range of p_0), they can fuse or *coalesce* together to form a bound state.

However, this model does not give information about the dynamics of nucleon clustering and it is not even possible to extract any useful dynamical information from it, such as nuclear matter properties and its relation to clustering dynamics. Furthermore, the first results at AGS energies gave lower values of coalescence parameters than previous measurements.

Therefore the following important inference was made: clusters are formed by a statistical coalescence during the breakup (freeze–out) of the fireball [25]. In fact light nuclei are relatively large objects with small binding energies compared to the mean energy in the source. The deuteron e.g. has a rms radius of $R_{rms} = 2.1\ fm$ and a binding energy E_b of 2.2 MeV. Considering that a highly interacting source before freeze–out has a temperature above 100 MeV, the observed deuterons (clusters) must be formed near freeze–out, where they can survive and leave the system.

Then, the distribution of nucleons in phase space, assumed to be position independent in a volume V, is:

$$f(p) = \frac{(2\pi)^3}{V}\frac{d^3 N_p}{d\overrightarrow{p}^3} \tag{2.7}$$

By calculating the phase space distribution of a cluster of a mass A using equation 2.7, one obtains the same equation as 2.4 but with a different definition of B_A

$$B_A = \frac{2s_A + 1}{2^A} \frac{1}{N!} \frac{1}{Z!} (R_{np})^N [\frac{(2\pi)^3}{\gamma m_p V}]^{A-1} \tag{2.8}$$

which shows that the coalescence parameter B_A is related to the source volume as $B_A \propto (1/V)^{A-1}$.

One can establish a relationship between the phenomenological parameter p_0 and the volume of the system V by comparing equations 2.8 and 2.6:

$$\frac{4}{3}\pi p_0^3 \sim \frac{(2\pi)^3}{V} \tag{2.9}$$

this means that a measurement of the intrinsic coalescence momentum radius p_0 is in fact a measurement of the volume of the source, at the time of cluster formation.

2.3 Density Matrix Model

The previous models were improved by accounting for some of the quantum mechanical aspects of coalescence [26]. The particle distributions are represented by density matrices and the wave functions of the particles are assumed to be Gaussian in shape. By considering the internal coalescence volume in momentum space, $4/3 \cdot \pi p_0^3$, the coalescence parameter for a fragment of a mass A is:

$$B_A = \frac{2s_A + 1}{2^A} (R_{np})^N A^{3/2} (4\pi \frac{\nu_A \nu}{\nu_A + \nu})^{3/2(A-1)} \tag{2.10}$$

where ν_A is the parameter of the Gaussian wave function and the size parameter ν is related to the mean square radius of the emitting source:

$$R_{rms} = \sqrt{\frac{3}{2\nu}} \tag{2.11}$$

This method has described with success deuteron production in heavy ion collisions at AGS.

2.4 Thermodynamical Model

The aim of this model is to relate the measured momentum densities of particles to some physical quantities [27, 28]. This is done by characterizing the state of the system at the time of breakup by a temperature T, proton and neutron chemical potentials μ_p and μ_n and volume V. Chemical equilibrium among protons, neutrons and composite clusters is assumed to be reached late in the collision after decompression of nuclear matter.

The total number of particles of a particular specie (i.e. p, n, d, t etc.) is calculated by integrating the momentum distribution

$$\frac{d^3N_j}{d^3\overrightarrow{p}} = \frac{2s_j+1}{(2\pi)^3} V e^{(\frac{E_j-\mu_j}{T})} \tag{2.12}$$

where $\overrightarrow{p}$ is the momentum of the particle, s_j is the spin, $E_j = \sqrt{p^2+m_j^2}$ the energy, m_j its mass and μ_j is the chemical potential.

Assuming chemical equilibrium as:

$$\mu_A = N\mu_n + Z\mu_p \tag{2.13}$$

the proportionality factor is:

$$B_A = \frac{2s_A+1}{2^A}\frac{1}{N!}\frac{1}{Z!}(R_{np})^N[\frac{(2\pi)^3}{\gamma m_p V}]^{A-1} e^{-E_0^A/T} \tag{2.14}$$

which is the same as eq 2.8 plus the exponential term $e^{-E_0^A/T}$ which includes the fragment binding energy E_0^A.

This model compares well with data obtained from BEVALAC energies, even if the assumption to have a system with a uniform density in heavy ion collisions is questionable.

2.5 Flow and "Temperature"

Collective motion of particles has been measured in heavy ion collisions [29, 30]. The effect of collective flow is to introduce momentum–position correlations, therefore it should affect in some way B_2 when plotted as a function of the transverse momentum of the cluster.

In general three kinds of flow are defined: radial, elliptic (the matter is deviated in certain directions compared to the reaction plane) and directed (the matter is bounced off). Due to symmetries direct and elliptic flow vanish in central collisions (for more information see [31]).

Flow can be understood in terms of outward pressure originated by the very high density of matter in the center of the collision. This can be seen in figure 2.1. In the left picture the momentum–position is correlated and the measured volume is much less than when the momentum is randomly distributed across the source (right picture)

The effect of the flow is to increase the apparent temperatures of the particles, since a kinetic–energy factor (dependent on flow) is added to the thermal energy (due to thermal motion) of the particle:

$$\langle E\rangle = \langle E\rangle^{therm} + \langle E\rangle^{flow} \approx T_0 + mv_f^2 \tag{2.15}$$

where $\langle E\rangle$ is the particle mean energy, m the particle mass and v_f the flow velocity. Equation 2.15 includes a mass dependent factor. Therefore a larger particle mass gives higher apparent temperatures.

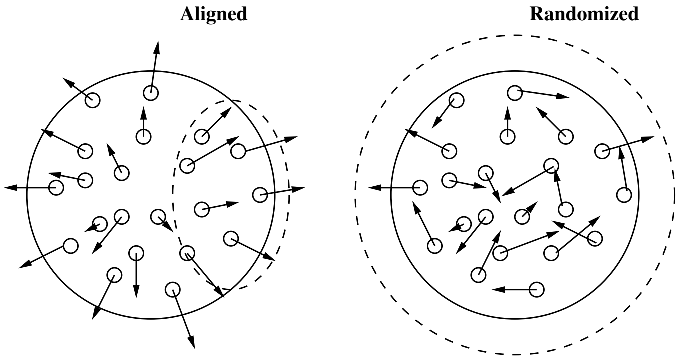

Figure 2.1: Example of radial flow. Small circles represent nucleons, and the arrows their transverse momentum vectors. The areas outlined with the dashed lines represent regions where we find pairs with small relative momentum.

Furthermore it has been observed that flow occurs for large systems and increases for higher densities (see figure 2.2). Figure 2.2 demonstrates the presence of flow at SPS energies.

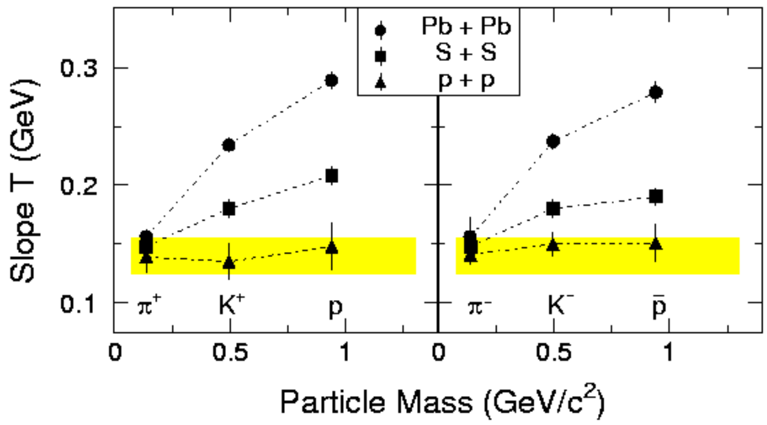

Figure 2.2: NA44 experiment [32]

The apparent temperature for different particle mass has been calculated at BRAHMS at 200 AGeV, included (anti–)deuterons. The results are plotted in fig 2.3. An increase of the apparent temperature for heavier particles is observed. The deuterons, however, do not directly feel the collective expansion since they are formed at freeze out.

Figure 2.4 shows flow velocities in function at different center of mass energy. Compared to SPS energies, the flow velocity at RHIC has increased.

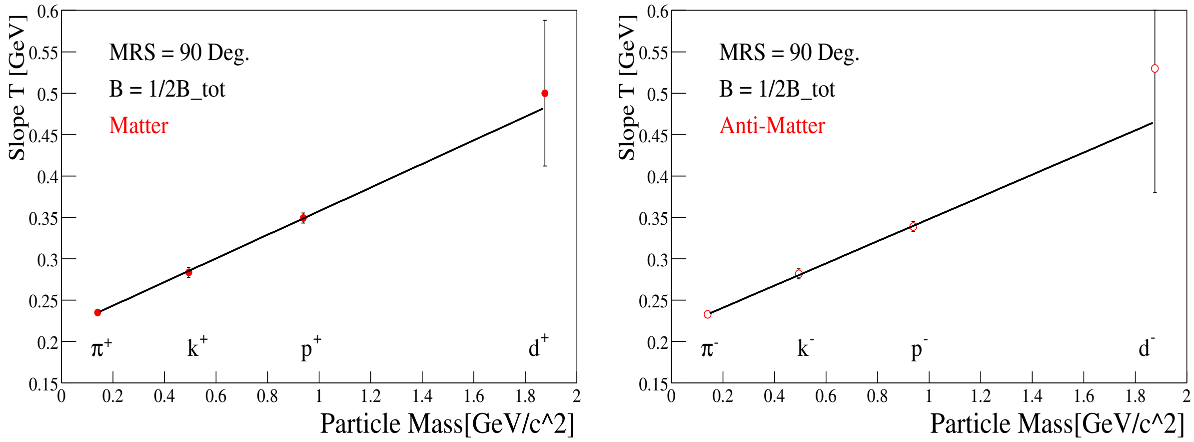

Figure 2.3: Inverse slopes parameter for pions, kaons and protons (left) and relative anti–particles (right) at 200AGeV using m_T–exponential fit as the fitting function. Data is taken from [33], except for (anti)deuterons temperatures which are calculated in this work.

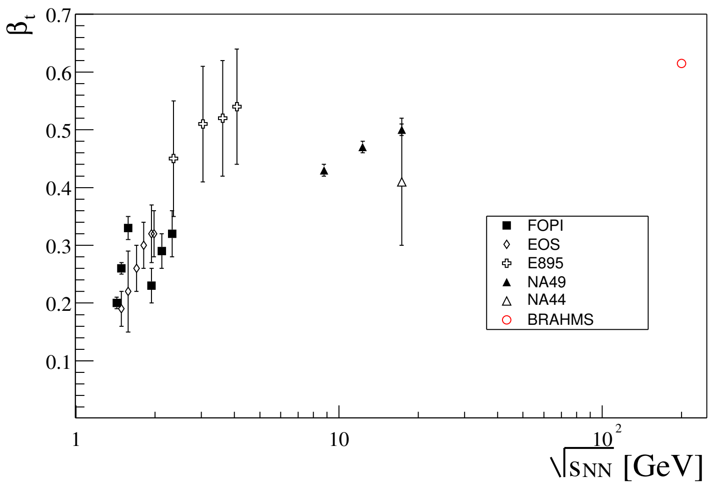

Figure 2.4: Flow velocities versus center of mass energy calculated using blast wave function. A constant flow profile is assumed. The picture is taken from [33].

One can therefore conclude that flow greatly effects B_2 calculations. Following the presented scenario, one should expect a B_2 independent of momentum because there is no collective flow. In contrast, in the presence of collective flow one should expect a momentum–dependent B_2. This will be experimentally investigated in chapter 6 for deuteron and anti–deuteron coalescence in central collisions at RHIC energies (Au+Au at 100 + 100 AGeV) and is one of the central topics of this thesis.

The next step is to introduce a natural development of the previous coalescence models: a model which includes a dynamical description of the source via calculations.

2.6 Polleri Model - A study of Interplay between Collective Flow and Density Profiles

Polleri et al. [34] made a model which relates position and momenta of the particles in a thermal system (e.g. in local equilibrium and characterized by a temperature T_0) due to the presence of collective flow. The source is taken to be cylindrical symmetric along the beam direction.

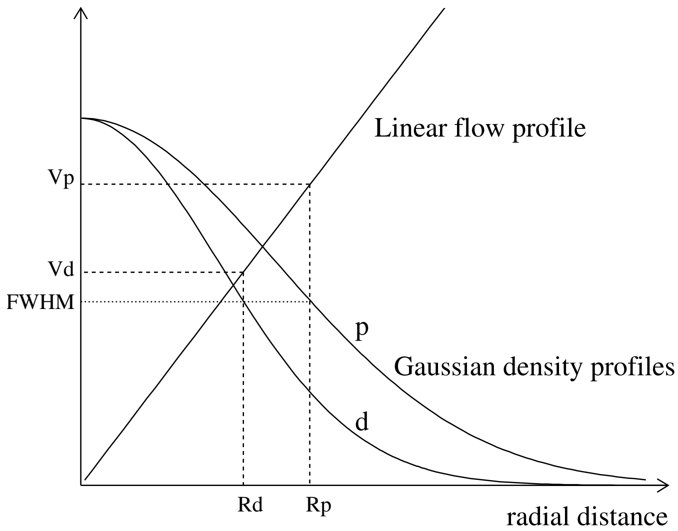

Figure 2.5: Interplay between density and flow profiles. Here the flow profile is assumed linear and the density profiles Gaussian. This corresponds to different mean flow velocities for deuterons and protons, while with a box profile this difference would disappear.

The main feature of this model is to show the interplay between flow and density profiles at the freeze–out stage (see figure 2.5). It demonstrates that the observed mass–dependence of the slope parameters and the p_T–dependence of the coalescence coefficient (which will be investigated in this work for RHIC energies) imposes serious constraints on the spatial profiles of the collective velocity and the particle density at the freeze–out stages.

In conclusion, for SPS energies the model predicts the different measured slopes of nucleon and deuteron transverse mass spectra. A transverse density profile of the source which is closer to a box rather than to a Gaussian shape, is required.

In [35] a density matrix approach has been used to describe the process of coalescence in ultra-relativistic collisions. An hydrodynamical parametrization has been applied for the source at freeze–out, which implements rapid collective expansions of the collision zone formed in heavy ion collisions. Data from CERN SPS by NA44 and NA52 collaboration has been analyzed. It has confirmed the finding of Polleri i.e. that the different measured slopes of nucleon and deuteron transverse mass spectra require a transverse density profile of the source which is closer to a box than to a Gaussian shape.

Chapter 3

The BRAHMS Experiment

First proposed in 1993, the Relativistic Heavy Ion Collider at Brookhaven National Laboratory (BNL) became operative with the first collision at 56 GeV Au+Au the 13 June 2000. Later in August, ions were successfully accelerated to $\sqrt{s_{NN}}$ = 130 GeV. The following run (RHIC run II) was performed at 200 GeV from August 2001 to January 2002. The data discussed are taken from that run.

In this chapter, RHIC is first introduced. This will be followed by a description of the BRAHMS experiment.

3.1 RHIC - The Relativistic Heavy Ion Collider

Figure 3.1 shows the RHIC complex at BNL. The RHIC tunnel is 3.8 km long and sits 3.6 meters underground. RHIC consists of 1740 magnets which are superconducting and it operates at a temperature of only 4.5 K above absolute zero.

Ions are accelerated in various steps: the Tandem Van De Graff uses a static electrical potential to accelerate atoms to remove some of their electrons. Positive ions are accelerated in bunches of $4.5{\cdot}10^9$ ions and enter HITL - the Heavy Ion Transfer Line, which carries them to the Booster. At this point, the ions are traveling at around 5% the speed of light, i.e. an energy of 1 MeV per nucleon.

The Booster accelerates the ion bunches up to 95 MeV per nucleon (35% the velocity of light) and feeds the Alternating Gradient Synchrotron.

The AGS increases the energy and strips more electrons from the ions. When entering the ATR (AGS-To-RHIC) line, ions have an energy of 10.8 GeV ($\sim$ 99.7% light velocity).

At the end of this line, a switching magnet sends the ion bunches down to the two RHIC's rings, where they are accelerated as in the AGS and the Booster. One of the beams travels clockwise while the other travels counterclockwise. They can collide at six interaction points. In this stage, 57 separate bunches of gold ions circulate at nearly light velocity (99.99%). Every bunch contains $\sim 10^9$ ions and each ion contains 197 nucleons. There are up to 1200 collisions per second, each collision producing between 0 to 5000 particles, depending on the centrality of the collision.

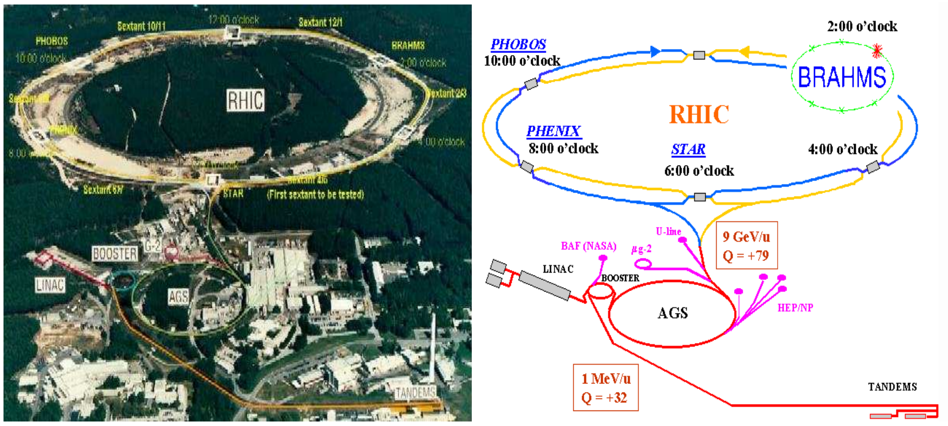

Figure 3.1: RHIC accelerator facilities.

Four of the interaction points are used for experiments. Looking at the RHIC as a clock, the four current experiments are at 6 o'clock (STAR), 8 o'clock (PHENIX), 10 o'clock (PHOBOS) and 2 o'clock (BRAHMS).

3.2 BRAHMS Overview

The BRAHMS experiment is designed to measure charged particles ($\pi^{\pm}$, $k^{\pm}$, $p\bar{p}$) over a wide range rapidity ($0 \lesssim y_{\pi} \lesssim 4$) and momentum (from 0.2 up to 25 GeV/c).

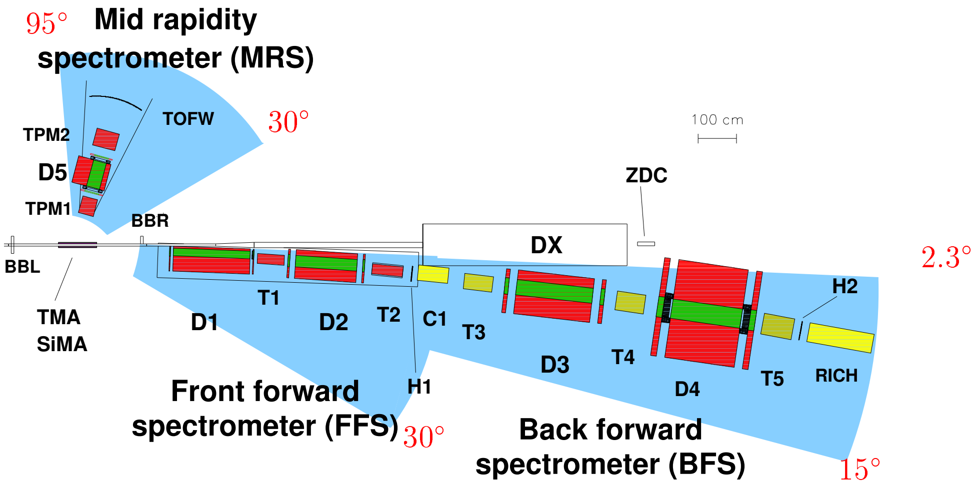

Figure 3.2: Overview of the BRAHMS experiment (top view).

The BRAHMS detector setup is shown in figure 3.2 (top view). BRAHMS consists of two spectrometer arms: the Mid–Rapidity Spectrometer (MRS), and the Forward Spectrometer (FS) which consists of two blocks, the Front Forward Spectrometer (FFS) and the

Back Forward Spectrometer (BFS). This section describes the BRAHMS detectors. The description is focused on the MRS, since the analysis of this work is based on data taken from this spectrometer.

3.2.1 The Detectors

MRS and FS are magnetic spectrometers, composed of different detectors. The "global detectors" are designed to locate the vertex position (in colliders, the vertex of the collision is not fixed), perform time measurements, determine the centrality and multiplicity of the collision. The "tracking detectors" and "particle identification detectors" track and identify charged particles. Figure 3.3 shows a schematic view of BRAHMS detectors.

TPC	T1, T2, TPM1, TPM2	Tracking
DC	T3, T4, T5	Tracking
TOF	H1, H2	Timing, PID
CHKV	RICH, C1	PID
ZDC	ZDC	Forward neutral energy, Primary Vertex
BB	BB left and right	Timing, Vertex, Multiplicity
MA	Scintillator tiles, Silicon strip detectors	Multiplicity, Centrality
Magnet	D1, D2, D3, D4, D5	Momentum selection
Magnet	DX (left and right)	Forward charged particle sweeping

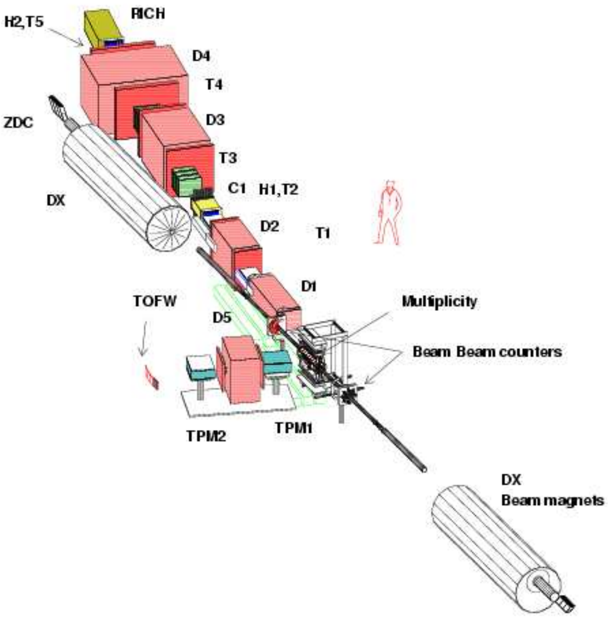

Figure 3.3: Layout of the BRAHMS experiment.

The Mid–Rapidity Spectrometer (MRS)

The MRS is designed to measure and identify particles in the mid–rapidity region. The spectrometer can be moved from 30 to 95 degrees with respect to the beam line. The solid angle covered at e.g. is ~ 6 msr.

The particle trajectories are deflected in the dipole magnet D5 and tracked in the two TPC's (TPM1–TPM2). The angle of the particle trajectory deviation in the magnetic field, together with information on the magnetic field strength, allows the calculation of the momentum of the particle associated to that track. Time measurements are done by TOFW. Combining data collected from TPM1, TPM2 and TOFW, the flight path of the particle is determined. The velocity is determined by measuring the time it took the particle to fly from the vertex collision to the TOFW. Using this calculated momentum and velocity, one can determine the mass of the particle.

The Forward Spectrometer (FS)

Tracking and PID for high momentum particles at high rapidity range is performed by the forward spectrometer (FS). The first section, FFS, can be positioned between 2.3 and 30 degrees. The BFS, which performs tracking and identification for the highest momentum particles, can rotate between 2.3 and 15 degrees.

In principle, the FS is not very different from the MRS. Two Čerenkov detectors are added to extend the PID to high momentum particles. The BRAHMS detector systems is described in detail in [36].

3.2.2 The Coordinates System

The global coordinate system in BRAHMS is right handed: the z axis follows the beam direction, the y axis points upward and x axis points away from the center of RHIC.

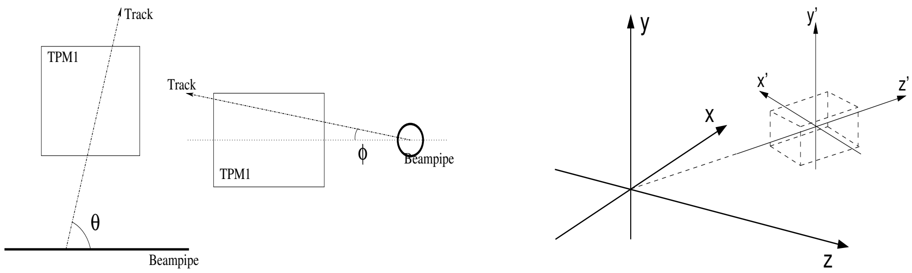

Figure 3.4: BRAHMS coordinate system (left) and global and local reference frames (right).

The local coordinate system of a single detector is also right handed: the z axis is parallel to the detector and points away from the collision vertex, whereas the y axis points upward.

3.3 Global Detectors

Global detectors measure global observables like charged particles multiplicities and collision vertex.

There are four global detectors in BRAHMS, namely: the Tile Multiplicity Array, the Silicon Multiplicity Array, the Beam–Beam Counters and the Zero Degree Calorimeters.

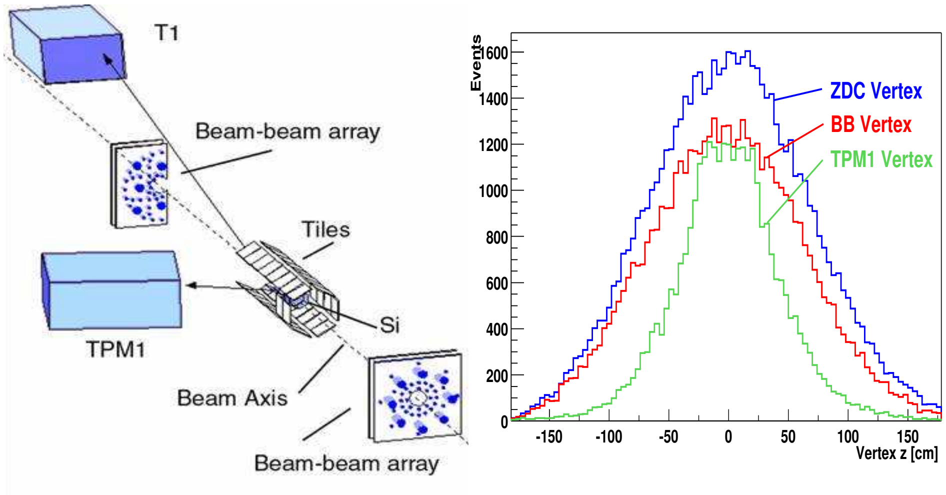

Figure 3.5: Global detectors (left): the Beam Beam Counters, T1 and ZDC's (not shown), are located along the beam line. TPM1 is a part of the MRS. In the figure on the right the resolution of the different vertex determination system are compared.

3.3.1 Multiplicity Arrays

The Multiplicity Arrays (MA) measure the overall charged particle multiplicity and provide a first level trigger to the other detectors.

The MA consist of two different sub–detectors (see figure 3.6), namely the Tile Multiplicity Array (TMA) and the Silicon Multiplicity Array (SiMA). These detectors give an independent measurement of the charged particle multiplicities.

A brief description of the two sub–detectors follows.

SiMA: The silicon detector is the closest to the beam pipe. The distance is 3.5 cm. There are 25 Si strip detector units (4 x 0.85 x 0.03 cm^3), arranged hexagonally around the beam pipe.

The ionizing radiation creates electron–hole pairs in the semi–conducting material, and the charge is collected through an induced electrical field.

The SiMA provides additional centrality and event by event fluctuation measurements (see [37, 38]). The pseudo rapidity range covered by SiMA is: -2.2 $\lesssim \eta \lesssim$ 2.2.

TMA: This detector can measure the charged particle multiplicity on a event-by-event basis in a pseudo–rapidity range -2.0 $\lesssim \eta \lesssim$ 2.0. The signals from the plastic scintillators are very fast and therefore suitable for use in the first level trigger of the experiment.

The TMA consists of 38 plastic scintillating tiles mounted on an hexagonal aluminum frame. Tiles are connected through optical fibers to PM tubes. The dimension of each tile is 12 x 12 x 12 cm^2.

A detailed description and documentation about MA's design and software can be found in [39].

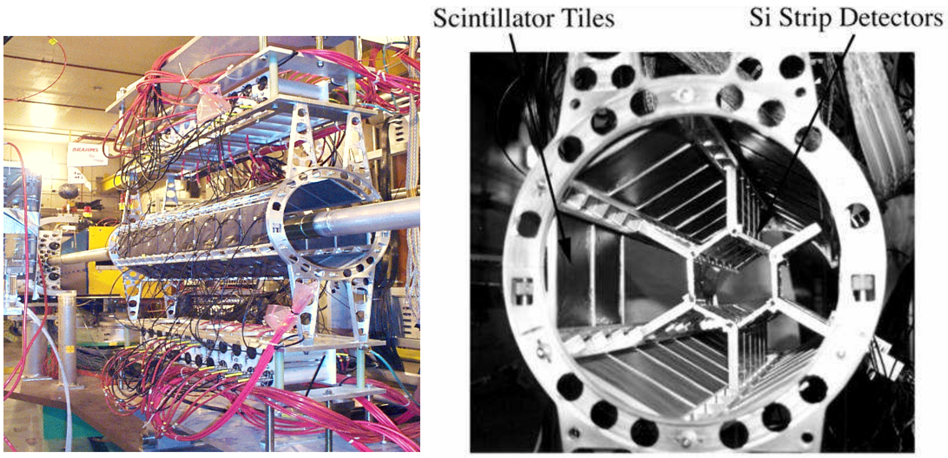

Figure 3.6: Left picture: MA overview. The right BB counter and D1 magnet are visible on the left. The beam pipe is situated into the hexagon. Right picture: MA details. The inner hexagon close to the beam is occupied by silicon strip detectors. The outer hexagon is filled with tile scintillator detectors.

3.3.2 Beam Beam Counters

The Beam Beam Counters (BBC) are designed to measure the primary vertex location by measuring the difference in particles arrival time between BBR and BBL, assuming that the particles travel at the speed of light. Furthermore they give the start–time for the time of flight (TOF) measurements. They are both illustrated in figure 3.7.

The Beam–Beam Counters consist of two arrays of fast Čerenkov radiators, each gripped with PM tubes. The diameter of the photo tubes is 5 cm or 1.9 cm connected to 3 cm long or 4 cm long radiators respectively. They are positioned at 2.2 meters on the left and right sides of the nominal interaction point. The left BBC - BBL - consists of 44 modules made up of 36 small tubes and 8 big tubes.The right array - BBR - has 35 modules in total, with 30 small tubes and 5 big tubes.

The intrinsic time resolution of a module is $\sim$ 50 ps, giving a 0.7 cm accuracy in determination of the interaction point.

The right and the left counters cover the same pseudo–rapidity range $2.2 \lesssim |\eta| \lesssim 4.6$, but have a different azimuthal angle. The vertex/start–time determination algorithm and BBC performance are described in detail in [14].

3.3.3 Zero Degree Calorimeters

The Zero Degree Calorimeters (ZDC) provide both timing (determine the interaction point with a resolution $\sigma_z \sim 2.8$ cm) and energy signal (by studying mutual Coulomb dissociations in Au+Au collisions [40]). They are lead–tungsten calorimeters, and are designed to measure the energy deposited by spectator neutrons emitted from collisions. For this reason the signal is strongly correlated with the impact parameter. Neutrons are uncharged,

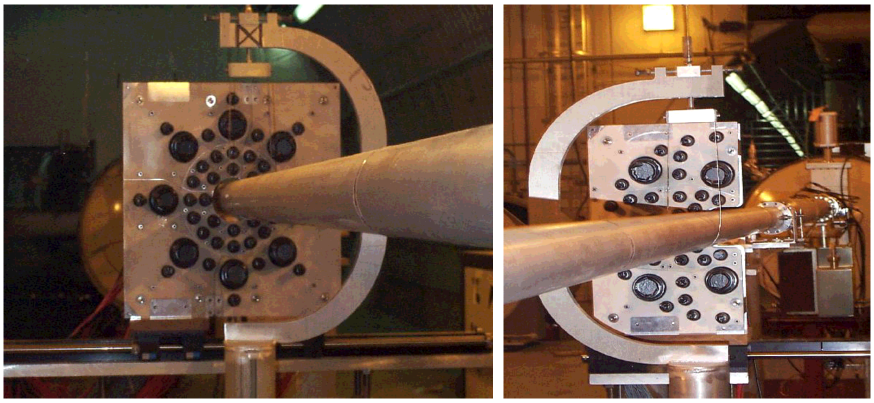

Figure 3.7: Left (left) and right (right) BBC arrays. Note in the BB left array the higher distribution of large tubes in the external zone, and the higher distribution of small tubes in the internal more high particle dense region. The BBC right array has a different geometry, designed in order to not interfere with the close magnet D1. The reduced coverage is partially compensated by higher spatial density of modules in the array (the angular coverage is from 1.6° to 5.8°).

and are therefore not deflected by the magnets and will continue along the beam direction close to zero scattering angle. This is the reason why the ZDC's are situated behind the beam magnets DX, 18 meters on each side of the collision vertex.

Each ZDC consists of three modules, each made of 29 layers of 5 mm tungsten plates separated by 0.5 mm Čerenkov radiating fiber to sample the hadronic shower. The modules are read out with photo–multipliers, one for each module.

Each of the RHIC experiment is equipped with identically constructed ZDC, allowing for a comparison of the results between all the experiments. The ZDC design is described in detail in [41].

3.4 Tracking Detectors

"Tracking" a charged particle means reconstructing its path inside an apposite device. In BRAHMS the devices are the Time Projection Chambers and the Drift Chambers. They can measure the energy loss of the particle, locate where it was deposited and therefore extrapolate where the particle interacted in the volume.

3.4.1 Time Projection Chambers

As already mentioned, the Time Projection Chambers (TPC) are designed to provide particle tracking. In BRAHMS, there are 4 TPC's: T1, T2 in FFS and TPM1, TPM2 in MRS (see figure 3.3 as reference).

The TPC's are filled with a mixture of Ar and CO_2. A vertical electrical field $\vec{E}$ is generated by a cathode plate and held at a potential of $\sim$ -5000 V at the bottom of the cage. When a charged particle travels through the volume, the gas is ionized, meaning the ions produced travel down toward the cathode, and the electrons drift upward, opposite the direction of $\vec{E}$. Then the electrons will approach the first wire plane (the gating grid), which is connected to the trigger system. The gating grid is "opened" (no voltage) for a short time only when a trigger signal indicates that there is data to read out, otherwise it is "closed" (high negative voltage), preventing electrons from entering the drift region.

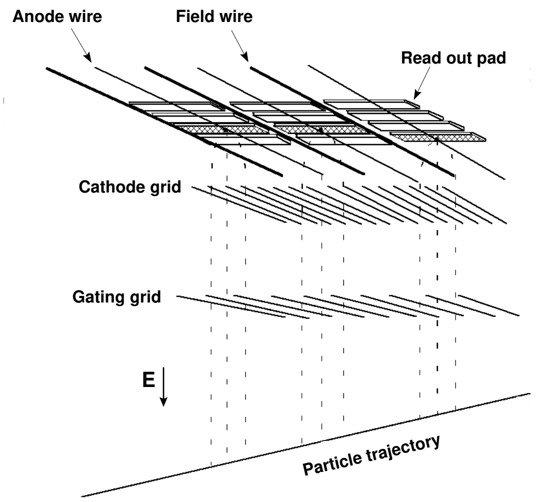

Figure 3.8: Schema of the wires and pads inside a TPC.

After the electrons have passed the cathode plane they are accelerated toward the anode wires held at $\sim +1150V$. The field gradient here is so high that an avalanche of electrons occurs. The total charge generated in the avalanche is proportional to the number of primary electrons that were liberated by the particle traversing the detector.

The avalanche also induces a charge on the pads below the anode wire. The anode wires provide the z coordinate (row number) and the pads give the x coordinate. The y coordinate is obtained by measuring time difference between the primary ionization and the drift time of primary electrons to the anode pad plane. This is possible because the drifting velocity is low compared to the velocity of the particles that traverse the TPC.

The specifications for the BRAHMS TPC's are listed in table 3.1.

TPC	Dist. to Vert.[m]	Width [cm]	Height [cm]	Length [cm]	No. Rows	Pad/ Row	$\langle\sigma_x\rangle$ [mm]	$\langle\sigma_y\rangle$ [mm]
T1	5	33.60	22.00	56.00	14	96	0.38	0.40
T2	8.1	2x39.00	2x22.00	2x31.5	2x8	112	0.37	0.41
TPM1	0.95	37.5	21.00	36.00	12	96	0.31	0.43
TPM2	2.85	50.00	22.00	67.5	20	144	0.39	0.49

Table 3.1: TPC's specifications. *No. rows* are the number of the instrumented rows, *pad/row* the number of pads per row and $\langle\sigma\rangle$'s are the average hit position resolution.

The choice of gas and pressure effects the drift velocity and the diffusion of the drifting electrons. The efficiency depends also on the atmospheric pressure. The gas in the TPC's is a mixture of Ar and CO_2 (90% and 10% respectively) which gives a relatively low drift velocity and small electron diffusion.

Details of the BRAHMS TPC's can be found in [36].

3.4.2 Drift Chambers

The drift chambers (DC) in BRAHMS are T3, T4, T5. They are located in the BFS at 10.5 m, 14.5 m and 18.4 m respectively from the nominal vertex.

Drift chambers are, like TPC's, tracking devices. Drift chambers are mostly efficient at low track densities, a condition that is satisfied in the BFS.

Each DC has three modules, each consisting of a volume filled with gas, with planes of anode–cathode wires and field wires. When a particle traverses the detector, it ionizes the gas in the detector volume, and electrons are liberated. The electrons then drift to the anode wire in the electrical field induced by the field between the cathode and field wires. Near the anode an avalanche of electron–ion pairs is created like in the TPC.

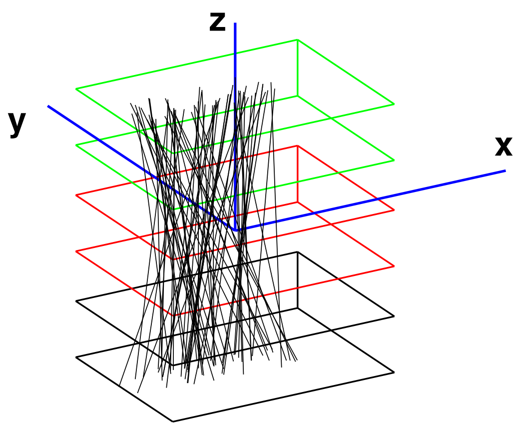

Figure 3.9: Reconstructed tracks in T3 [42].

The track reconstruction is based on matching hits on the different planes in the drift chamber (see figure 3.9).

More details about BRAHMS DC's are available in [43].

3.4.3 Dipole Magnets

The magnets (together with TPC's and DC's) allow momentum determination of the charged particles by bending their path. The knowledge of the magnetic field, the length of the magnet gap and the bending angle of the track are enough to reconstruct the momentum (section 4.3.2).

There are five magnets in BRAHMS, named D1 through D5. The field is oriented vertically and deflects particles only in the $x - z$ plane.

In the FS, and A(B) field corresponds to negatively (positively) charged particle detection. In the MRS, both charge signs are detected in a single polarity setting. Using setting A will bend positively charged particles on the left relative to their direction of travel. Setting B is the opposite polarity and thus bends negative charged particles on the left. Table 3.2 illustrates magnets technical characteristics.

The five dipole magnets are made of iron with copper conducting coils and epoxy–glass insulation. The design of the magnets was optimized by the use of detailed three dimensional field calculations given by the code TOSCA. D5 is the mid–rapidity spectrom-

	Length [cm]	**Width** [cm]	**Max Field**[T]	$B \cdot dl$ [Tm]	**Current** [A]
D1	225	49	1.26	2.6	3450
D2	200	98	1.68	2.8	3000
D3	253.3	113.6	1.22	2.58	3000
D4	251.5	253.3	1.19	2.34	2750
D5	99	101.6	1.45	1.21	2500

Table 3.2: Magnet dimensions and field specifications.

eter magnet, designed for particles emitted at mid–rapidity. The set D1–D4 provides the necessary particle trajectory bending for the higher momentum particles expected in the forward direction.

3.5 Particle IDentification (PID) Detectors

The Time of Flight Measurements (TOF) performed by the hodoscopes and the response of the Čerenkov detectors are used for the particle identification (PID) of charged particles.

3.5.1 Hodoscopes

Hodoscopes provide Time Of Flight measurements, which are defined as time for charged particle to fly from the collision vertex to the scintillator slats of the hodoscopes.

The hodoscopes in BRAHMS are H1, H2 and TOFW (Time Of Flight Wall), and are located in the FFS, BFS, MRS respectively. Figure 3.10 shows the different designs between H1, H2, which are similar, and TOFW.

Figure 3.10: The left picture shows H1 during the installation. On the right a front view of TOFW is shown.

TOF is started (start–time) by the global detector system and stopped (stop–time) when the hodoscopes measures the particle. The flight time is obtained by subtracting the readout time with the start–time (see [14] for details). This information is used to calculate the velocity of the particle. Knowing the flight time and the momentum, a particle can be identified using a simple formula (section 4.4.1) which relates the mass, velocity and momentum of a particle.

Name	Dist to nominal vertex [m]	Slats dim. x y z [cm]	Species separated	Maximum p [Gev/c]
H1	8.7	1 x 1 x 20	π/K	3.8
			K/p	6.5
H2	18.6	1 x 1.5 x 40	π/K	5.8
			K/p	9.7
TOFW	4.3	1.27 x 1.25 x 22	π/K	2.5
			K/p	4.3

Table 3.3: TOF Hodoscopes physical properties.

The hodoscopes consist of an array of vertical scintillator slats, each with fast photomultiplier tubes (PM) mounted at each end. Hodoscopes are numbered from left to right.

The nominal time resolution of each tube is $\sigma_t \sim 65\ ps$. H1 and H2 consist of 40 and 32 slats respectively while TOFW consists of 125.

The panels of TOFW are situated in arc–like arrangement. The radius of the arc is 240 cm with its center located at the center of D5. In this arrangement, particles coming from D5 have near normal incidence upon the slats.

Table 3.3 shows some properties of the TOF systems, including K/π and K/p momenta separation limits.

3.5.2 Čerenkov Detectors

Čerenkov detectors provide PID for high momentum particles and can identify pions from 2.7 GeV/c. In BRAHMS, two Čerenkov detectors are used to extend the PID in the forward spectrometer, namely C1 and RICH.

C1 is a threshold Čerenkov detector. The gas mixture is chosen so that the threshold is 2.6 GeV/c for pions, 9.3 GeV/c for kaons and 17 GeV/c for protons. Thus if f. ex. a particle of 13 GeV/c passes through C1 and gives no signal, it is likely to be a proton.

Figure 3.11 (left) shows schematically C1 principle.

The photons emitted by the particle in the gas (C_4F_{10}) are reflected up or down by two 45° mirrors in the back, and detected by two arrays of PM tubes above and below the radiator volume.

RICH stands for Ring Imaging ČHerenkov detector (fig 3.11 - right). This detector has a large concave spherical mirror that reflects Čerenkov light emitted by the particle in the gas of the detector vessel. The light cone is focused into a ring of light onto a focal plane.

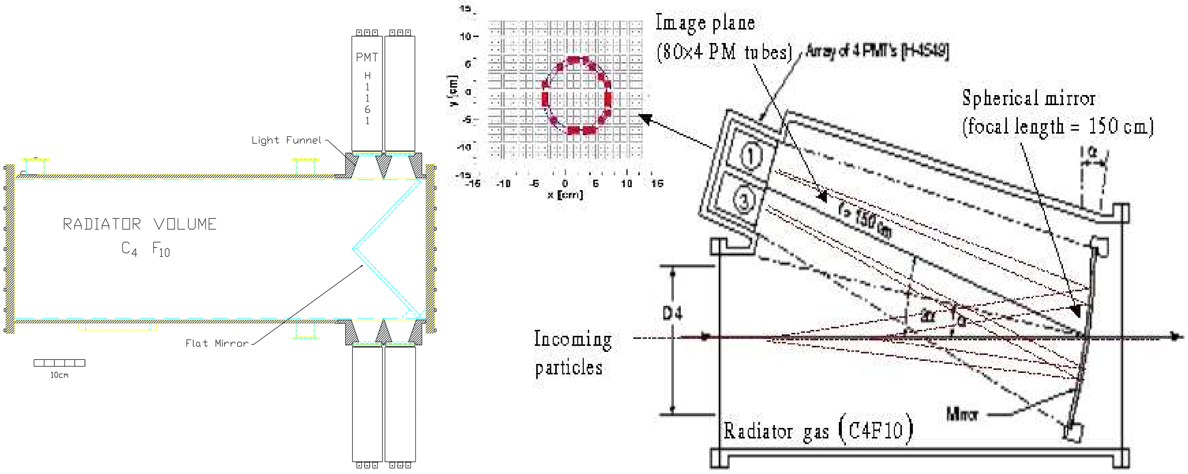

Figure 3.11: Čerenkov detectors: C1 (left) and RICH (right).

Due to the high segmentation of the array, the radius of the focused Čerenkov light cones can be reconstructed. The ring radius is related to the the photon detection angle, and thus to the velocity of the particle. The ring radius depends on the mass and velocity. PID can be performed using the formula $m^2 = p^2((n\cos\theta)^2 - 1)$ (where n is the refractive index of the radiator gas).

RICH thresholds are 2.19 GeV/c for pions, 7.7 GeV/c for kaons and 14.7 GeV/c for protons.

3.6 Detector Acceptance

Figure 3.12 shows the BRAHMS acceptance, which is the phase–space region over which the spectrometers can measure pions, kaons and protons. For a given setting both spectrometers have small solid angle coverage (6.5 msr for the MRS and 0.8 for FS). By combining many different settings, however, it is possible to map a bigger part of the phase–space. By design, the BRAHMS spectrometer can identify pions and kaons over the rapidity range -0.1 $\lesssim$ y $\lesssim$ 3.8. Within the acceptance of run II it is possible to obtain rapidity densities dN/dy for protons and (anti–)protons at selected rapidities $0 \lesssim y \lesssim 3$.

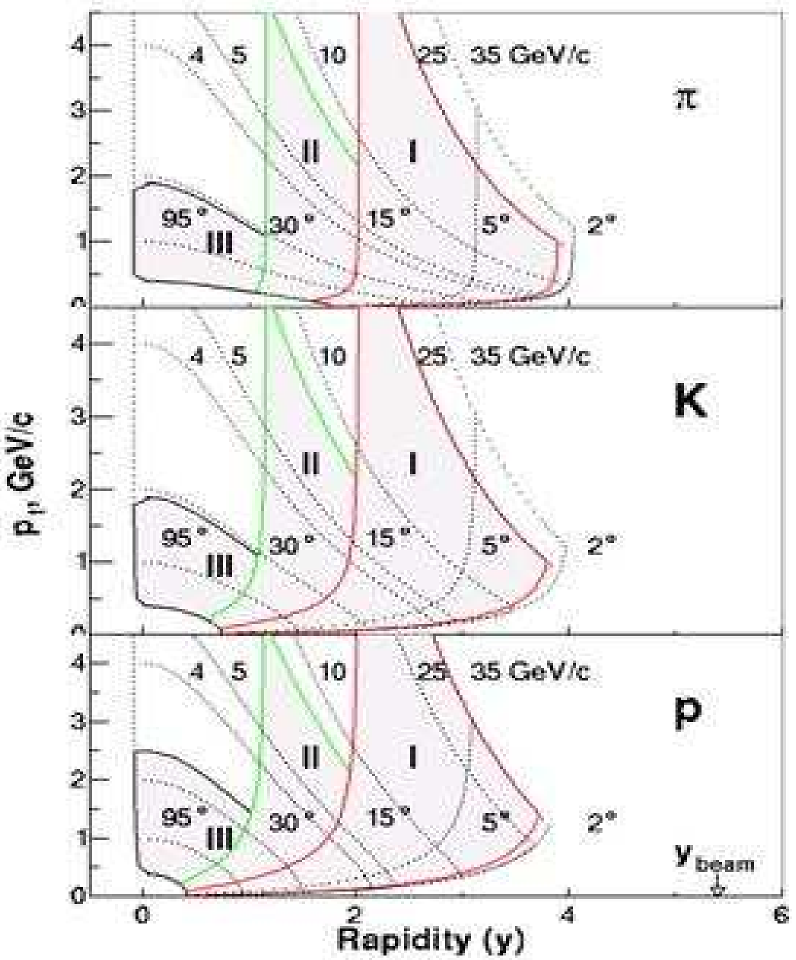

Figure 3.12: BRAHMS acceptance for pions, kaons and protons. Regions III, II, I correspond to measurements using MRS, FFS and BFS respectively. The nearly vertical lines marked with 2°, 5°, 15°, 30° and 95° indicate zones at constant angle, while the curves that decrease from left to right indicate constant momentum.

Chapter 4

From Raw Data to Physics

The purpose of this chapter is to give an overview of the reconstruction of the data collected during the Au+Au run at 200 GeV in 2001.

Each event is characterized by a centrality, multiplicity (number of particles produced) and vertex position along the z axis. The *local* tracks are reconstructed in the projection chambers and the *global* tracks are constructed by combining the knowledge of the vertex of the collision, the TOF hits and the local tracks. The momentum and velocity are assigned to the tracks using the magnets and TOF respectively. The final "product" will be well–characterized events with respective tracks all stored in ordered data structures from which they are easy to access.

4.1 DAQ and Triggers

In order to study the physics of collisions, first thing one must define an "event" (or collision).

This is done with the use of the *triggers*, which give the conditions under which the DAQ (Data Acquisition system) shall record data. Table 4.1 is a list of the trigger conditions used in BRAHMS at 200 GeV.

As shown in table 4.1 the trigger box allows to select between different conditions and combinations. Trigger 4 is the most inclusive. It covers all nuclear reactions, electromagnetic dissociation and from central to peripheral collisions. It defines the *minimum bias* event sample and covers 97% of the full nuclear cross section. Trigger 1 selects about 50% of the nuclear collision event.

For all the events of this analysis trigger 6 is requested, selecting central collisions in a narrow interval around the nominal collision vertex.

4.2 Event Characterization

This section describes how the centrality, charged particle multiplicity and vertex position are determined for each event.

Trigger	Description
1	Coincidence of both BBC arrays, with a requirement of 2 or more tubes with hits both in the left and right array
2	Coincidence of both BBC arrays, with a requirement of 1 or more tubes with hits both in the left and right array
3	Energy threshold in the TMA and SMA ($\sim$ 20% centrality)
4	ZDC arrays coincidence with narrow time overlap of $\sim ns$, summed energy signal from each module with energy > 25 GeV and > 4 hits in TMA.
5	Coincidence of the two BBC arrays, with a narrow time gate, selecting primary vertex z–coordinates $\in$ [-25cm, 20cm]
6	Coincidence of triggers 3 and 5. (Vertex and Multiplicity trigger)
7	Pulser trigger for pedestal runs
8	1 Hz synchronization trigger. Can be used for background studies.

Table 4.1: The BRAHMS triggers in run II.

4.2.1 Multiplicity and Centrality Determination

Since it is not possible to directly measure the impact parameter b, the *centrality* concept is used instead.

It is possible to calculate the charged particle multiplicity and the centrality of the collision for an event from the energy deposited in the SiM and TMA, assuming that the largest multiplicity corresponds to the most central collision.

First, the total calibrated energy (given by the energy loss signal in the detector) deposited in each element of TMA tiles and SiMA strip is divided by the expected average energy deposited by one charged primary particle (MIP - Minimum Ionizing Particle - see [37]) in a tile. The expected energy, or conversion factors, are evaluated by GEANT simulations. In this way the charged particle multiplicity for each element is obtained. Then the final multiplicity distribution is obtained by adding the individual contributions from the detector elements, corrected for the geometrical acceptance of the given element and normalized to the number of events (see figure 4.1).

Background particles contribute significantly to the deposited energy by about 10% in the SiMA and 30% in the TMA elements. The energy calibration of the detector elements originate from very peripheral events, pulser, cosmic ray etc., where one tries to determine the energy deposited by a MIP (Minimum Ionizing Particle). Since the amount of material that a particle traverses depends strongly on the primary vertex position, a correction factor depending on the angle of incidence of the particle is introduced and multiplied to the gain corrected value.

Assigning a certain centrality to an event means determining if a given event is among the x% most central ones, i.e. determining how central (or peripheral) the collision is. Centrality cuts are applied by selecting appropriate ranges in the multiplicity spectrum.

In this analysis, the estimated error on the charged particle multiplicity is of the order of 10% [44].

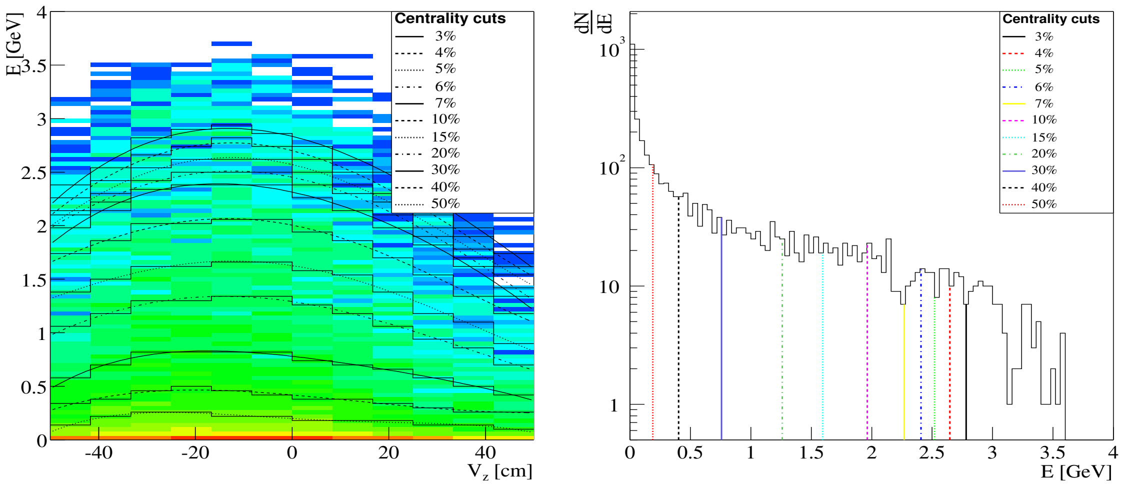

(a) (b)

Figure 4.1: Centrality cuts based on the energy deposited in the TMA [38]. Figure (a) shows the energy deposited and the distribution of the cut values as a function of the primary vertex coordinate. Figure (b) shows a section of (a). If an event has a total energy deposited of say 2 GeV, it has a centrality of 7-10%.

4.2.2 Vertex Determination

In collider experiments the vertex position changes from event to event. It is important to know the precise location of the vertex.

Three detectors are used to determine the collision vertex: BBC, ZDC and TPM1. Fig 4.2 illustrates the vertex determination method and the correlation between the BB and TPM1 vertexes. In the present analysis the vertex is calculated using the Beam–Beam Counters.

To improve the quality of the measurements, it is necessary to apply a set of calibrations to the BBC's. A calibrated BB hit consists of time information and an estimation of the number of particles that hit the tube (see for details [14]).

After the calibrations, the vertex is calculated with the following equation:

$$z = c(\langle t_L \rangle - \langle t_R \rangle)/2 = c(\langle t_L \rangle - T_0) - (\langle t_R \rangle - T_0))/2 \tag{4.1}$$

where $T_0 = (\langle t_L \rangle + \langle (t_R \rangle)/2 + T_{const}$ is the time zero signal, $\langle t_{L,R} \rangle$ are the average times measured in the left and right arrays respectively, and T_{const} is a constant time delay which depends on differences in cable length as well as delay in the electronics.

The difference of the distribution of the BBC vertex and the TPM1 track projections to the beam-line is used to estimate the BB vertex resolution. The width of this distribution is an upper limit to the BBC vertex resolution. The resolution achieved so far is ~ 0.7 cm for the most central events. See also [14].

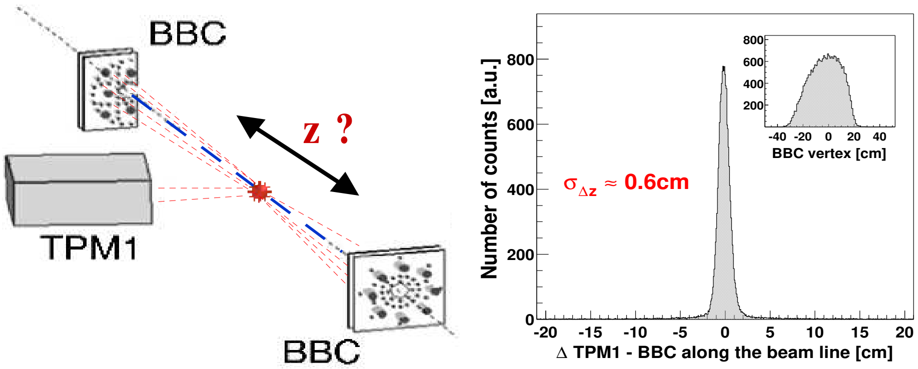

Figure 4.2: Vertex Determination (left) and resolution (right) in BRAHMS at $\sqrt{s_{NN}}$ = 200 GeV.

4.3 Particle Tracking

The first part of this section describes how local tracks are reconstructed into the Time Projection Chambers. Then the momentum determination method is introduced, followed by the particle flight path length from the primary vertex to the hodoscopes plane.

4.3.1 Local Tracking

Local tracking is the first step in Particle IDentification. Local tracking is done in the BRAHMS TPC's and DC's (DC tracking is described in [45]).

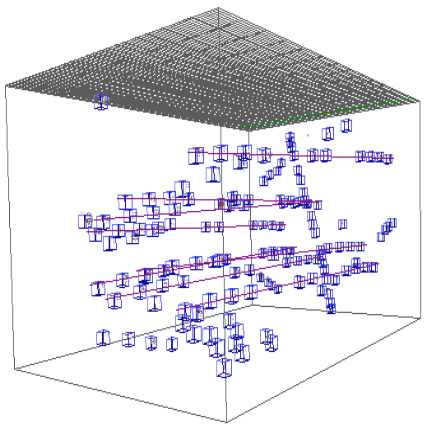

Figure 4.3: Local tracking in TPC's [37].

Before tracking, several calibrations to the TPC's are required. These helps identify bad pads, correct non–linearities of the drift velocity, and measure drift velocity, since pressure changes can change drift velocity with time.

In local tracking the ADC signals of the detectors pads are converted into 3-d segments. This is done in several steps using tracking algorithms (see [7]). First the ADC signals are grouped into clusters. If the clusters overlap, they have to be separated into two or more clusters (deconvolution). Then the deconvoluted clusters are converted into TPC hits containing spatial position and energy loss information. Finally the hits are grouped together by the "track follow finder" algorithm and fitted together to obtain a 3–d track line. These procedures are described in detail in [7].

4.3.2 Momentum Determination

Momentum determination in BRAHMS is done thanks to the dipole magnets. The radius of curvature of the charged particle trajectory through the magnets is calculated and the trajectory is estimated by matching the tracks of the incoming and outgoing tracks in the magnet. Fig 4.4 shows momentum calculation in the MRS.

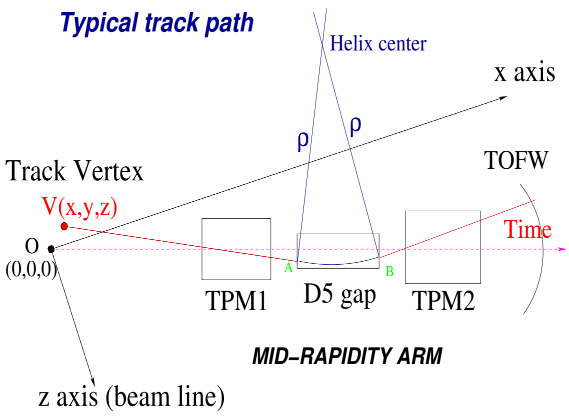

Figure 4.4: Momentum determination in BRAHMS in the MRS (top view).

The momentum is calculated with the following equation:

$$\frac{p}{q} = B\rho = Bl/\theta \tag{4.2}$$

where p is the particle momentum, q the particle charge, ρ is the radius of its trajectory in the magnetic field, l is the length of the magnet gap and θ is the angle between the tracks.

Momentum resolution is therefore dependent on $B \cdot dl$ integrated over the length l of the dipole, where B is the (constant) magnetic field.

4.3.3 Track Extrapolation

The finding of the *global tracks* i.e. particle flight path from the collision vertex to the TOFW (in the case of MRS) is necessary to complete the PID. It requires an estimation of the track origin and track end. The track origin is the track vertex, explained in section 4.2.2. The track end is the track line intersection with a plane defined by the hodoscope axes. In the MRS, tracks are extrapolated from TPM2 to TOFW panel planes. For details see [14].

4.4 Particle Identification

After the total track length and the associated momentum have been found, the PID is completed by calculating the velocity of the particle with TOF.

4.4.1 TOF Technique

Velocity is determined using TOF measurements. As for the BBC's, the hodoscopes need several calibrations. The TOF calibration procedure is quite similar to BBC's calibration. All calibrations are done in a semi–automatic way in a run by run basis so that it matches the BBC calibration. A calibrated TOF hit provides information of both the time the particle takes to fly from the vertex to the slat and the energy loss.

Once TOF hits are matched to global tracks, one can determine the velocity of the particle:

$$\beta = \frac{L}{ct_{tof}} \tag{4.3}$$

or

$$\frac{1}{\beta} = \sqrt{1 + \frac{m^2}{p^2}} \tag{4.4}$$

with L the track length from the vertex to the TOF wall and t_{TOF} the flight time. L depends on the position of the hodoscope, preferably long enough for a good PID resolution.

The precision of the velocity resolution depends on both detector timing resolution and the accuracy of the vertex position.

4.4.2 TOFW Performance

Now that the local/global tracks, the respective momentum and velocity are determined, it is possible to proceed with the PID.

In this section the ability of TOFW to identify particles is shown. Figure 4.5 shows particle velocity versus momentum in the MRS at 90 degrees (y = 0). The only requirements for the selected events are trigger 6 (i.e. centrality $\sim$ 0 to 20%) and a collision vertex between -20 and 20 cm where the trigger 6 conditions are the most effective.

From figure 4.5 the separation between pions, kaons, protons and deuterons is clearly visible. The effective TOFW resolution is $\sim$ 80 ps (see [14]). It is also clear that the PID quality depends on momentum, time, and track path length resolution. For momentum values where the particle shapes overlap (i.e. $>$ 2 GeV for pions and kaons), it is not possible to distinguish between the particle species.

The resulting PID can be improved by eliminating multiple TOF hits, uncorrelated track–TOF hit pairs, secondary tracks produced far from the nominal collision vertex. These, and other methods, are applied and explained in the next chapter (see f. ex. figure 5.3).

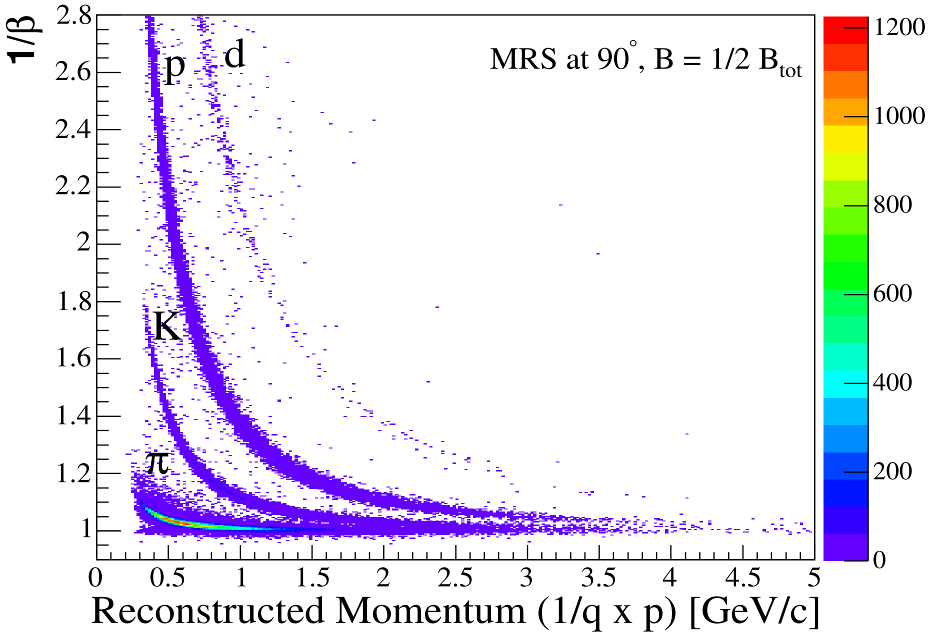

Figure 4.5: Particle velocity versus reconstructed momentum p/q (see equation 4.2) in the MRS from events with centrality 0 to 20% and collision vertex between -20 and 20 cm. No track quality cuts are applied. The figure was obtained with $\sim 10^6$ events and $\sim 6 \cdot 10^5$ tracks.

Chapter 5

Analysis

The aim of this chapter is to build the (anti–)protons and (anti–)deuterons spectra (at rapidity $y = 0$ and $y \approx 0.9$), in order to calculate the coalescence parameter B_2 (done in the next chapter). The first part of the analysis describes the data selection, including event selection, particle selection, and PID methods. The second part shows data correction, geometrical acceptance, detector efficiency, and corrections due to secondaries (particle production, absorption and multiple scattering). Finally, data normalization and statistical errors are shown.

With regard to the corrections, $6 \cdot 10^5$ events (the "real" selected events are $\approx 3 \cdot 10^6$ and $\approx 7 \cdot 10^5$ for MRS at 90 and 35 degrees respectively) have been simulated as close as possible to the experiment conditions to obtain the best results. This is done using the event generator Hijing.

5.1 BRAHMS Analysis Software

This section describes briefly the software tools used to perform the analysis: Root's Object Oriented Technologies (ROOT) and Brahms Analysis GEANT (BRAG).

ROOT

ROOT is a C++ based class library containing basic tools for handling and analyzing data, like reading and writing data–objects from files, storing event–information in more accessible ways and displaying data in the form of histograms, scatter–plots etc. ROOT homepage can be found at [46].

BRAHMS experiment requires more specialized tools, and consequently BRAT toolkit has been, and continues to be, developed.

BRAT

BRAT is a collection of C++ classes and application packages for dealing with detectors and data in BRAHMS. BRAT is based on ROOT class library and also contains its own interfaces to the Data Acquisition System (DAQ) and to parameter and calibration databases written in MySQL.

The next scheme further shows the relationship between the over cited software packages and the computer languages used.

$\boxed{\text{FORTRAN77}}(\textit{language})\longrightarrow \boxed{\text{CERNLIB}}(\textit{framework})\boxed{\text{GEANT}}(\textit{framework})\longrightarrow$

$\longrightarrow\boxed{\text{BRAG}}(\textit{application})$

$\boxed{\text{C++}}(\textit{language})\longrightarrow \boxed{\text{ROOT}}(\textit{framework})\boxed{\text{BRAT}}(\textit{toolkit})\longrightarrow$

$\longrightarrow\boxed{\text{BRATMAIN\&BRATROOT}}(\textit{applications})$

5.2 Event Selection

Before the PID selection the runs must be analyzed in order to exclude the bad ones (i.e. runs with some uncorrectable errors as detector malfunction etc.). Events with irrelevant triggers and interaction point outside of the defined cuts are discarded. It is also important to check the accuracy of the detector calibrations.

In this analysis the following global cuts are applied:

Trigger Cuts: Only events recorded by trigger 6 are used. This is the hardware trigger selecting the most central events (see section 4.1), including centralities from 0% up to 20–25% of the most central events.

Vertex Cuts: Only events with vertexes in a vertex range between -20 and 20 cm from the nominal collision point are selected. This is the best compromise between collecting as much statistics as possible because of the low number of deuterons. The limit imposed by trigger 6 regulates efficiency which begins to drop around this range.

Centrality Cuts: Events with centrality between 0–10% are selected. This range is chosen because one needs for the analysis central events, events including enough statistics and data comparable with other experiments.

5.3 Particle Selection

After event selection has been performed the particles are identified and selected for each event. This is done in few steps. First the tracks are reconstructed and tracks with bad characteristics such as background tracks or tracks too close to the magnet, are rejected. Then the particles are identified with the PID method. Finally, in order to compare protons and deuterons for the B_2 calculation, the rapidity cuts are applied.

5.3.1 Track Selection

First of all, the constancy of reconstructed tracks per event is checked through all run collection of the spectrometer setting. This allows one to find malfunctions of the spectrometers.

It is then checked to determine if a correct matching procedure was performed. This is done by checking how close the track is to the margin of the magnet after two tracks are matched. If it is less than one cm (track hits the magnet) it is discarded.

Another check determines the matching between TPM tracks and hits in hodoscopes of TOFW is done properly. This is done by examining the agreement between the vertical position of the projection and the horizontal slat position calculated from the time–difference of the top and bottom of the PMT.

Not all TOFW slats are calibrated for all the runs. In addition, some of them have very few hits which decreases the quality of the calibrations, and there are also slats where the signals are missing or bad. Therefore these slats are cut in the data. To correct for this, the same slats are cut also in the geometrical acceptance (section 5.5).

One must select tracks that point back to the interaction point (IP). This is done by pointing TPM1 tracks back to the IP, and requiring to be at a given distance from it. To do this, in MRS the tracks are pointed back in the $y-z$ plane and the resolution of the pointing is determined by fitting the distributions with a Gaussian. Then, a 2.5σ cut is applied to eliminate secondary and background tracks (i.e. tracks not coming from the interaction diamond, due to noise and secondary interactions). Furthermore this cut has been chosen to select almost all original tracks (99%). Picture 5.1 shows the distribution of TPM1 projected tracks in y (vertical plane) and z (along the beam pipe) before the cut.

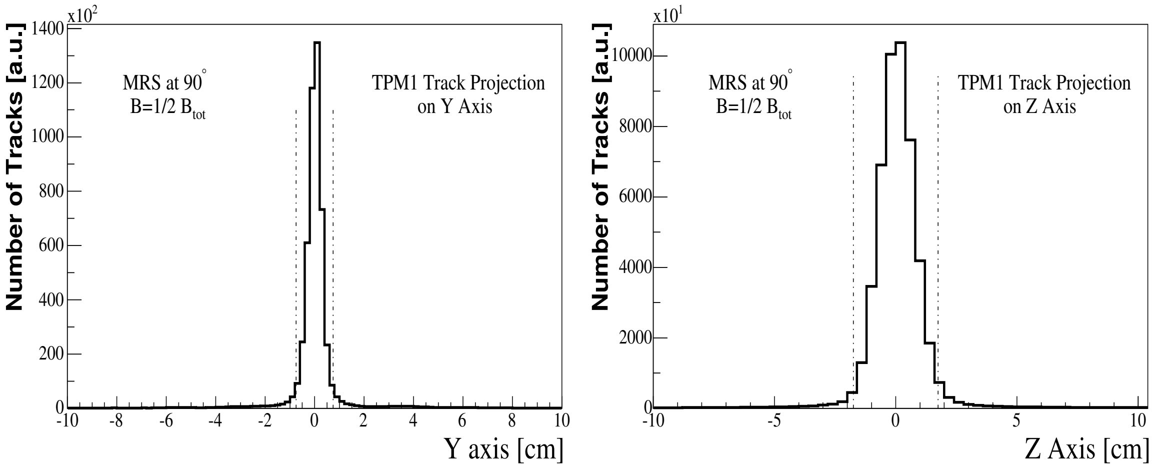

Figure 5.1: Projection of TPM1 tracks on y (left) and z (right) axes. The width σ of a fitted Gaussian is 0.3 and 0.7 respectively.

These two peaks are fitted to a Gaussian distribution and the value of sigma for each peak is calculated. The tracks that have a distance to the nominal collision vertex larger than 2.5 times the respective y and z are discarded. This is possible because of the clean m^2 distribution of the particles (it is possible to easily distinguish between protons,kaons and deuterons).

From this point on, the described cut will be defined as an "elliptical cut" and is calculated using:

$$\frac{(VtY - VtY_{Off})^2}{(2.5 \cdot \sigma_y)^2} + \frac{(VtZ - VtZ_{Off})^2}{(2.5 \cdot \sigma_z)^2} < 1 \tag{5.1}$$

where VtY, VtZ are respectively TPM1 track pointing on y and z axes, VtY_{Off}, VtZ_{Off} are the vertex offsets and σ_y, σ_z are the respective sigma for the fitted Gaussian.

Figure 5.2 shows the effect of the condition expressed in equation 5.1 in 2 dimensions.

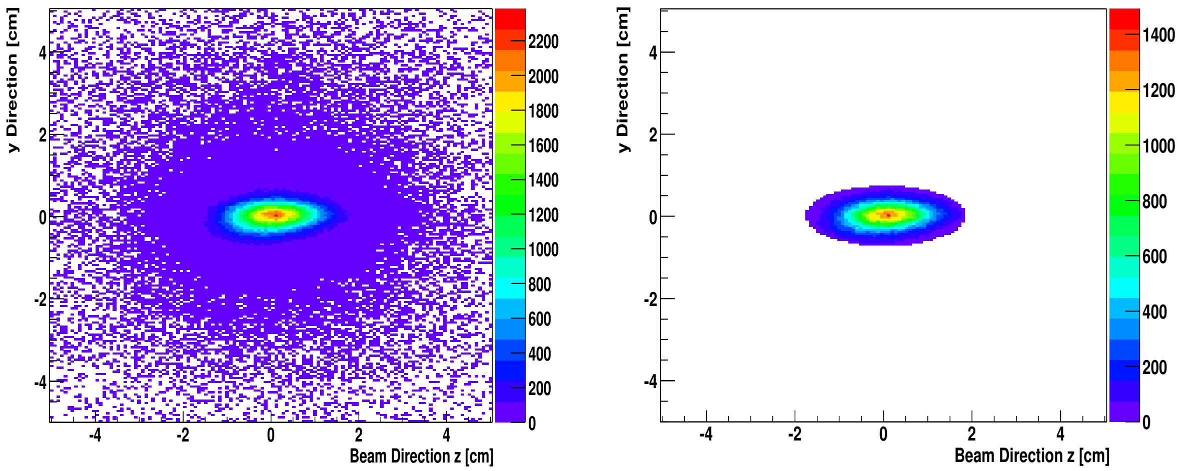

Figure 5.2: The histogram on the left shows all tracks found in TPM1 as they are directed back to the beam line. The right histogram shows the accepted tracks after the cut. Data is taken from B = 1/2B_{tot} field for MRS = 90° and include all particles detected.

Figure 5.3 shows the effect of the global and local cuts in reducing the background. In the figure on the left the global cuts mentioned above had been applied. The picture on the right is made after the elliptical cut. One can observe how good is the "cleaning" of the background.

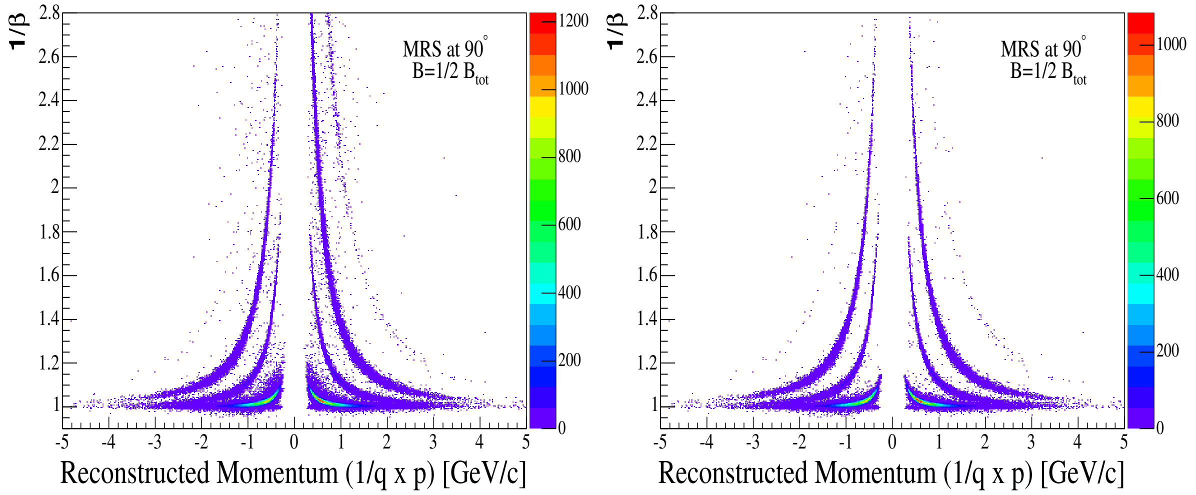

Figure 5.3: TOF in function of reconstructed momentum before (left) and after (right) elliptical cuts.

When the elliptical cut is applied, a part of the background is automatically included. This is shown in figure 5.4 (red dashed area). Since the error introduced is small i.e. less than 3% (see [47]), the correction is not applied in this work. The number of background particles that survive the cuts can be estimated by fitting the measured background outside the cuts, as shown in figure 5.4. The logarithmic scale permits the identification of a second lower Gaussian "hill" which is the background due to interactions of the particles in the tube with the beam pipe. Details about the removal of background can be found in [47].

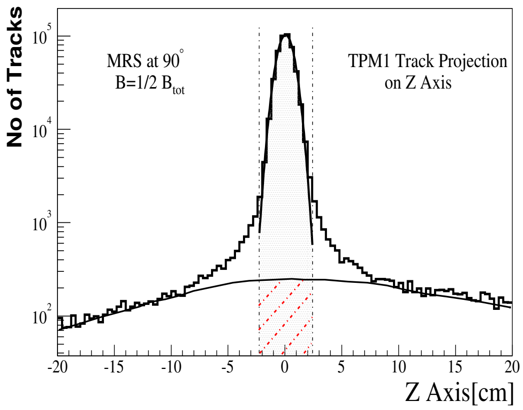

Figure 5.4: TPM1 pointed tracks to the nominal collision vertex.

5.3.2 PID

From the momentum and velocity of the particle (see 4.3.2 and 4.4.1) it is possible to determine the mass squared m^2 as:

$$m^2 = \frac{p^2}{\gamma\beta^2} = p^2(\frac{1}{\beta^2} - 1) \tag{5.2}$$

The TOF resolution is 85 ps for TOF1 and TOF2, 100 ps for TOFW. Figure 5.5 shows PID for protons and deuterons with the MRS located at 90 ° and a field of $1/2B_{tot}$. The theoretical expectations values of the different particle types are represented by the dashed curves, which follow the equation:

$$1/\beta = \sqrt{\frac{m^2}{1+p^2}} \tag{5.3}$$

where $1/\beta$ is the time that the particle takes to traverse the distance from the nominal interaction point and the TOFW i.e. where it is detected; m and p are the mass and momentum of the particle, respectively.

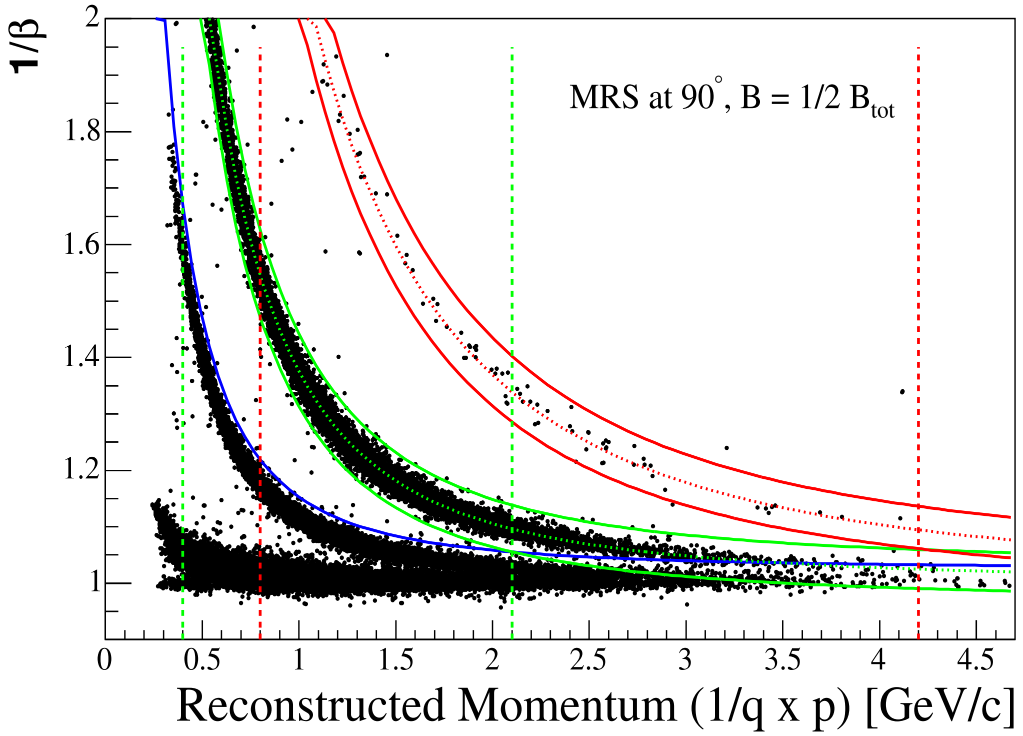

Figure 5.5: TOF PID for protons and deuterons with theoretical curves, green and red respectively. The blue lines are the upper theoretical lines for the kaons.

The solid curves delimit the particle selection. They correspond to $n \cdot \sigma$ cut above and below the expected $1/\beta$ versus p dependence (dashed lines), assuming a certain TOF and p resolution. The equations are:

$$1/\beta = \sqrt{\frac{m^2}{(p \mp \sigma_p)^2+1}} \pm \sigma_{1/\beta} \tag{5.4}$$

where σ_p is the momentum resolution and $\sigma_{1/\beta}$ is the $1/\beta$ resolution determined from the TOF measurements. The value 0.03 ps for the $1/\beta$ resolution is derived from the

TOFW time resolution of 100 ps. The σ_p value in principle depends on the momentum, but here it is set to 0.05 ps to both open up the selection curves at a lower momentum and to get the desired particles. A 2.5σ cut is applied. This cut identifies close to 100% of the particles in the "good" momentum ranges and cuts away most of the background.

Equation 5.4 gives 2 curves. One lies higher in TOF with respect to the correspondent theoretical (dashed) curve, and the other lies lower. Particles are selected between these curves. With this PID method it is possible to separate kaons to protons up to 2.1 GeV and protons to deuterons up to 4.2 GeV (see figure 5.5).

The highest kaons theoretical lines intersect the lowest proton lines around 2.1 Gev. Therefore, at that point there is an area between the blue and green lines in which it is not possible to distinguish between kaons and protons for higher momentum. The same happens for protons and deuterons at 4.2 GeV.

Figure 5.6 shows the effects of global, local and PID cuts on the mass squared distribution for different settings of the MRS and different momentum ranges. Histogram (a) shows m^2 at 90° between $0.4 < p < 2.1$ GeV/c. 0.4 GeV/c is the lowest momentum for which it is possible to identify protons. At lower momentum the multiple scattering becomes too high and the momentum resolution deteriorates. In the momentum range shown in (a) it is important to be able to distinguish between protons and kaons, and a nice separation between the two peaks (kaon peak is on the left) can be observed.

Histogram (b) shows m^2 distribution at the same MRS setting but in the momentum range $0.6 < p < 4$ GeV/c. Here a clear separation between protons and deuterons can be observed.

Histogram (c) and (d) show m^2 distribution for MRS at 35° (y $\approx$ 0.9), and more background can be observed. For B_2 calculation only deuterons from histogram (d) are taken and only protons from histogram (c) are taken. This is because of the PID limitations shown in figure 5.5.

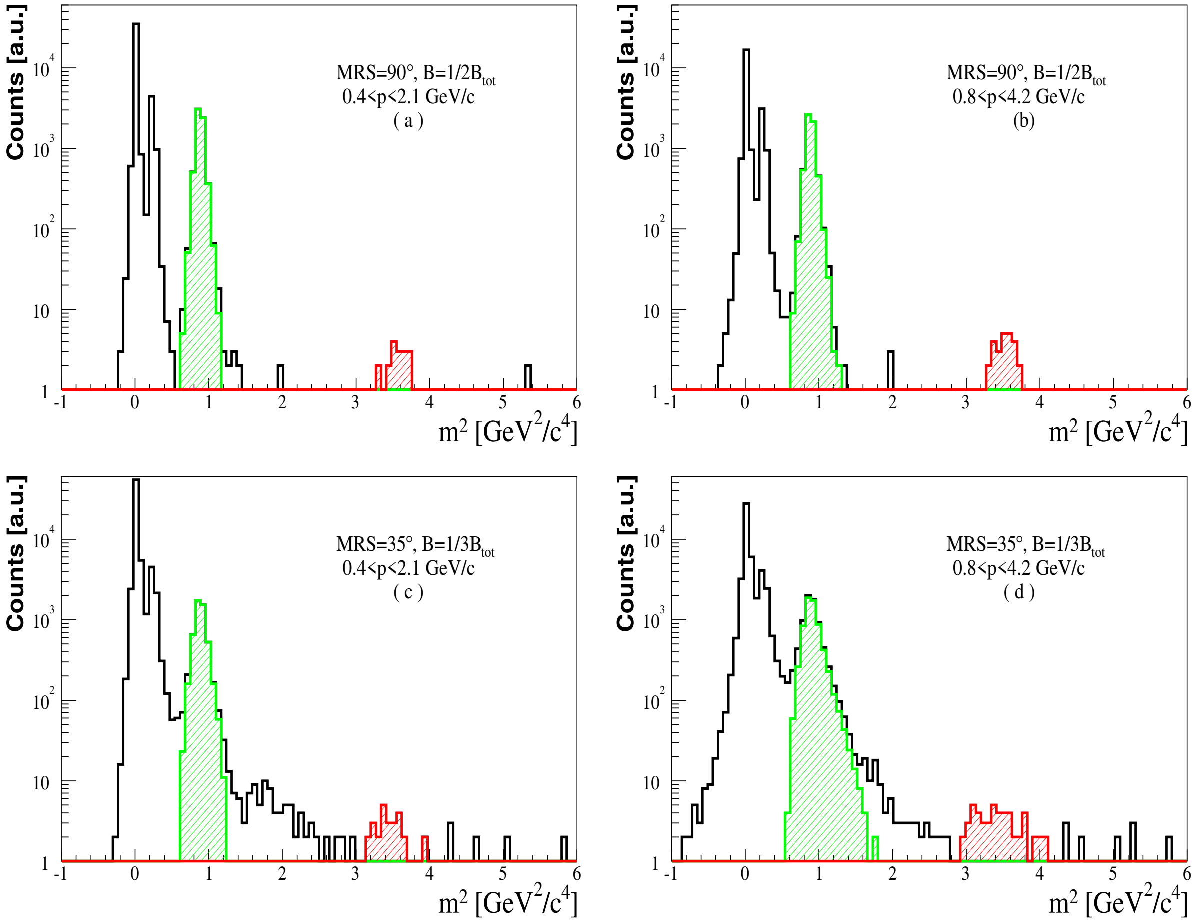

Figure 5.6: Mass squared distribution for MRS at 90° and 35°. The green area indicates protons, the red are deuterons. The black lines depict m^2 distribution of π, K, p and deuterons detected by TOFW in the indicated momentum range after the global and local cuts. The colored areas show the same distributions after the PID selection method described previously.

5.3.3 Rapidity Selection

When all the fiducial cuts and the PID selection method has been applied, it is possible to identify protons and deuterons. In order to determine the B_2 coalescence factor one must compare protons and deuterons at the same rapidity and at p_t and $2p_t$ respectively.

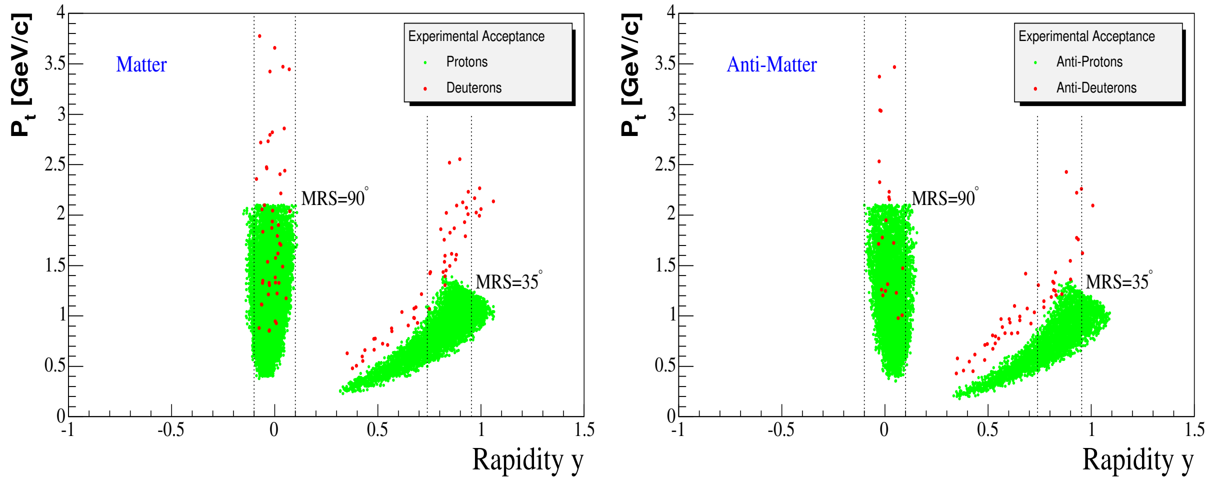

Figure 5.7: MRS acceptance with rapidity cuts for (anti–)protons and (anti–)deuterons at an MRS angle of 90° (left) and 35° (right). Protons are in a momentum range between 0.4 and 2.1 GeV/c (best PID for protons), while deuterons between 0.8 and 4.2 GeV/c (best PID for deuterons).

This process starts with plotting the p_t versus y acceptance distribution of the identified (anti–)particles, and then applying the appropriate rapidity cuts. Figure 5.7 shows acceptance for positive(negative) particles at 90° and 35°. The dotted lines represent the applied rapidity cuts. At 90° they are $-0.11 < y < 0.11$ while at 35° $0.74 < y < 0.95$. The cuts are chosen to include the widest p_T distribution of deuterons and protons as possible. At the same time the cuts cannot be too wide, or the resulting distribution will be too diverse.

For reference, the number of (anti–)deuterons in the selected rapidity ranges is (21)49 at 90° and (17)26 at 35°.

The total of measured events in the selected vertex range (trigger six) are 3304321 at 90°, 674289 at 35°.

5.4 Data Correction and Tools

There are essentially two types of corrections to be applied to the data:

1. In regard to spectrometers, geometrical acceptance relates to the position and mag-

netic field of the spectrometers, and the efficiency, relates to the hardware performance of the detectors.

2. In regard to physics, one must correct all the secondary interactions such as particle decay, multiple scattering, particle knock out from beam pipe material, particle absorption etc.

For each of these items a different kind of simulation is required. In the first case the simulation (using BRAG) produces *acceptance maps* (which are independent of the input event generator), in the second HIJING and BRAG must include all the physical interactions (this step is model dependent).

Simulations are made in order to find p_T dependent correction factors for the above mentioned effects, to apply them to the real data. The physics of the simulation has to be as close as possible to the real experimental data.

In the first part of the chapter an overview over the simulation tools used in this work is given. In the second part the corrections are described.

5.4.1 Event Generators

Models have been developed to describe the physics evolution in high energy collisions. Several current *event generators* essentially reproduce main feature of the collisions and the particle production between elementary particles or nuclei.

Event generators are very important in the field of relativistic heavy ion collisions since they are essential tools in the design and testing of heavy ion experiments. Furthermore it is possible to make predictions, compare results and can be used to correct data as it is done in this work.

Table 5.1 summarizes the most used models in the field.

Event generator	**Type**	**Comment**
FRITJOF	Hadronic transport	Classical strings
VENUS	Hadronic transport	Relativistic strings
HIJING	Parton cascade	pQCD, jet quenching, shadowing
neXus	Parton cascade	Universality hypothesis
UrQMD	Quantum field approach	Complex re–scattering

Table 5.1: Event generators. The HIJING model is used in this work.

HIJING

HIJING (Heavy–Ion Jet Interaction Generator) uses transport theory to evolve partonic degrees of freedom. This model explores the consequences of hard parton scatterings. The physics behind the program includes multiple mini–jet production, soft excitations, nuclear shadowing of parton distribution functions and jet interactions in dense matter. The success of HIJING was the prediction of the charged multiplicity $dN/d\eta$ at mid–rapidity in $\sqrt{s_{NN}}$ = 56 GeV and 130 GeV collisions at RHIC [48]. Unlike FRITJOF, HIJING allows the excited strings to de–excite via subsequent interactions, treated like ordinary nucleon–nucleon collisions. This is the event generator used in this work. The reason is the mentioned good agreement of $dN/d\eta$ at mid–rapidity. Furthermore compared with other models HIJING gives the best description of net–proton densities for the recent central Au+Au collisions at $\sqrt{s_{NN}}$ = 200 GeV.

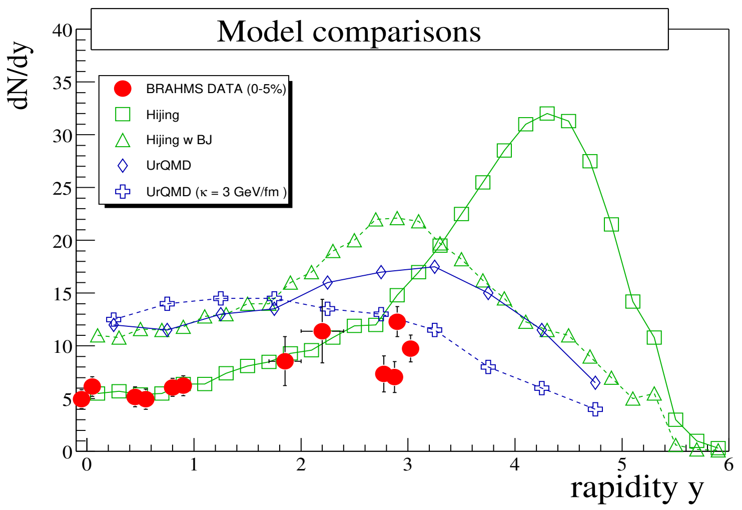

Figure 5.8: Net–proton multiplicity compared to model predictions (taken from [7]).

Finally HIJING is used in many experiments and therefore easy to compare.

5.4.2 Simulation Tools

The BRAHMS simulation package which contains specific detector geometry for the detector setup, is BRahms Analysis GEANT (BRAG). GEANT (GEometry ANd Tracking) is a CERN developed Monte Carlo tool.

GEANT

The GEANT framework simulates the interaction of elementary and composite particles with matter, and in particular the response of particle detectors being hit by a particular particle with a given momentum. This Monte Carlo based detector simulation package is therefore used to optimize and develop detectors in general, to test tracking and analysis programs, and to interpret the experimental data. This simulation is the only way to correct experimental data for secondary particles in the background and the effect of nearby dense material like magnets or detectors stands.

The input for GEANT simulations can be either output data from models as described previously, or a starting point and momentum vector of a specific particle.

BRAG

BRAG is the GEANT simulation package for BRAHMS. It contains the specific detector geometry for the detector setup. HIJING and FRITJOF events are often used as input events for BRAG.

The output of a simulation consists of four files containing settings for the magnet, geometry and the field used (figure 5.9). The *.cdat* files contain information of all particles like PID, mass, momentum, TOF etc.

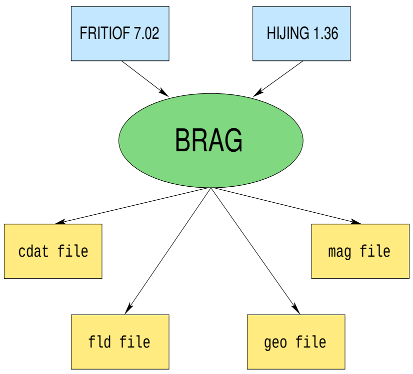

Figure 5.9: BRAG output files.

5.5 Acceptance Corrections

The measured spectra of raw particle depend on the geometrical coverage (position of detectors relative to beam pipe), vertex position and the magnitude of the magnetic field. Therefore it is necessary to prevent these faults by applying an acceptance correction. In this way the measured yields obtained are in principle independent on the experimental setup.

In the BRAG simulations a flat distribution in p, θ and ϕ of pions is thrown within the desired p, ϕ and θ range through the spectrometers, for the different values of the magnet field. At relativistic energies most particles leave the same amount of energy by ionizing matter that they traverse (MIP:minimum ionizing particle). Thus, acceptance maps for other species of particles are calculated by substituting the mass and recalculating rapidity. Figure 5.10 shows an example of a BRAG simulation.

In the simulations particles are required to leave a track in TPM1, TPM2, pass through D5 (within the applied fiducial cut) and to be detected in TOFW. The spectra of these "accepted" particles will be mapped in y versus p_t and then divided by the spectra of the thrown particles. The geometrical acceptance correction factor is obtained in the following way:

$$ACC(y, p_T) = \frac{BRAG_{acc}(y, p_T)}{BRAG_{thr}(y, p_T)} \times \frac{\Delta\phi}{2\pi} \tag{5.5}$$

where $BRAG_{acc}$ are the accepted pions in the rapidity interval after the mentioned requirements, $BRAG_{thr}$ are the initial pions thrown in a flat distribution. The scale factor, $\frac{\Delta\phi}{2\pi}$, is used because the particles are not distributed evenly through ϕ, but rather in a limited range, covering the first magnet's vertical aperture in the spectrometer.

From the simulation, eight acceptance maps are obtained, where the transverse momentum is plotted as a function of rapidity. Each map covers a 5 cm wide vertex bin

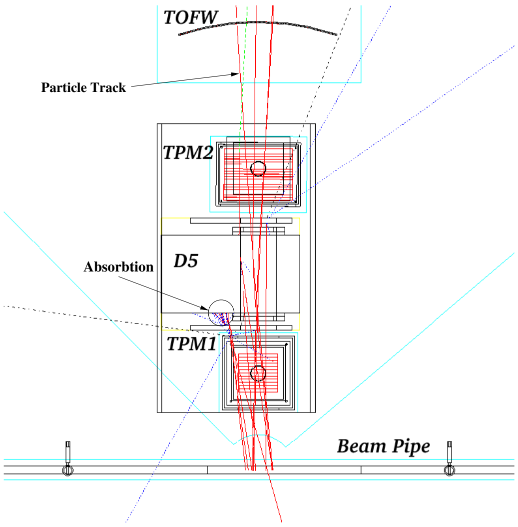

Figure 5.10: BRAG simulation of pions thrown through MRS spectrometer. If ten pions are thrown with a flat distribution in the range of $100° < \theta < 80°$ and $-2° < \phi < 2°$, about three are accepted. This is consistent with the opening of the magnet which is $\Delta\theta \approx 8.8°$ and $\Delta\phi \approx 2.5°$. D5 field is 2.16 kGauss, momentum of pions between 0.1 and 2.0 GeV. The red lines represent the particle tracks through the detector. Note that in the acceptance map simulation no secondary particles production is included [33].

between -20 to 20 cm from the nominated interaction point. The transverse momentum range goes from 0.1 to 4.0 GeV/c and is divided in bins of 50 MeV/c.

The same momentum and rapidity cuts of the data are applied to each of these maps. Then the acceptance maps will be projected in p_t. The respective values in the unit rapidity for each p_t point are summed and then normalized for the number of bins in one unit rapidity. This can be seen in equation 5.6:

$$< P >= \frac{\sum_{y_i} P(y_i)}{Nbin_y} \tag{5.6}$$

where P is the "probability" to have a particle in that region of phase–space, y_i is the i–bin of rapidity and N_y is the number of bins corresponding to the unit of rapidity.

Next, one must sum all the maps, each weighted by the number of events in the respective vertex bin, and normalize the result with the total number of events. A global map which covers the vertex range between -20 and 20 cm is obtained (figure 5.11). The raw spectra will be divided by this map. The acceptance is not divided by the data vertex–bin by vertex–bin because there are few deuterons, which could result in more errors. The proton spectra analyzed in this way agree with the results of other analyses in which each vertex bin is corrected separately.

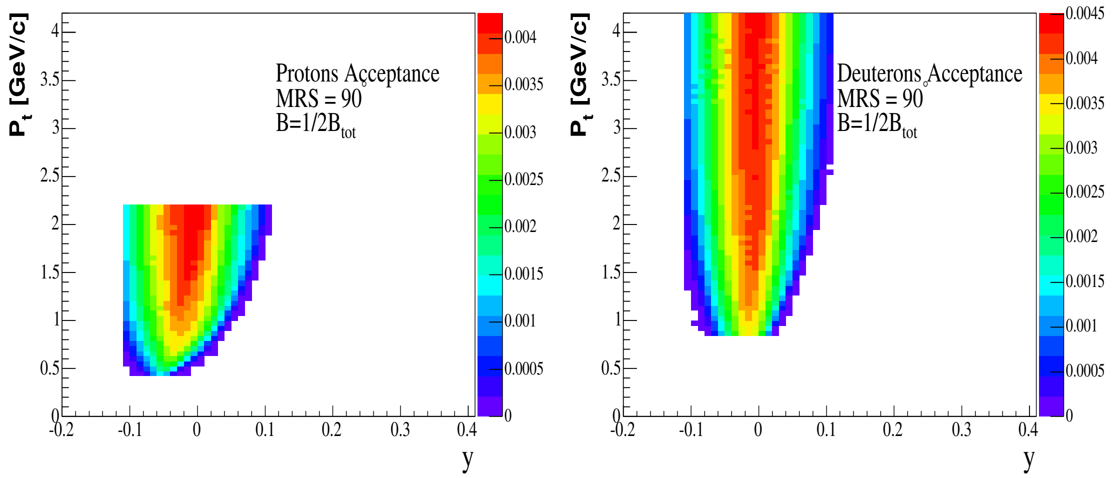

Figure 5.11: Acceptance maps for protons and deuterons at MRS = 90°. Momentum and rapidity cuts (the same of experimental data) are already applied. This is the reason why the protons and deuterons maps are "cut" at p_T = 0.4, 2.1 GeV/c (left) and p_T = 0.8, 4.2 GeV/c (right) respectively. The different colors corresponds to the different values gives by equation 5.5.

5.6 Detectors Efficiencies

There are two methods of determining detector efficiency corrections in MRS, including checking the efficiency of the track reconstruction (TPC's) and PID (TOFW). Because correcting for efficiencies is not the main aim of this work, it will only be briefly explained. These procedures are described in detail (also for FS) in the recent work [7].

Tracking efficiency in MRS TPC's is studied with the "track embedding method". Here a simulated track with a well defined momentum and PID is inserted into a real event at the raw data level. Using the tracking software,one can determine how often simulated tracks are found by counting the number of hits in the TPC. Then the reconstructed tracks are compared to the known track originally inserted in the event. If the overlap is greater then 60% the track is said to be reconstructed. It turns out that the efficiency curves are linear and decrease as the number of hits increase.

There are two components for the TOFW efficiency calculation. In one the bad slats and outer slats (due to poor statistics) have been ignored. The corresponding cuts were applied in the respective acceptance maps so that the same phase space region $y - p_T$ is covered. The other component includes the working slats. The corrections are applied due to *multiple hits* (two or more tracks associated to the same hit are ignored) and missing hits due to the shape of TOWF (tracks can pass through the wrapping of the slats or the energy deposited is too low due to the path length of the detector is short). For the working slats the efficiency found is $\sim 93 \pm 2\%$.

5.7 Corrections due to Secondaries

Simulations are necessary to correct the measured p, pbar, d and dbar for particles originating from decays or other secondary reactions. A typical example are protons from Λ decays: $c\tau(\Lambda) \sim 7.89$ cm. Therefore lambdas decays well outside the fireball. The protons cannot coalesce with neutrons to form deuterons and will lower B_2 making the volume seem larger than it is. BRAG simulation with realistic input distributions determine the distribution of these particles in the spectrometer.Using this information it is possible to distinguish between primary and secondary tracks, i.e. from decays and production in beam pipe, magnets, etc.

An intensive study of all these effects for (anti–)protons, (anti–)deuterons production and absorption has been made and will be presented in the following.

First, full **HIJING simulations** of events over a 4π solid angle are generated. Collisions between two Gold nuclei at $\sqrt{s_{NN}} = 200$ GeV are generated. The centrality of the collision is set up to be 10% i.e. $0 \lesssim b \lesssim 5\ fm$.

In the second step the particles generated by HIJING are propagated through BRAHMS spectrometers in the selected phase–space range, using the BRAG environment. The experimental data come from 90° and 35° settings. Thus, in the first case the relevant phase space is $-30° < \phi < 30°$, $60° < \theta < 120°$ and in the second $-30° < \phi < 30°$, $5° < \theta < 65°$.

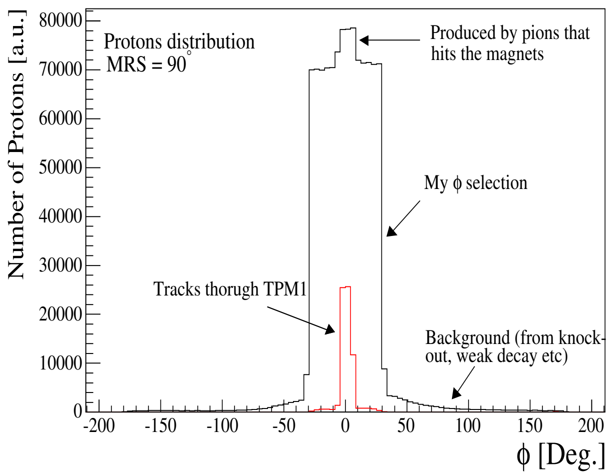

Figure 5.12: GEANT protons distribution as a function of azimuthal angle ϕ. For this figure 360000 events were used.

For MRS simulations at 90° the GEANT magnet field is set to $1/2B_{tot}$, and for 35° it is set to $1/3B_{tot}$, corresponding to the settings at which the data was recorded. All of the physical effects are turned on, including particle decay, re–scattering, particle absorption, interaction with the beam pipe, etc. In this way, the simulations are as close as possible to the experimental data.

After the BRAG simulation two sets (MRS = 90° and one for MRS = 35°) of *.cdat* files are produced, each containing the results of $6 \cdot 10^5$ HIJING events (collisions) propagated through the BRAHMS detectors.

Figure 5.12 shows all protons (plotted in function of the azimuthal angle ϕ) produced after sending the particles from the event generator HIJING through the BRAHMS simulated spectrometers using BRAG application.

The same elliptical cut (i.e. the same values of the experimental σ_y and σ_z of the distributions in z and y of TPM1 tracks, projected back to the interaction point) is applied to the simulated data. Figure 5.13 shows the projection of TPM1 tracks in the y axis and the cuts applied.

In the real experiment the resolution of the tracks in TPM1 is not perfect since there is uncertainty in the measurement of the track position. This is not included in the simulation.

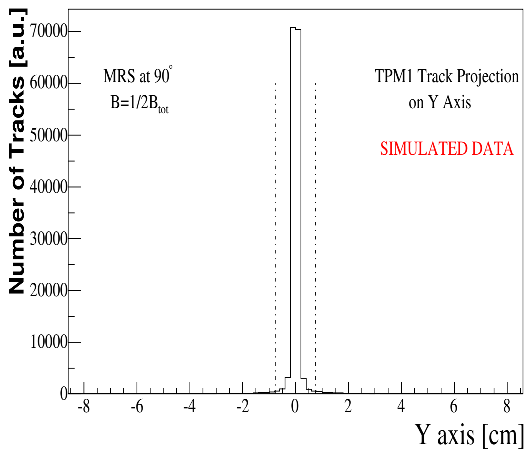

Figure 5.13: Simulated TPM1 tracks projection on y axis with vertex cuts.

This makes the width of the experimental Gaussian larger than the simulated Gaussian. Nevertheless, the expected sigma due to the intrinsic resolution of TPC's is small (excluding multiple scattering and other physical processes); one would expect the same size as the contribution from digitalization[4] if the simulation was realistic. It is an order of ∼1-2 mrad for TPM1 (see also [49]), which corresponds to ∼1-2 mm in sigma of x at beam. Compared to the width of distribution from contributions from weak decays, which are substantially bigger than ∼1-2 mm, one can assume that the error introduced is negligible.

5.7.1 Corrections for Particles Production

In this section the possible sources of secondary deuterons and protons (and respective anti–particles) will be examined. If the effect is significant (i.e. $> 1\%$), a correction factor will be calculated.

Protons production: Secondary protons are produced by inelastic scattering in the beam pipe, air, detectors etc. Weak–decay from hyperon is the main source of secondary protons measured.

Anti–protons production: There should be very few anti–protons produced. In fact no anti–protons are in the material surrounding the experiment, and anti–protons should therefore arise only from pair production. The energy required for this reaction is ~ 2 GeV (in the center of mass system).

Deuterons production: Produced mainly from knock out from very light nuclei, mainly from beryllium (Be) pipe.

Anti–deuterons production: No knockout is possible, the only contribution comes from pair production. It should be the same as for deuterons.

Compared to the measurements from STAR [50], HIJING underestimates the number

[4]Process to simulate the uncertainty of the resolution of the tracks in TPM1

of lambda particles produced in the collision. Therefore, in order to obtain correct results, it is necessary to correct for this effect.

The measured dn/dy ratio of lambda to protons at mid–rapidity is taken from [51] and [50], and is ~ 0.89. Since the 200 GeV results are similar to 130 GeV ones, the ratio is assumed to be the same.

The same ratio is calculated using HIJING simulation (see figure 5.15). Since HIJING does not reproduce the observed ratios, the HIJING number of lambdas will be scaled to the measured ratios.

Lambda particles are produced directly and in the following decays:

$$\begin{array}{lcll} \Sigma^0 & \rightarrow & \Lambda + \gamma & (100\%) \\ \Xi^0 & \rightarrow & \Lambda + \pi^0 & (100\%) \\ \Xi^- & \rightarrow & \Lambda + \pi^- & (100\%) \\ \Omega^- & \rightarrow & \Lambda + K^- & (67.8\% - negligible) \end{array} \tag{5.7}$$

The contribution of omega particles is negligible, as can also be seen in figure 5.14, which shows the expected relative yields of hyperons (HIJING model). HIJING ratio between the particles above and the protons in dn/dy at mid–rapidity has been calculated to be 0.38. The ratio does not change significantly for MRS at 35°.

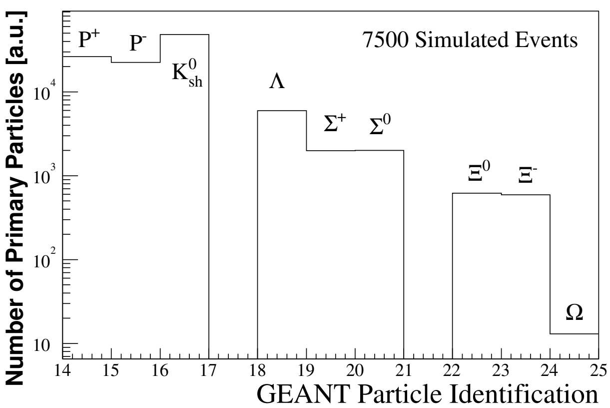

Figure 5.14: HIJING original particles identification distribution. The GEANT particle identification and relative abundance of the thrown particles is shown.

The HIJING lambda scaling factor is therefore:

$$\begin{array}{ll} C_{H\Lambda} = \frac{0.89}{0.38} = 2.34 & (Particles) \\ C_{H\bar{\Lambda}} = \frac{0.95}{0.41} = 2.31 & (Anti-Particles) \end{array} \tag{5.8}$$

This factor has been used to scale the lambda yield for the calculation of the weak decay correction factor.

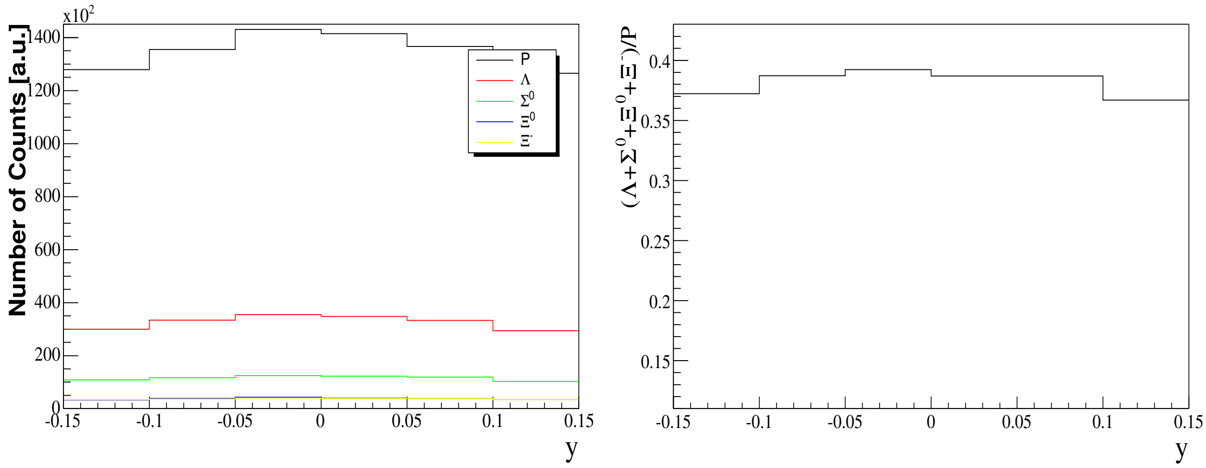

Figure 5.15: On the left: Rapidity distribution of HIJING positive particles thrown at mid–rapidity in the range $-30° < \phi < 30°$, $60° < \theta < 120°$. On the right: dn/dy ratio of particles shown at left and protons at mid–rapidity.

WEAK DECAY

Hyperons like Λ and Σ^+ decay outside the fireball by *weak decay* and produce protons, some of which are detected. Therefore, the number of measured protons is larger than the number of "original" protons and should not be used directly in the calculation of B_2. The decay modes of Λ and Σ^+ are the following:

$$\begin{array}{lcll} \Lambda & \rightarrow & p + \pi^- & (63.9\%) \\ \Lambda & \rightarrow & n + \pi^0 & (35.80\%) \\ \Sigma^+ & \rightarrow & p + \pi^0 & (51.57\%) \\ \Sigma^+ & \rightarrow & n + \pi^+ & (48.30\%) \end{array} \tag{5.9}$$

The mean lifetime for Λ is approximately $2.6 \cdot 10^{-10}$ s and for Σ is $0.7 \cdot 10^{-10} s$.

Some of the protons produced are reconstructed as original protons. It is therefore necessary to introduce a momentum–dependent *weak decay correction factor*. For a given p_T bin the total weak decay correction is calculated from the simulation as:

$$C_W(P_t) = \frac{N_p^d(p_T)}{N_p^d(p_T) + C_{H\Lambda} \cdot N_p^{\Lambda}(p_T) + N_p^{\Sigma}(p_T)} \tag{5.10}$$

where N_p^d is the number of direct protons detected, $C_{H\Lambda}$ is the HIJING model dependence correction factor for lambda (see eq. 5.8), N_p^{Λ} the number of protons from lambda detected, and N_p^{Σ} is the number of detected protons from sigma.

It has been chosen not to alter the HIJING correction factor for Σ because no documentation for the measurement of these particles is yet available at RHIC.

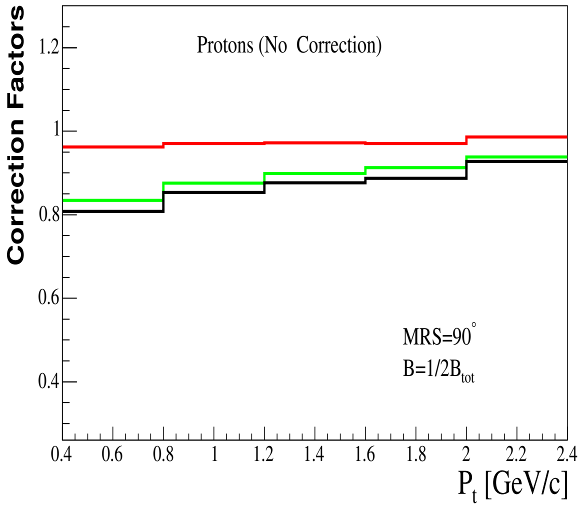

Figure 5.16: HIJING weak decay correction factors versus p_T for protons at mid–rapidity. Red, green and black lines indicate respectively Σ, Λ and total $(\Sigma + \Lambda)$ corrections.

Figure 5.16 shows HIJING pure correction factors (i.e. without applying the factor $C_{H\Lambda}$) at mid–rapidity, while figure 5.17 shows HIJING correction after applying the factor $C_{H\Lambda}$.

Figure 5.17 (see next page) shows HIJING weak decay correction factors for particles and anti–particles at 90° and 35°.

The correction factor distribution in function of p_t must be multiplied to the proton p_T distributions to correct the proton sample. One observes that the weak decay correction has a significant effect on the final transverse proton spectra.

On average the correction for protons in the regions of interest for B_2 calculation ($0.4 < p < 2.1$ GeV/c) is a factor of 23% and 20% for MRS = 90°, B = 1/2B$_{tot}$ and MRS = 35°, B = 1/3B$_{tot}$ respectively.

Production of deuterons and anti–deuterons by feed–down (from fragmentation of heavier clusters) is negligible.

KNOCK–OUT FROM BEAM PIPE

The number of measured protons must also be corrected for the *knockout* protons, which are produced mainly by the interaction of pions, kaons and protons with nuclei in the beam pipe. They are also generated from interactions with air molecules, and with spectrometer material.

The study of the knock–out effect is done with the $6 \cdot 10^5$ HIJING events used as an input for BRAG, at mid–rapidity and MRS = 35°.

The predictions of HIJING model agrees well with the observed charged multiplicity, and since the pion is the particle that mainly produces the knock out protons (which compared to lambda decays is very low), the estimates should be reasonably good.

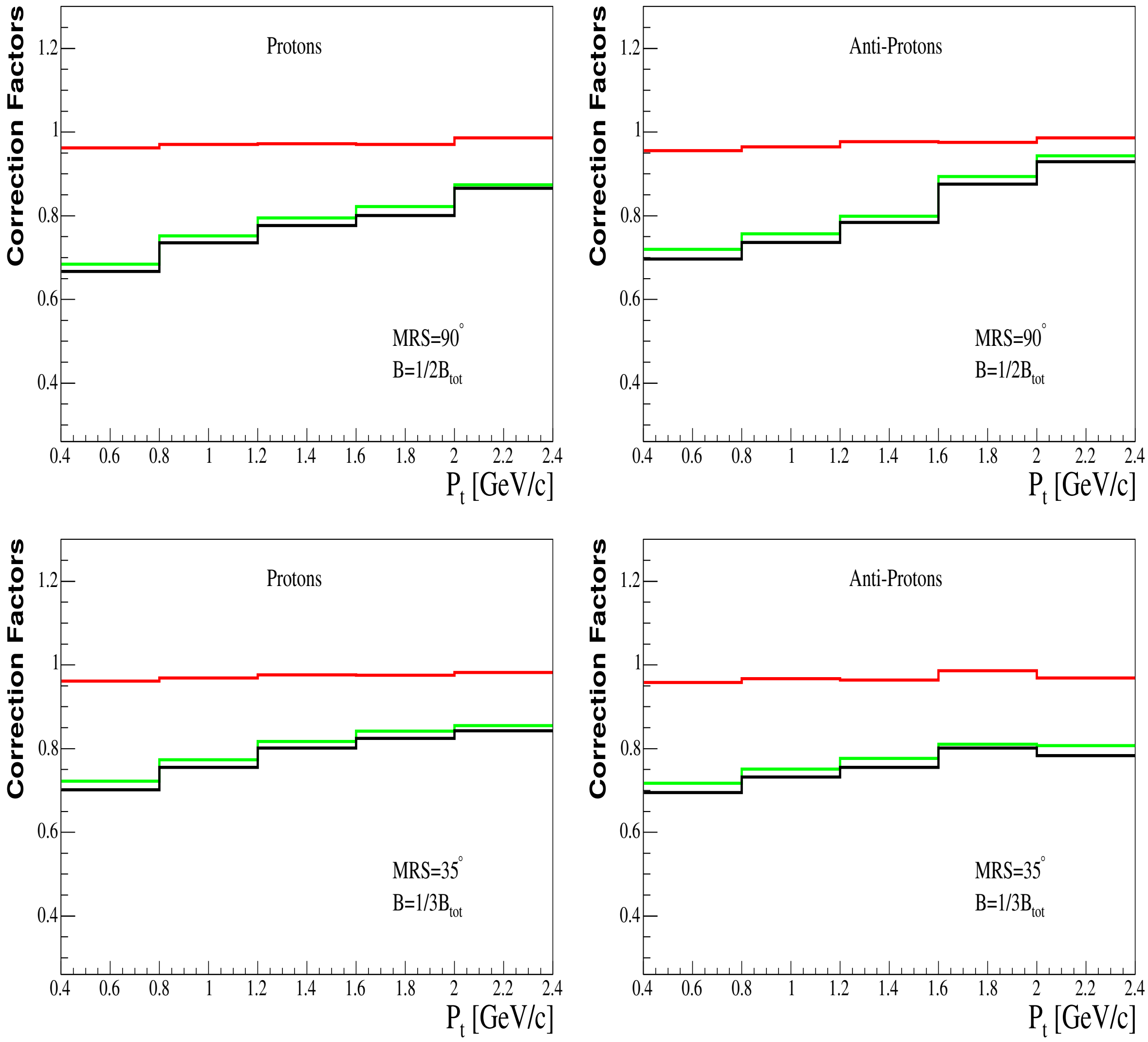

Figure 5.17: HIJING weak decay correction factors after rescaling to measured hyperons yields versus p_T for protons and anti–protons at the respective settings. Red line: Σ correction, green line: Λ correction, black line: total correction.

Figures 5.19 in the next page shows some results of the simulation. Protons which have pions, protons or kaons as *mother particle* are plotted. The protons are required to pass through TPM1, TPM2, D5 and hit TOFW. The same vertex cuts used in the experimental data are applied.

The condition “mother particle” has been implemented in the software and simply means “produced by”. this condition is used to see if, and how many, protons are produced by knock–out with the beam–pipe, air, magnets etc. For this study it would also have been possible to plot all the protons originating at a point inside the beam pipe material. However, this method is not so precise as the previous. In fact the number of protons were approximately the double. After an investigation it has been found that this was due to the lambda (and sigma) particles decay to protons exactly in the beam pipe region. Figure 5.18 shows protons production vertexes (i.e.) where protons are produced in the first 10 cm (x–y axes) of the HIJING simulation. The different colors correspond to different physical processes which generate protons. For this example only 7500 events are used and no conditions or cut are applied.

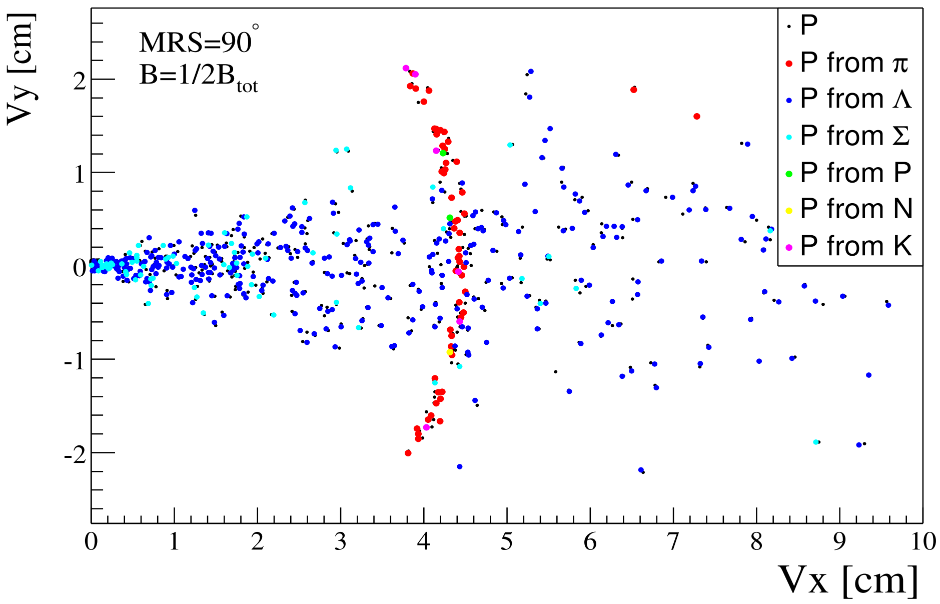

Figure 5.18: GEANT distribution of proton production vertexes due to different processes. The beam–pipe is at the point “0” on the y axis, perpendicular to the x–y plane. No cuts or conditions are applied. The ϕ angle of the thrown distribution can be seen.

From this figure it can be clearly seen that almost all of the knock–out protons are produced in the beam pipe by pions (in red), which draw the shape of the beam pipe.

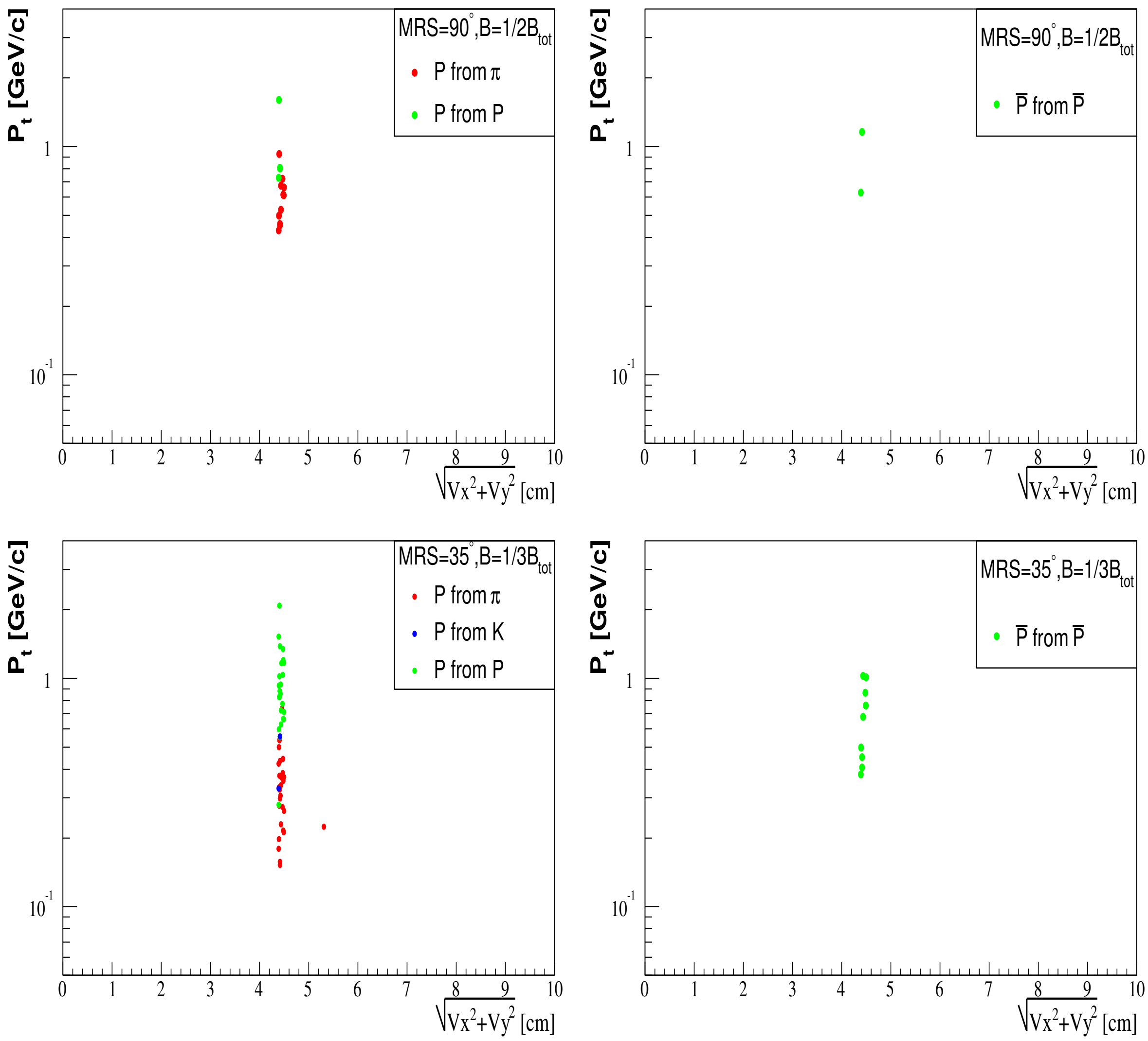

Figure 5.19: HIJING simulation: detected knock–out protons and anti–protons (all cuts are applied) in the respective MRS angles and with the indicated magnetic fields. The figure shows plotted transverse–momentum versus distance of the production vertexes from the interaction point. A logarithmic scale has been chosen in order to demonstrate that the average p_T of the particles is below or around one. The "isolated" proton at 35° is probably due to a collision of a pion with an air molecule. Since the simulation is done for $6 \cdot 10^5$ events, one can argue that corrections by knock–out with air molecules at these settings are negligible. See text for details.

Protons from lambda (blue) and sigma (light blue) decays are also plotted. Since there are many of such hyperons in this region, it can happen that they decay to protons exactly at the beam–pipe distance from the interaction point. This explains the larger number of protons detected with the second previously explained method.

The number of the detected–protons is very low compared to the large number of events in the simulation ($6 \cdot 10^5$). This is explained by the fact that at this setting the magnetic field deflects many of the produced low–momentum protons, the acceptance is small and very few protons are knocked out.

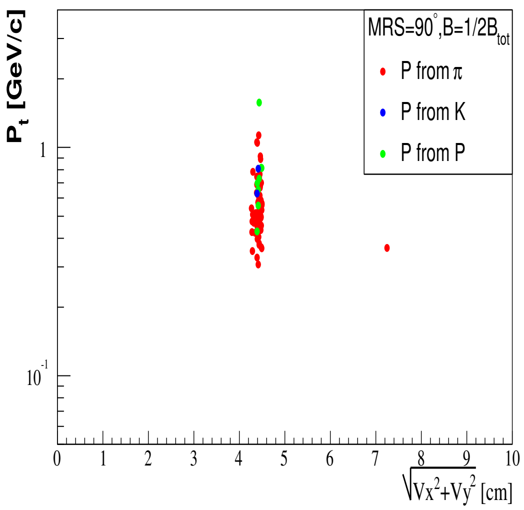

Figure 5.20: Detected knock–out protons without vertex cut.

Figure 5.20 shows the same plot as in figure 5.19 but without vertex cuts. From this picture one learns that the vertex cut excludes a relatively important number of knock–out protons which otherwise would be measured. The logarithmic scale is chosen in order to show that most of the protons have a $p_T < 1$ GeV/c.

In both figures one also observes that knock–out protons from pions have, on average, the lowest momentum. Next highest are protons from kaons, protons from protons have the highest momentum.

Since no deuterons at the used settings are detected in the simulations, and the momentum of deuterons used for the analysis is between 0.8 and 4.2 GeV/c, the corrections for knock–out deuterons are negligible. Furthermore, it comes out from the simulation that measured knock–out (anti–)protons at 90° and 35° are less a 1% of the total measured, and are therefore negligible.

Figure 5.21 shows proton production at mid–rapidity with a $B = 1/2B_{tot}$ magnetic field. The peak due to knock–out production can easily be seen at the beam–pipe distance from the collision vertex.

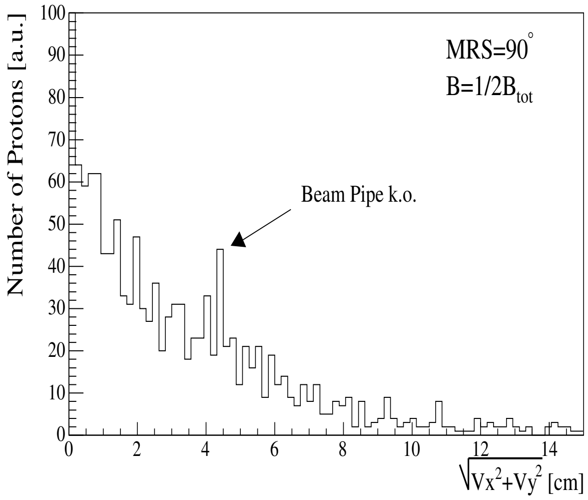

Figure 5.21: HIJING simulation of $6 \cdot 10^5$ events: measured protons after all cuts at 90° (left) and 35° (right). The protons from the collision are in the first bin of the histogram. All the others are generated by knock–out, weak decay etc. at the indicated distances from the collision point. Notice the proton peak at ~ 5 cm from the collision point, which corresponds to the distance of the beam pipe.

5.7.2 Corrections for Particles Absorption and Multiple Scattering

In this section the corrections applied to absorption and multiple scattering of protons and deuterons are discussed.

A particle is absorbed when it interacts inelastically with the nuclei of a medium. Absorption (abs) occurs mainly in beam pipe and air molecules. Absorption of particles in magnets or TPM1 materials is not taken into account since the particles are not detected by TOFW anyway.

Multiple scattering (ms) is the Coulomb elastic scattering of particles with the nuclei of the matter between the interaction point and the TOFW. This effect can deflect particles out of acceptance.

Using BRAG one can determine the magnitude of these effects. A flat distribution in momentum $0 < p < 4$ GeV/c, and θ, ($\pm 2°$ in the selected MRS setting) is generated and sent thorough the spectrometers, with only the physical process of interest (i.e. absorption or multiple scattering) on. An identical distribution is sent, but without any physical effect. The momentum–dependent correction is determined using the ratio of the first detected distribution divided by the second, and will be applied to the spectra before calculating B_2.

PROTONS-ANTI–PROTONS

Proton absorption and multiple scattering occurs mostly in beam pipe and air. Figure 5.22 shows the results of simulations for *ms* and *abs* (only anti–protons). In this set of simulations the corrections were obtained by digitizing the hits in detectors to include detector effects.

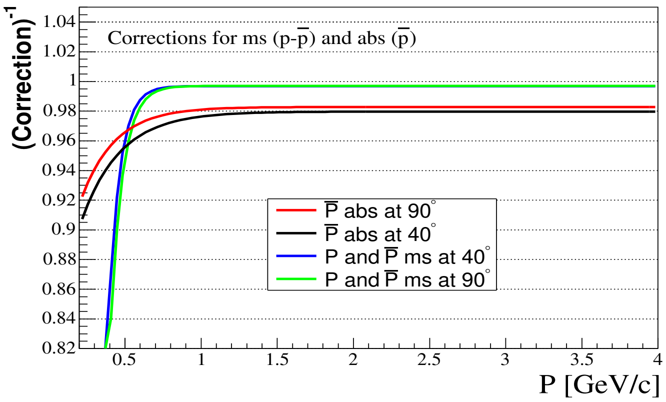

Figure 5.22: Momentum dependence of abs and ms correction at 90° and 40°. Here the simulated hits on detector are digitalized to include detector effects [52].

It can be observed that corrections are larger at smaller momenta. The multiple–scattering correction for angles lower than 40° has been found to be less than 1% and therefore negligible.

Corrections for anti–protons at mid–rapidity are in the order of 2% for $p > 1$GeV/c. For $p < 1$ GeV/c the correction becomes more consistent, and absorption occurs mostly in beam pipe and air.

New simulations have been made to calculate corrections for proton absorption at 90° and 35°. Here the simulated data are reconstructed in root files without digitalization. A simulation of anti–proton absorption ($1 \cdot 10^5$ fired anti–protons) at mid–rapidity checks for consistency in corrections. The result can be seen in figure 5.23, which shows a nice agreement with the corrections of figure 5.22. This can be an argument to confirm that the error introduced is negligible.

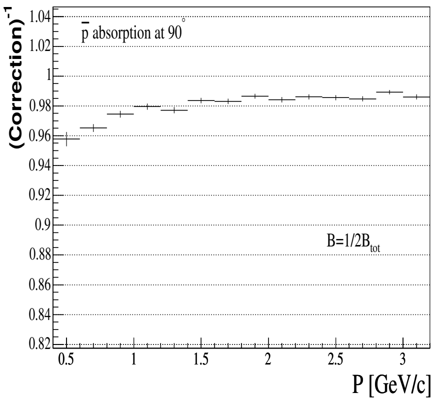

Figure 5.23: Anti–protons absorption correction. The reconstruction has been done without digitalization.

Figure 5.24 shows momentum–dependent correction for protons absorption at MRS = 90°, 35°. Absorption for protons at mid–rapidity results in the order of 1% for $p > 1$ GeV/c. At 35° the correction is almost of the same order, just a bit lower.

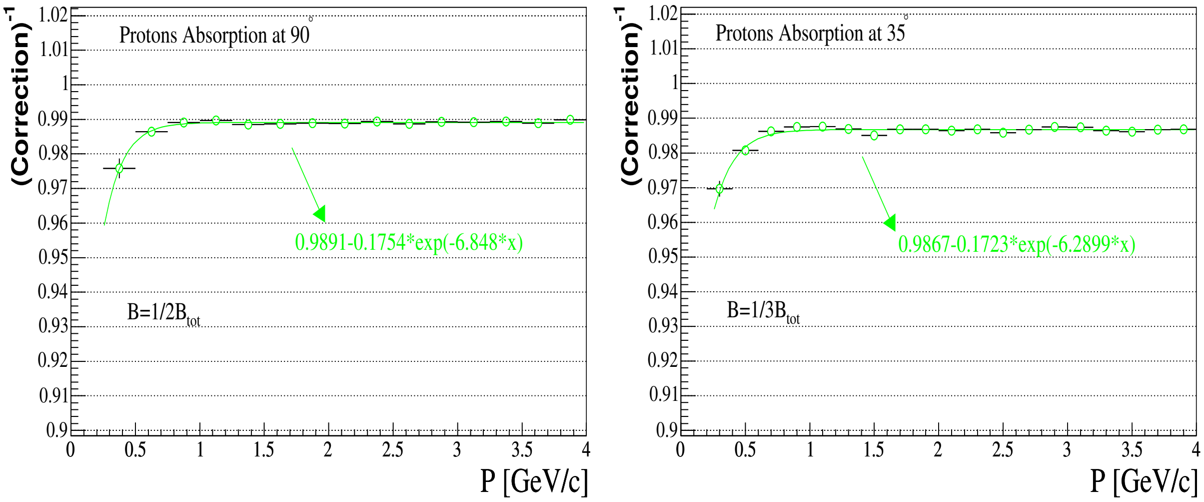

Figure 5.24: Fitted corrections for protons absorption at 90° and 35°.

DEUTERONS - ANTI–DEUTERONS

For deuterons, absorption occurs mostly in beam pipe and air. In the simulations a flat distribution in p_T of one million deuterons has been thrown through the spectrometers, first turning the physical effect of hadronization on, then turning it off. The only difference from the previous simulations is that here the hadronization interface is different, including interactions of deuterons.

The results are plotted in figure 5.25.

In principle, the absorption contributions should resemble that for protons, but with a higher cross section. It would be expected that for large deuteron energies (more than 1 GeV/c) the absorption should be the double of that for protons. This can clearly be seen if one looks at figure 5.24 and 5.25. At lower deuteron energies the Coulomb interaction plays a dominant role.

Anti–deuterons are not defined in GEANT. Therefore, for the above reasons, a good approximation takes the anti–proton absorption and multiplies it by 2. The neutron does not contribute to the total charge and is therefore ignored.

$$\frac{Corr_d}{Corr_p} = \frac{Corr_{dbar}}{Corr_{pbar}} \tag{5.11}$$

5.8 Statistical Errors

The general statistical error is the following:

$$Error = \sqrt{\sigma^2} \tag{5.12}$$

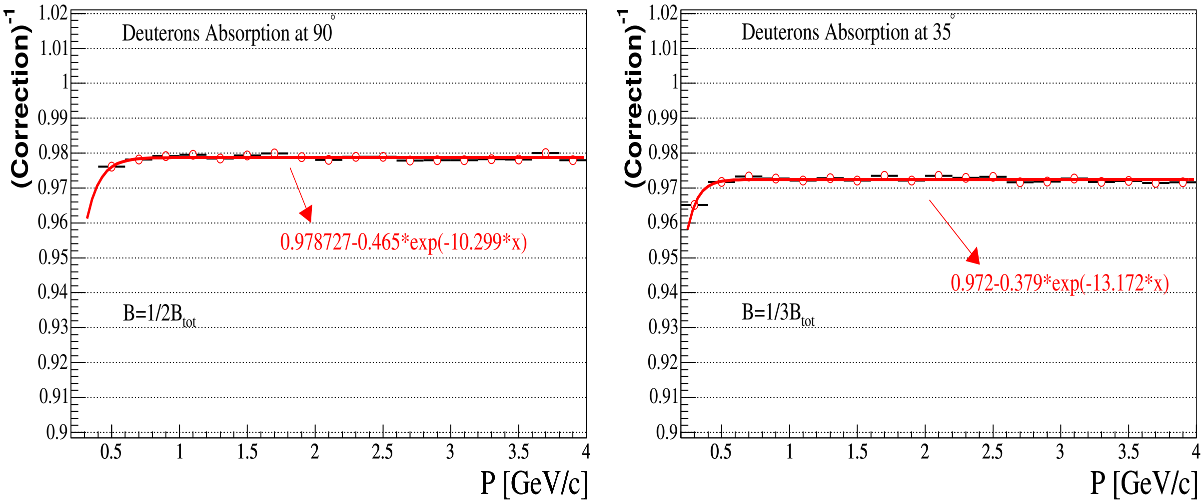

Figure 5.25: Fitted corrections for deuterons absorption at 90° and 35°.

where σ can be for protons (σ_p) or deuterons (σ_d). In order to calculate B_2, the number of protons (or deuterons) is obtained by counting bin by:

$$N = \sum_i (2\pi * p_T * bin - width * N_i)^2 \tag{5.13}$$

where N_i is the number of counts in that bin. The associated error is:

$$\sigma^2 = \sum_i (2\pi * p_T * bin - width * \sigma_i)^2 \tag{5.14}$$

where σ_i is the bin error. To calculate the error associated to B_2 one has to derive the formula:

$$B_2 = \frac{d}{p^2} \tag{5.15}$$

Deriving per parts one obtains from error propagation the error:

$$\sigma^2_{B_2} = (\frac{1}{p^2})^2 \sigma_d^2 + (\frac{2d}{p^3})\sigma_p^2 \tag{5.16}$$

5.9 Normalization

The particles distribution is identified after calibration, trigger selection, event selection, vertex selection, track selection, centrality cuts and PID cuts. This distribution has to be normalized and corrected for acceptance, absorption, multiple scattering, weak–decay (in case of protons) etc.

For a given (y, p_t) bin the fully normalized invariant transverse momentum spectrum is calculated in the following way:

$$\frac{d^3N}{p_t d\phi dy dp_t}(p_T) = \frac{N_i}{p_T \Delta\phi \Delta y \Delta p_T} \cdot \frac{C_{wd} C_{eff}}{N_{ev} ACC\ C_{abs} C_{ms}} \tag{5.17}$$

Where:

N_i : number of particles (deuterons or protons and respective anti–particles)
$\Delta\phi$: bin size in azimuthal angle
Δy : bin size in rapidity
Δpt : bin width in p_T
C_{wd} : weak decay correction factor (for protons)
C_{eff} : detector efficiency correction factor
N_{ev} : number of events
ACC : geometrical acceptance correction factor
C_{abs} : absorption correction factor
C_{ms} : multiple scattering correction factor

Determination of the calculated correction factors is discussed in the next section.

Chapter 6

Results and Discussion

In this section proton and deuteron yields are shown and fitted to an m_T–exponential function. Inverse slope and yields are extracted, and anti–proton-proton along with anti–deuteron-deuteron ratios are compared with results from BRAHMS collaboration.

$B_2(d)$ and $B_2(\bar{d})$ are calculated and plotted versus transverse momentum for MRS = $90°$ ($y = 0$) and MRS = $35°$ ($y \approx 0.9$). A model which could interpret the results better is briefly explained. Then, the average value of B_2 is calculated and compared with results from other experiments.

The transverse size of the source is compared at the two different rapidities ($y = 0$ and $y \approx 0.9$).

Finally a rough estimation of the energy density at kinetic freeze–out is given.

6.1 Yields and Fitting Functions

Figure 6.1 shows (anti–)protons and (anti–)deuterons fitted yields for MRS at 90°. It should be emphasized that in this analysis the calculation of B_2 is not done by fitting the spectra, but by counting the invariant yields in the desired p_T range bin by bin (section 6.3.1). There are mainly two reasons why the yields are fitted. First, it is possible to compare the extracted yields and apparent temperatures with the results of the same data with other members of the collaboration (and therefore check the results). Second, the inverse slopes are used to fit the B_2 versus p_T distribution with an exponential function.

The chosen fit function used is m_T–exponential because it describes the data well at mid–rapidity and forward rapidity. The equation is:

$$f(m_T) = \frac{1}{2\pi m_T}\frac{d^2n}{dy dm_T} = \frac{1}{2\pi}\frac{N}{T(T+m)}e^{-\frac{m_T - m}{T}} \tag{6.1}$$

where the parameters N (rapidity density) and T (inverse slope parameter) are the quantities of interest. The m_T functions can be used to fit in p_T by substituting $m_T = \sqrt{p_T^2 + m^2}$. Se appendix C for more details.

The spectra in figure 6.1 are corrected for all the effects described in the previous chapter. Extrapolated yields and inverse slopes are shown in table 6.1. Good agreement between results from other members of the collaboration [7, 33] can be seen.

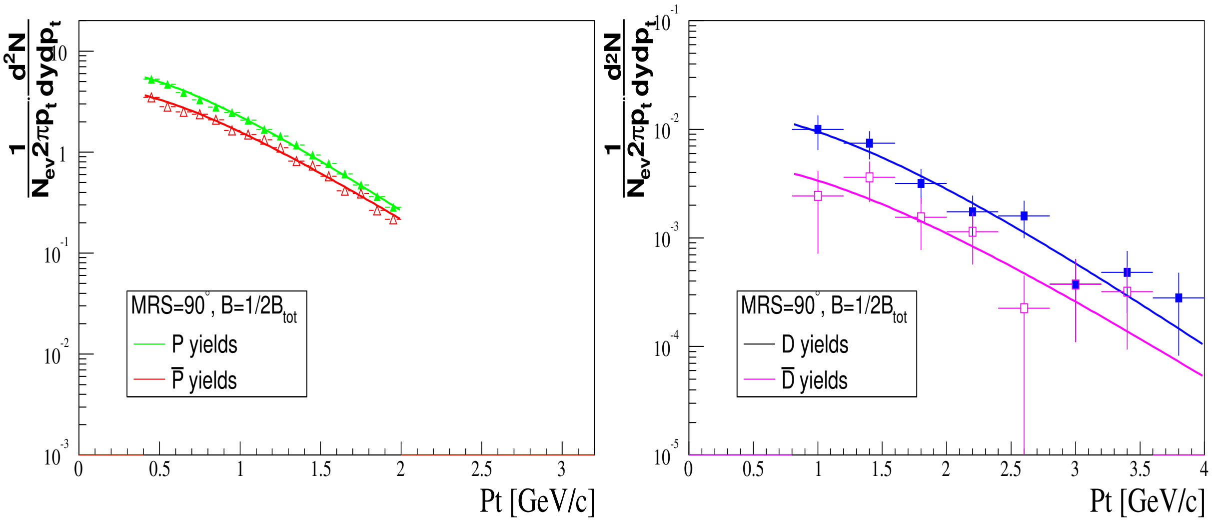

Figure 6.1: Fitted invariant spectra for (anti–)protons and (anti–)deuterons. The rapidity cut is $-0.11 < y < 0.11$ and the momentum of the particles is between 0.4 and 2.1 GeV - therefore only particles in the good PID range are shown.

$FitRange$ $[GeV/c]$	$Part$	dN/dy	$T[MeV]$	$\chi^2/Ndof$	(dN/dy) $InFitRange$	$\%$ of $Extrapol.\ Yields$
$0.4 < p_T < 2.1$	P	22.2 ± 0.22	391 ± 4	32.5/14	17.7	79.9 %
	$\bar{P}$	16 ± 0.18	410 ± 6	34.8/14	12.6	79.4 %
$0.8 < p_T < 4.2$	D	0.11 ± 0.019	506 ± 88	2.94/6	0.08	76.3 %
	$\bar{D}$	0.044 ± 0.011	530 ± 150	3.45/5	0.034	77.8 %

Table 6.1: Extrapolated yields and inverse slope parameters for (anti–)protons and (anti–)deuterons for MRS at 90°. The particles are in the same rapidity cut, i.e. between -0.11 and 0.11.

Figure 6.2 shows the relative ratios at MRS = 90°. The anti–protons to protons ratio show close agreement with the published ones at RHIC at 200 AGeV by BRAHMS collaboration (see [10]).

Figure 6.3 shows protons and deuterons yields at the two MRS angles for matter (left) and anti–matter (right). They show p_T ranges of identified (anti–)protons and (anti–)deuterons.

In figure 6.4 the (anti–)protons and (anti–)deuterons corrected yields are plotted together at the different MRS angles and field settings.

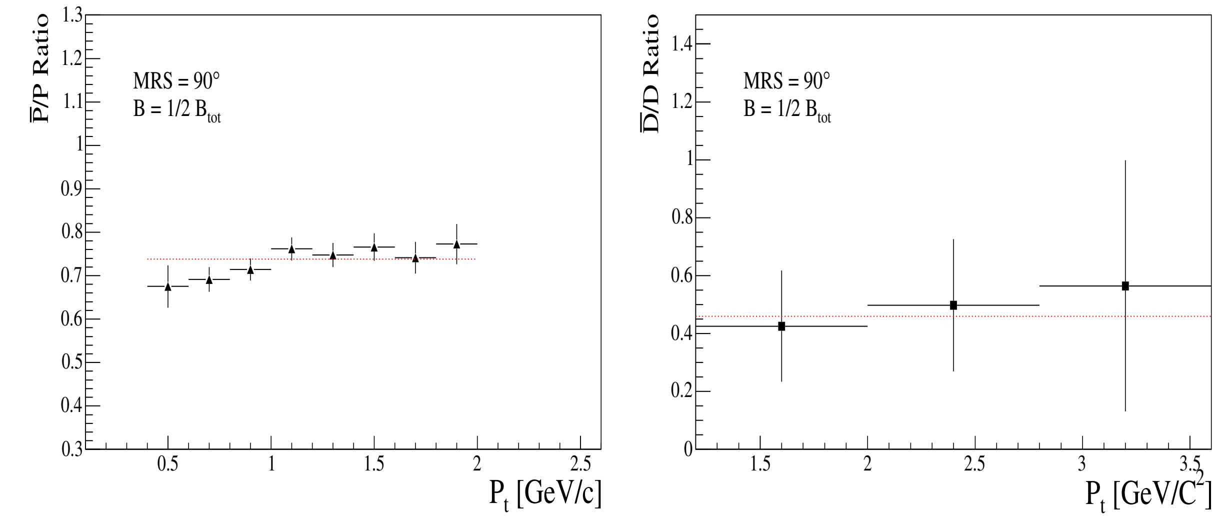

Figure 6.2: Anti–protons to protons (left) and anti–deuterons to deuterons (right) ratios.

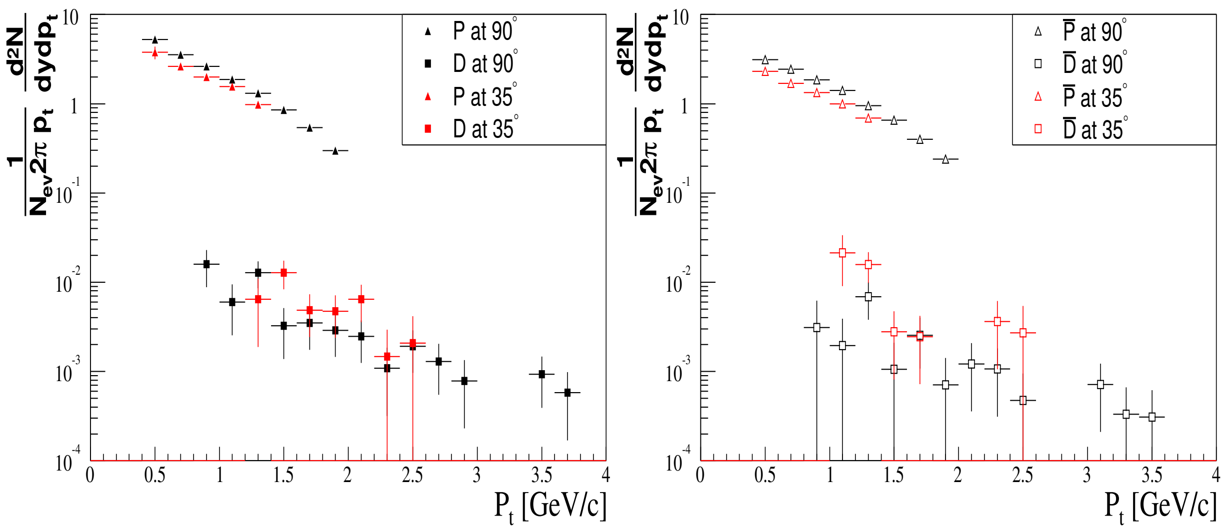

Figure 6.3: Protons and deuterons invariant spectra for matter (left) and anti–matter (right). Protons are selected within a momentum cut between 0.4 and 2.1 GeV, while deuterons are selected between 0.8 and 4.2 GeV (*good* PID selection). The rapidity cut at 90° is between -0.11 and 0.11 and at 35° it is between 0.75 and 0.94.

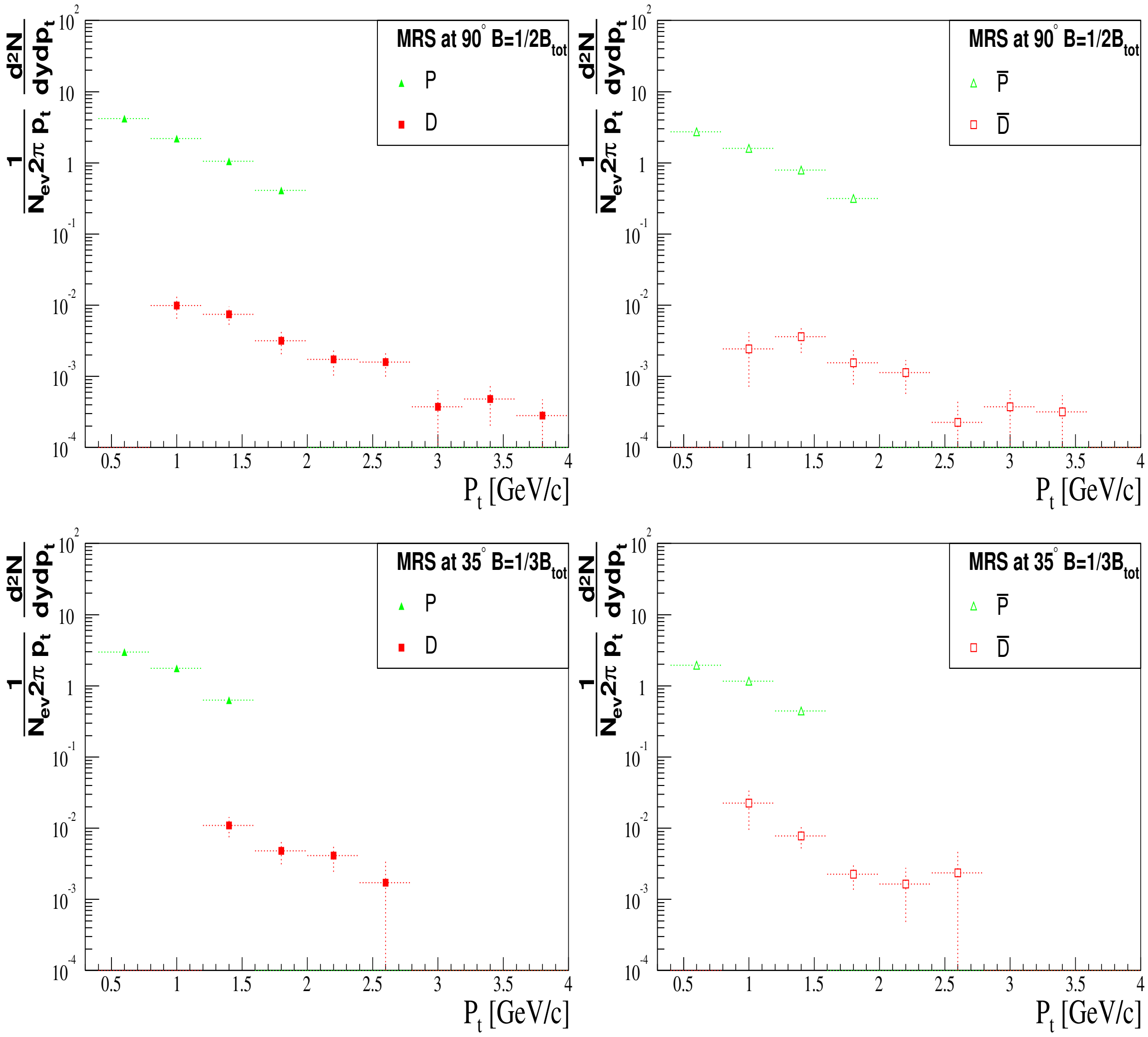

Figure 6.4: Protons and deuterons corrected yields at all used MRS settings for the analysis.

6.2 B_2 versus p_T

Now that the yields are known, B_2 is calculated following equation 2.1:

$$B_2 = \frac{(E_d \frac{d^3 N_d}{dP^3})}{(E_p \frac{d^3 N_p}{dP^3})^2} \tag{6.2}$$

In figure 6.5 (for MRS at 90°) and figure 6.6 (MRS at 35°) the coalescence parameter is plotted as a function of the transverse momentum of the cluster. This is done by dividing the number of the deuterons in a certain p_T range by the square of the number of protons at half transverse momentum. The dashed lines are the average values of B_2 for particles and anti–particles, which are for MRS at 90° $(4.36 \pm 0.99) \cdot 10^{-4}$ and $(3.6 \pm 1.33) \cdot 10^{-4}$ respectively, for MRS at 35° $(8.678 \pm 2.67) \cdot 10^{-4}$ and $(8.98 \pm 5) \cdot 10^{-4}$ respectively.

The B_2 dependence on p_T is also plotted in logarithmic scale to study better the trend.

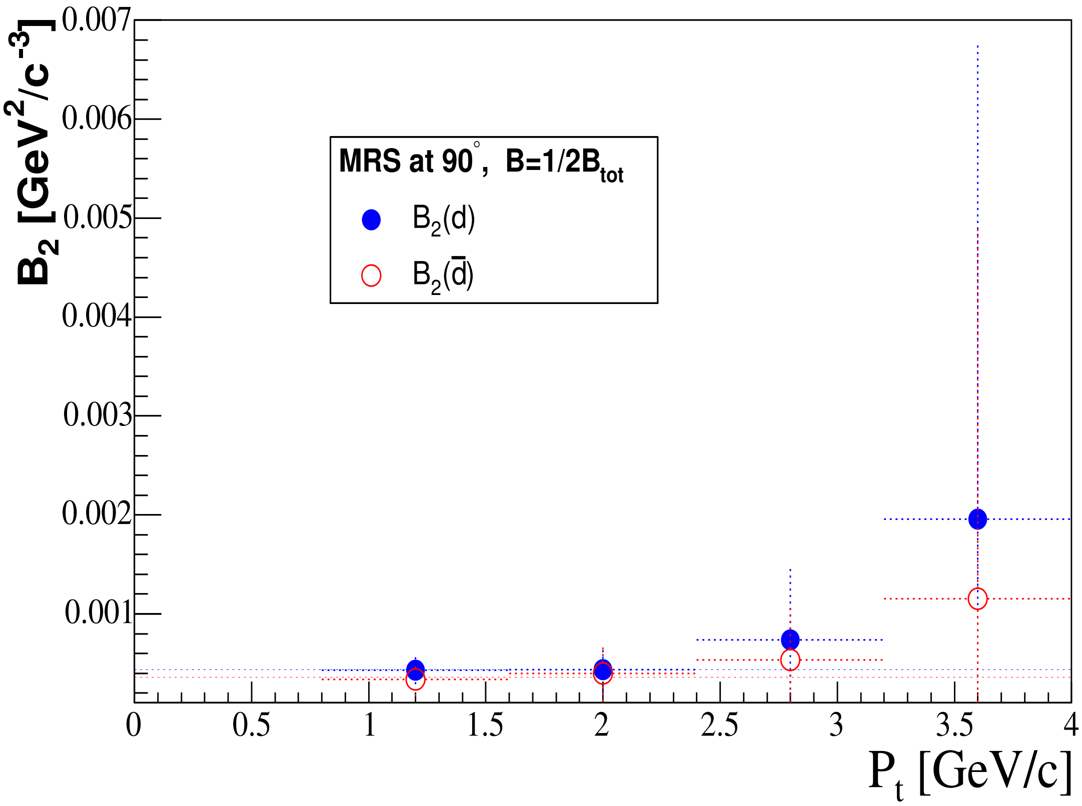

Figure 6.5: Coalescence parameter B_2 as a function of p_T of the (anti–)deuteron for MRS at 90°. Open points are anti–particles. The rapidity cut is ±0.11 and the momentum cut is between 0.4 and 2.1 GeV/c for protons and 0.8 and 4.2 GeV/c for deuterons.

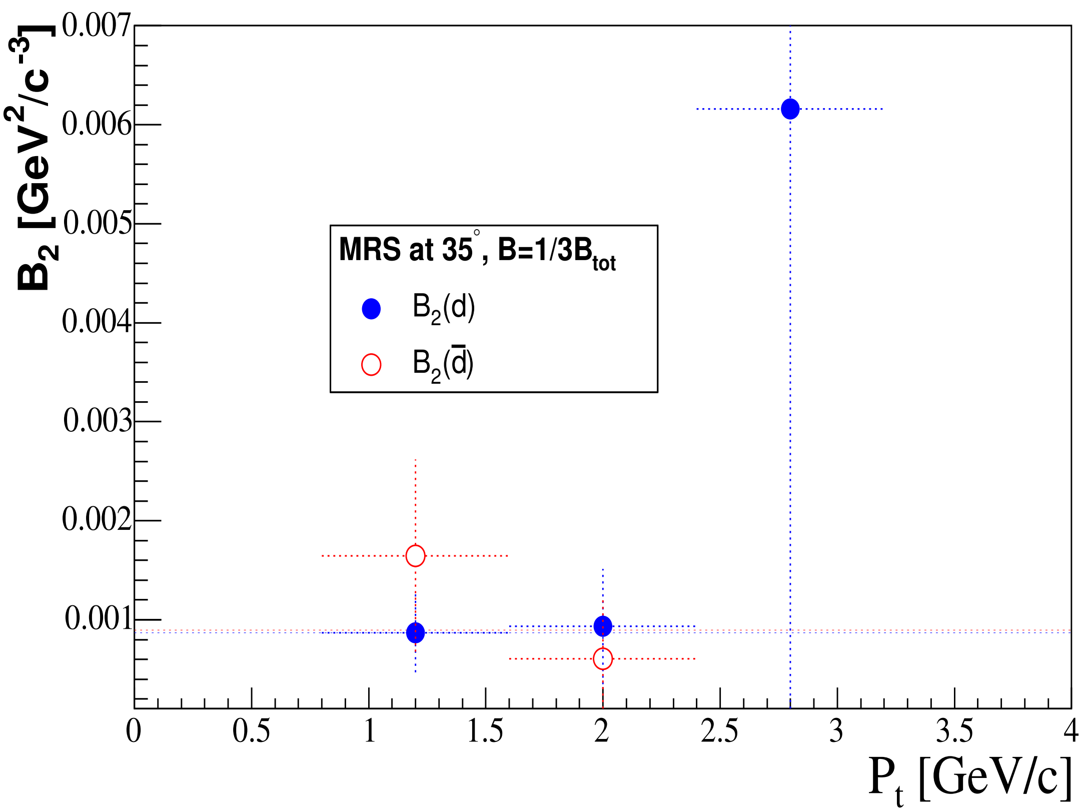

Figure 6.6: Coalescence parameter B_2 as a function of p_T of the (anti–)deuteron for MRS at 35°. Particles are selected in a rapidity range between 0.75 and 0.94. Protons are taken in a momentum range between 0.4 and 2.1 GeV/c, while deuterons between 0.8 and 4.2 GeV/c. The last $B_2(\bar{d})$ is not plotted because it lies higher, meaning it wouldn't be possible to examine the lower points. This can be seen in the logarithmic scale in figure 6.7.

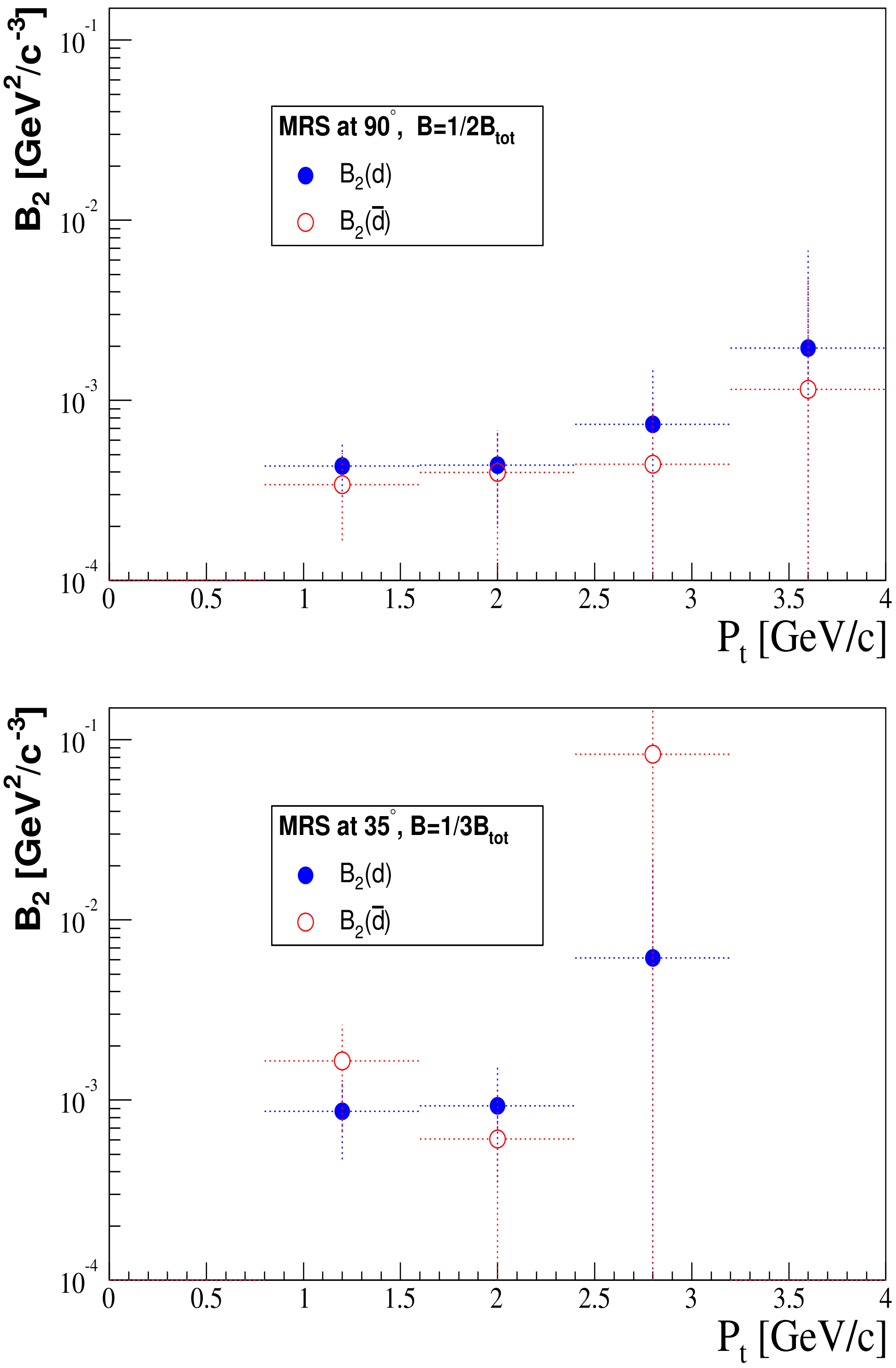

Figure 6.7: Coalescence parameter B_2 as a function of p_T of the (anti–)deuteron for MRS at 90° (top) and 35° (bottom) in logarithmic scale.

The 90° plot seems to show an increase of B_2 with p_T while due to the poor statistics it is more difficult to discuss the 35° plot.

The behavior shown in figure 6.5 can be explained by referring to the increase of the apparent temperature with the particle's mass (see figure 2.3 in chapter 2), which could be related to the presence of a collective flow, as will be explained in the following.

As illustrated in section 6.1 it is a good assumption to approximate the protons and deuterons transverse spectra as exponential. For protons:

$$\frac{d^3N_p}{dp^3} \sim e^{\frac{-E_p}{T_p}} \tag{6.3}$$

and for deuterons:

$$\frac{d^3N_d}{dp^3} \sim e^{\frac{-E_d}{T_d}} \tag{6.4}$$

where T_p and T_d are the inverse slopes for protons and deuterons respectively. Using the above definitions in equation 6.2 and taking in consideration that the momentum of deuterons is almost double that of protons (therefore $E_d \sim 2E_p$), one obtains:

$$B_2 \sim e^{m_T(\frac{1}{T_p} - \frac{1}{T_d})} \tag{6.5}$$

Thus, if T_p and T_d would be the same (no flow) there would be no dependence of B_2 on p_T as predicted by early coalescence models. Such constant behavior can be observed in $p+p$ or light collision systems at low energies. A glance to figure 2.3 shows that for RHIC energies the deuteron apparent temperature is higher than the protons, which leads to an exponential increase of B_2 with p_T.

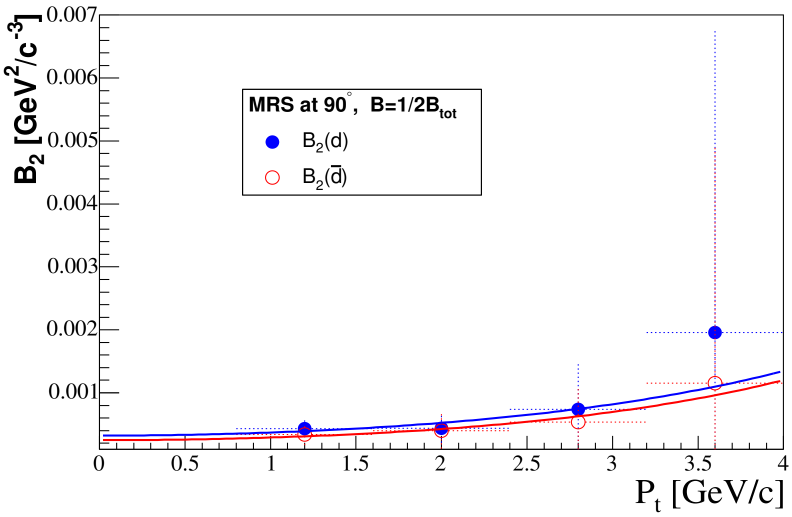

Figure 6.8: $B_2(d)$, $B_2(\bar{d})$ versus p_T fitted at 90° using equation 6.5.

Using equation 6.5 it is possible to fit the B_2 distributions in the transverse momentum. Figure 6.8 shows the result of the fit at mid–rapidity, where there are more statistics.

From the previous considerations one can conclude that flow affects the apparent temperature of the particles, and thus volume (B_2) dynamics. For this reason it is important to include the dynamic of the source (collective flow) in the calculations.

In the model [34] mentioned in chapter 2, A. Polleri develops a method which explains the interplay between flow and density profiles using a dynamical description of the source.

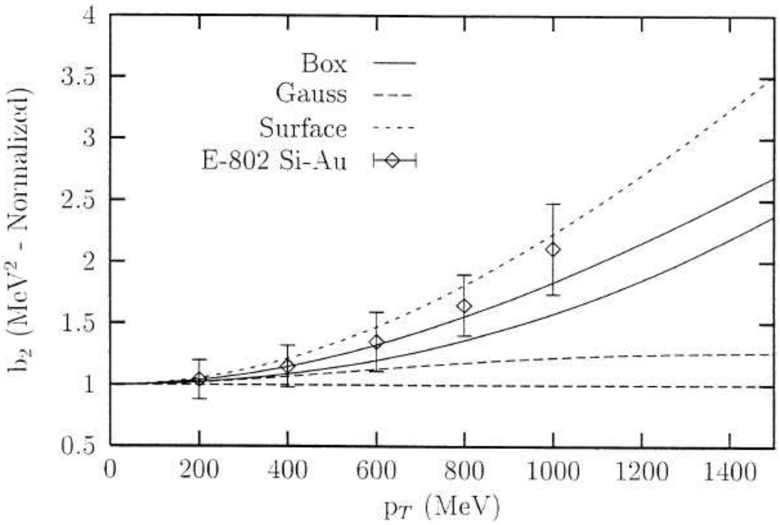

Figure 6.9: B_2 factor as a function of transverse momentum from Polleri simulation. The curve labeled "surface" corresponds to integration over a spherical shell from $R_0/2$ to R_0 in order to simulate surface emission. The two pair of curves correspond to a box like and Gaussian shape of the transverse density profile of the source. The top and low curve for each density profile corresponds to a square root flow profile and a linear profile respectively.

Another interesting feature regarding cluster spectra is that particles with different masses have different spectral slopes (see figures 2.2 and 2.3). For the latest experiments at high energies (like SPS or RHIC) an increasing of B_2 with transverse momentum has been observed. In his work Polleri developed a method to describe B_2 as a function of the transverse momentum of the deuteron (see figure 6.9). Here different curves correspond to different profiles of the source, the same discussed in figure 2.5, i.e. box and Gaussian. The predictions are compared with experimental results of E–802 experiment at AGS. It would be interesting to develop Polleri's program which generated figure 6.9 for RHIC energies, in order to predict how (from f. ex. the results of this work) the densities profiles of the source look.

6.3 The Coalescence Parameter

6.3.1 Calculation of B_2

In the preceding section the coalescence parameter has been calculated by fitting the p_T dependent distribution with a polynomial of order zero. To check the consistency of the result, a more accurate method is used. For a given setting and p_T range, the number of deuterons are counted bin by bin. The same is done for protons at half p_T. Ultimately, the number of deuterons is divided by the square of the number of the protons. The p_T range is taken as wide as possible. The results are shown in table 6.2 and compared with the ones found by fitting the B_2 distribution in p_T with the zero polynomial. The values are found to be consistent within the statistical errors.

The p_T (for deuterons) range in which B_2 can be calculated is shown in figure 6.3.

$[GeV^2/c^{-3}]$	$MRS = 90°$ $B = 1/2B_{tot}$	$MRS = 35°$ $B = 1/3B_{tot}$
$B_2(d)$ (bin by bin)	$(3.1 \pm 0.46) \cdot 10^{-4}$	$(4.84 \pm 1.2) \cdot 10^{-4}$
$B_2(d)$ (p0 Fitted)	$(4.36 \pm 0.99) \cdot 10^{-4}$	$(8.67 \pm 2.67) \cdot 10^{-4}$
$B_2(\bar{d})$ (bin by bin)	$(2.5 \pm 0.57) \cdot 10^{-4}$	$(8.2 \pm 2.88) \cdot 10^{-4}$
$B_2(\bar{d})$ (p0 Fitted)	$(3.6 \pm 1.33) \cdot 10^{-4}$	$(8.98 \pm 5) \cdot 10^{-4}$

Table 6.2: Comparison of $B_2(d)$, $B_2(\bar{d})$ calculations.

6.3.2 Comparison with other Results

Figure 6.10 shows $B_2(d)$ and $B_2(\bar{d})$ values for various collision systems at different energies. The characteristics of the experiments are chosen as close as possible to the ones of this work i.e. same centrality, weak–decay correction, mid–rapidity region, collision between heavy ions ($\sim$ same number of participants). The last two points of the chart show $B_2(d)$, $B_2(\bar{d})$ at rapidity $y \approx 0.9$.

In the other experiments the p_T range in which B_2 is calculated is lower than BRAHMS. This will not affect the general picture significantly, however, because the points with more weight are at low p_T; this is also true for rapidity y $\approx$ 0.9 (see figures 6.5 and 6.6). Still, since the p_T distribution has been fitted at mid–rapidity, it is possible to extrapolate B_2 values at lower p_T. This is done for each experiment in the next section, and the result is that there is not a substantial difference.

A first glance to figure 6.10 shows that B_2 value for $p + p$ is fairly constant with beam energy (see also figure D.1 in appendix D), according to the early coalescence models. One also observes a general decrease of B_2 corresponding to an increase of the energy beam for heavy systems, at least until SPS–RHIC energies. Furthermore, figure D.1 shows that for $N + N$ peripheral collisions B_2 is constant, while for heavier collisions B_2 decrease with an

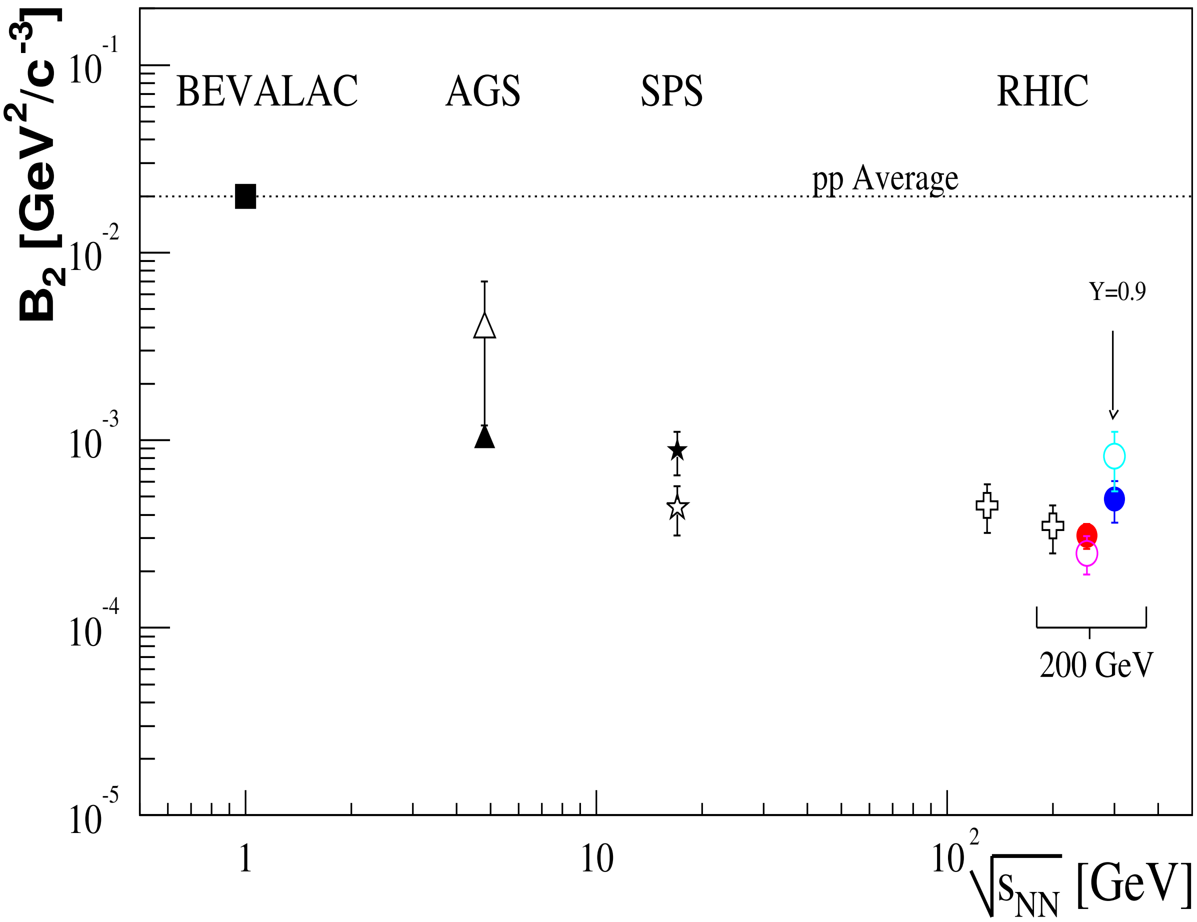

Figure 6.10: Coalescence parameter B_2 as a function of collision energy for Au+Au or Pb+Pb or A+A (Bevelac). Colored points are from this analysis (BRAHMS). (Open)solid symbols show B_2 from (anti–)nuclei. The AGS experiment is E864, the SPS is NA44, the RHIC is STAR and BRAHMS. The experiments characteristics are chosen as close as possible to this one (data taken by BRAHMS at RHIC run II, gold ions collisions at $\sqrt{s_{NN}}$ = 200 GeV) i.e. same centrality (10%, except $STAR$ at 130 GeV which has 18% centrality), collision between heavy nuclei, weak–decay corrected, mid–rapidity region (except the last two points on the right). One difference is that in the other experiments B_2 is calculated from a deuteron p_T range less than one, mainly $0.4 < p_T < 0.8$ GeV/c. NA44 has $0.6 < p_T < 1.6$ GeV/c and STAR has $0.5 < p_T < 0.8$ GeV/c while BRAHMS as previously mentioned (see fig 6.3) is higher (f. ex. $0.8 < p_T < 3.8$ GeV/c for B_2 at 90° - see fig 6.11). Data are taken from [53, 54, 55, 56, 57, 58, 59, 60].

increasing number of participants. From a spherical thermal model the B_2 dependence of number of participants are explained as an increasing volume of the source size $B_2 \sim 1/V$.

The value of the coalescence parameter found at RHIC seems to be quite unexpected since a much lower value of $B_2(d)$ and $B_2(\bar{d})$ was found if using the logarithmic decrease of B_2 until SPS energies. This is not surprising, however, for two reasons. First, the HBT radii do no change much either, and second, if one considers that at AGS energies the collision is baryon dominated, and at SPS it is meson dominated.

Another peculiarity of figure 6.10 is that the values of $B_2(d)$ and $B_2(\bar{d})$ are very close for the different experiments. Since anti–particles are very sensitive to the density of the source due to annihilation, one can argue that deuterons and anti–deuterons are formed on a similar freeze–out hyper–surface.

6.3.3 A more Detailed Comparison of B_2 with other Experiments

As previously mentioned, it is assumed that the coalescence parameters of this analysis are comparable with the ones from the other experiments, even if the last ones are in a lower p_T range. It has been shown that one reason is that the points with more weight are at lower p_T. Furthermore, since the B_2 distribution in function of the transverse momentum at mid–rapidity was fitted to the exponential of equation 6.5 (figure 6.8) it is possible to extrapolate the value of B_2 for a lower p_T.

The transverse momentum range in which $B_2(\bar{d})$, $B_2(d)$ are calculated in E864 is $0 < p_T < 1$ and $0 < p_T < 2$ GeV/c respectively. By extrapolating the values of $B_2(\bar{d})$ and $B_2(d)$ in the same momentum range, the average values are $3.1 \cdot 10^{-4}$ and $3.2 \cdot 10^{-4}$ GeV^2/c^3 respectively.

For NA44 the p_T ranges are $0.6 < p_T < 1.6$ GeV/c which correspond to the BRAHMS $\bar{B}_2 = 2.85 \cdot 10^{-4}$ and $B_2 = 3.95 \cdot 10^{-4}$ GeV^2/c^3 extrapolated in the same p_T range.

These values show a good agreement with the ones calculated in this work by counting bin by bin or by fitting the B_2 distribution in p_T.

6.4 Radius Parameter and Transverse Size at $y = 0$ and $y \approx 0.9$

In this section the transverse size of the system at freeze–out is compared at two different rapidities, $y = 0$ (MRS = 90°), and $y \approx 0.9$ (MRS = 35°).

In order to obtain the best comparison, the B_2 values in the two settings are calculated in the same p_T. This is done using data from figure 6.3 and choosing p_T ranges in which (anti–)deuterons are found in both settings (see figure 6.11). The value of B_2 within these limits is calculated by fitting the respective B_2 versus p_T distributions.

Thus for $B_2(d)$ the p_T range is $0.6 < p_T < 1.3$ GeV/c, $1.2 < p_T < 2.6$ GeV/c for protons and deuterons respectively. For $B_2(\bar{d})$ is $0.5 < p_T < 1.3$ GeV/c, $1.0 < p_T < 2.6$ GeV/c for anti–protons and anti–deuterons respectively.

In a fireball model with chemical and thermal equilibrium (see section 2.4 and [27, 61]),

$$B_2 = \frac{3}{4} R_{np} \frac{(hc)^3}{V} \frac{m_d}{m_p^2}, \tag{6.6}$$

where 3/4 is the spin contribution, R_{np} is the ratio of neutron to protons in the colliding system (which can be assumed to be 1 for $y = 0$ and $y \approx 0.9$ [62]) and V is the volume of the fireball when the particles coalesce.

The radius of the system can be written as:

$$R^3 = \alpha R_{np} (\hbar c)^3 \frac{m_d}{m_p^2} (B_2)^{-1} \tag{6.7}$$

where α depends on the assumed source geometry, e.g. $\alpha = 9/2\pi^2$ for a hard sphere ($V = R^3 \frac{4}{3}\pi$) and $\alpha = 3/4\pi^{3/2}$ for a Gaussian source. Here a hard sphere is assumed.

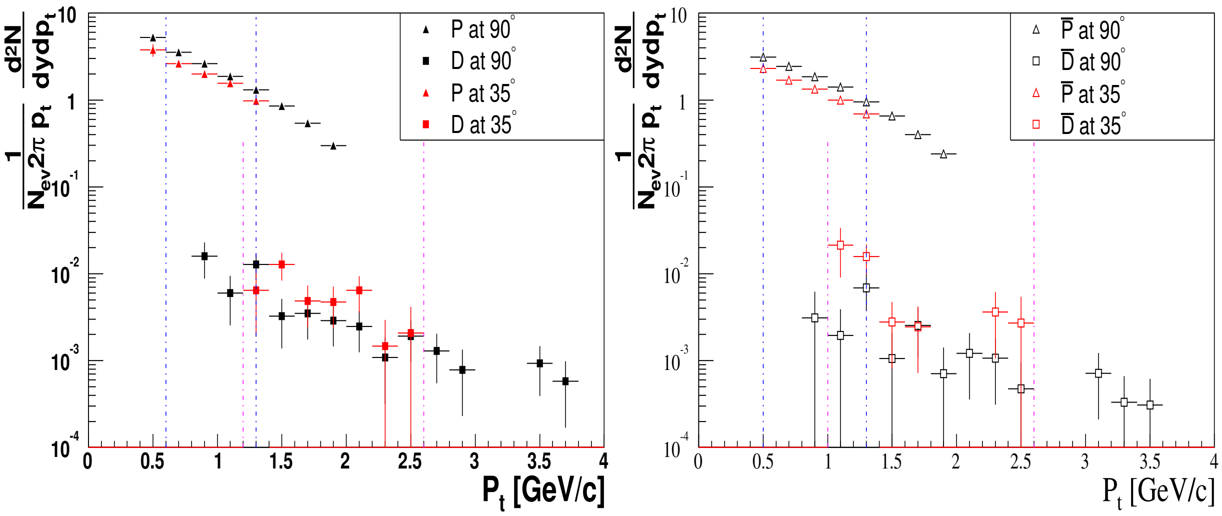

Figure 6.11: Protons and deuterons invariant spectra for matter (left) and anti–matter (right). Protons are selected within a momentum cut between 0.4 and 2.1 GeV/c, while deuterons between 0.8 and 2.2 GeV/c. The rapidity cut at 90° is between -0.11 and 0.11 and at 35° is between 0.75 and 0.85. The blue lines indicate the protons p_T range (at 90° and 30°) used to calculate B_2. The pink lines define the p_T range for deuterons, which is double that of protons. In this way it is possible to compare B_2 for both settings.

The results for B_2 and relative transverse radii are shown in table 6.3.

The table shows an increase of $B_2(d)$, $B_2(\bar{d})$ with rapidity corresponding to a decrease of the radius. Because the model assumes a spherical fireball volume in a local rapidity frame from transverse measurements, the radius parameter is related to the transverse size of the source. The decrease of the radius with rapidity can therefore indicate that the

	$MRS = 90°$ $B = 1/2B_{tot}$	$MRS = 35°$ $B = 1/3B_{tot}$
$B_2(d)$ $[GeV^2/c^3]$	$(5.36 \pm 1.4) \cdot 10^{-4}$	$(8.67 \pm 2.67) \cdot 10^{-4}$
$SourceRadius$ $[fm]$	11.07 ± 0.96	9.43 ± 0.96
$B_2(\bar{d})$ $[GeV^2/c^3]$	$(3.57 \pm 1.34) \cdot 10^{-4}$	$(9.04 \pm 5.09) \cdot 10^{-4}$
$SourceRadius$ $[fm]$	12.6 ± 1.58	9.30 ± 1.74

Table 6.3: Comparison between $B_2(d)$, $B_2(\bar{d})$ values and respective source radius at 90° and 35°. The comparison is made at the same p_T (see figure 6.11) where (anti–)deuterons are available for both settings.

transverse size of the source decreases with rapidity. However the decrease is within the statistical uncertainties. This reflects the picture of a cylindrical source with the same characteristics between rapidity zero and one, as confirmed by other measurements.

Figure 6.12 shows the fitted values of the coalescence factor $B_2(d)$ at 90° and radius parameter R as a function of the deuteron transverse mass.

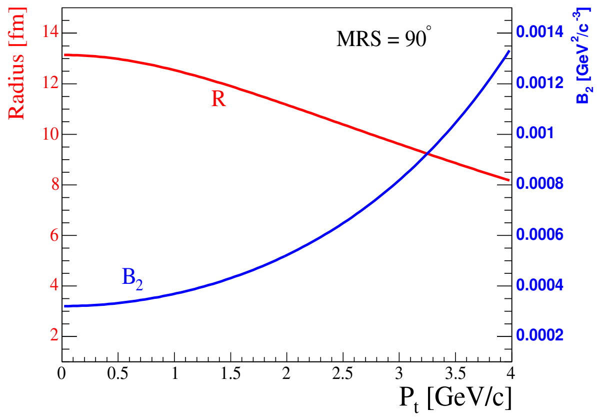

Figure 6.12: Coalescence factor $B_2(d)$ and radius parameter R as a function of the deuteron transverse momentum for positive particles for MRS = 90°. The blue line is the exponential fit shown in figure 6.5. The radius is calculated using equation 6.7 and assumes spherical source. Statistical errors are not drawn to help clarify the trend.

6.5 An Estimation of the Energy Density at Freeze–out

In this section a rough estimate of the energy density of the source at the calculated freeze–out volume is given. In reminiscence to the Bjorken formula [63] the energy density at freeze–out might be estimated as follows:

$$\frac{E_f(V_f)}{V_f} = \Delta y \frac{dE_t}{dy} \frac{3}{2} \frac{1}{nV_B} \tag{6.8}$$

where $\frac{dE_t}{dy}$ is the transverse energy per unit rapidity. Since the true isotropic energy density is 3–dimensional, and the quantity $\frac{dE_t}{dy}$ is 2–dimensional, the contribution from the third dimension is by a factor of 3/2. V_B is the coalescence volume found by equation 6.6. One estimates this volume to be about half of all fireball volume (the one which one wants to calculate) assuming two particles from opposite hemispheres do not coalesce. Therefore the factor n is applied to account for the transverse expansion of the system in the two opposite directions. A reasonable value for this factor is between one and two.

The use of the factor Δy can be explained as follows. Since one has assumed that there is thermalization for a certain range in rapidity, Δy is the source length in rapidity over which particles (nucleons) are correlated at freeze–out. For a thermal distribution of nucleons one finds $\Delta y \approx 1$ [64].

$\frac{dE_t}{dy}$ is calculated from [65]. The value is ~ 700 GeV and agrees with BRAHMS results.

Finally the volume V_B is calculated from equation 6.6 using B_2 at mid–rapidity. The value is $V_B = 9806\ fm^3$. Therefore:

$$\epsilon_{coal} = \frac{E_f(V_f)}{V_f} \approx \quad 0.075 \pm 0.025 \quad GeV/fm^3 \tag{6.9}$$

The error is calculated assuming $n = 1.5 \pm 0.5$.

The value calculated in equation 6.9 is the maximum possible for the energy density. This is because the energy density needs to be calculated only from the thermal energy, while the measured dE_t is the sum of a thermal and a kinetic term (due to flow). Therefore the kinetic term flow contribution has to be analyzed and corrected. The relative freeze–out temperature (T_{fo}) of the energy density given in 6.9 is now calculated by assuming a flow contribution to the energy density of $\sim 30\%$ [66].

In [67] hydrodynamic simulations of heavy ion–collisions at full RHIC energy have been made, based on a resonance gas equation of state which explicitly incorporates hadro–chemical freeze–out by employing chemical potentials for (stable) mesons and baryons in the later hadronic stages. Here for an energy density at freeze–out $\epsilon_{fo} = 0.1\ GeV/fm^3$ a freeze–out temperature $T_{fo} = 100$ MeV is found. From the same paper it turns out that because of chemical potential conservation the relation $\epsilon \sim T^4$ for an ideal gas is true. Therefore

$$T_{coal} = T_{fo}(\frac{\epsilon_{coal}}{\epsilon_{fo}})^{1/4} \sim 85\ MeV \tag{6.10}$$

where $\epsilon_{coal} \approx 0.05\ GeV/fm^3$ after flow correction.

From the result from this rough estimate one can argue that the coalescence temperature is lower than the freeze–out temperature, meaning coalescence is a softer process than standard processes occurring at 100 MeV. Therefore coalescence processes end little later.

Chapter 7

Summary and Conclusion

In this work data from Au+Au collisions at $\sqrt{s_{NN}} = 200$ GeV at RHIC have been analyzed. The data comes from mid–rapidity region (MRS = 90°, B = 1/2B$_{tot}$) and from y ≈ 0.9 (MRS = 35°, B = 1/3B$_{tot}$).

Invariant yields of (anti–)protons and (anti–)deuterons are found for the 0% to 10% most central events. Geometrical acceptance corrections, detector efficiency and corrections due to secondary interactions have been applied. Part of the corrections (weak decay and particle knock–out) are made using HIJING event generator. $6 \cdot 10^5$ events at RHIC energy are simulated and sent through BRAHMS spectrometers using BRAG detector simulator. At the angles and magnetic fields used in MRS, (anti–)protons knock–out from the beam pipe is negligible. It has been observed that most of the knock–out protons from beam pipe are originated by pions. A weak decay p_T–dependent correction factor is calculated for protons. The correction factor is corrected for the measured ratio Λ/p. Furthermore deuterons and protons are corrected for absorption and production.

Due to PID limitations, (anti–)protons and (anti–)deuterons used in the analysis are in the momentum range $0.4 < p < 2.1$ GeV/c and $0.8 < p < 4.2$ GeV/c respectively.

First, the coalescence parameter is calculated as a function of transverse momentum. At mid–rapidity it seems that B_2 increases with increasing transverse momentum. This behavior has also been observed at AGS [24] and SPS [68] energies. Due to the poor statistics it is difficult to say whether this increase is also found at 35°.

The p_T dependence is related to the inverse slope of the particle spectra and could be understood as a result of collective flow. It is therefore important to develop a coalescence model which includes the dynamic of the source. *Polleri et al.* [34] have shown that this dependence is related to the density profile and flow profile of the source at freeze–out.

The coalescence factors B_2 are calculated in the (anti–)deuteron transverse momentum, by dividing the number of deuterons in a certain p_T range by the square of the number of deuterons in the half p_T range. At MRS = 90° it has been found $B_2(d) = (3.1 \pm 0.46) \cdot 10^{-4}$ GeV^2/c^3 calculated in the range $0.8 < p_T < 3.8$ GeV/c, $B_2(\bar{d}) = (2.5 \pm 0.57) \cdot 10^{-4}$ GeV^2/c^3 calculated in the range $0.8 < p_T < 3.6$ GeV/c and at MRS = 35° $B_2(d) = (4.84 \pm 1.2) \cdot 10^{-4}$ GeV^2/c^3 in the range $1.2 < p_T < 2.6$ GeV/c, $B_2(\bar{d}) = (8.2 \pm 2.88) \cdot 10^{-4}$ GeV^2/c^3 in the range $1 < p_T < 2.6$ GeV/c which are the first measurements ever at 200 AGeV for this setting.

The results are compared with other experiments at similar conditions (weak–decay corrected, centrality, etc.) for different beam energies.

Figure 6.10 shows that for heavy systems there is a relation between freeze–out volume and beam energy. As volume increases, so does the beam energy. Furthermore figure D.1 shows an increase of the volume also increases the number of participants.

One finds that the RHIC volume for anti–matter is almost 2 times bigger than SPS volume, while SPS volume is 8 times bigger then AGS. This is quite unexpected if one follows the exponential decrease of B_2 until SPS energies, but not so surprising from HBT results and the physics of the collision.

A rough estimation of the energy density at freeze–out seems to indicate that deuterons should have been formed somewhat after chemical freeze–out, around which deuterons are still subject of dissociation.

Another noteworthy feature observed is that the values of $B_2(d)$ and $B_2(\bar{d})$ are very close. Since anti–particles are very sensitive to the density of the source due to annihilation, one can argue that deuterons and anti–deuterons are formed on a similar freeze–out hyper–surface and therefore have one source.

The calculated transverse size of the source at cluster formation at y = 0 and y ≈ 0.9 are similar, supporting the view that is now clearly emerging of a central rapidity plateau with boost invariant properties.

Appendix A

The BRAHMS Collaboration

I. G. Bearden[7], D. Beavis[1], C. Besliu[10], Y. Blyakhman[6], B. Budick[6], H. Bøggild[7], C. Chasman[1], C. H. Christensen[7], P. Christiansen[7], J. Cibor[3], R. Debbe[1], E. Enger[12], J. J. Gaardhøje[7], M. Germinario[7], K. Hagel[8], O. Hansen[7], A. Holm[7], A. K. Holme[12], H. Ito[11], E. Jakobsen[7], A. Jipa[10], F. Jundt[2], J. I. Jørdre[9], C. E. Jørgensen[7], R. Karabowicz[4], T. Keutgen[8], E. J. Kim[1], T. Kozik[4], T. M. Larsen[12], J. H. Lee[1], Y. K. Lee[5], G. Løvhøiden[12], Z. Majka[4], A. Makeev[8], B. McBreen[1], M. Mikelsen[12], M. Murray[8], J. Natowitz[8], B. S. Nielsen[7], J. Norris[11], K. Olchanski[1], J. Olness[1], D. Ouerdane[7], R. Płaneta[4], F. Rami[2], C. Ristea[10], D. Röhrich[9], B. H. Samset[12], D. Sandberg[7], S. J. Sanders[11], R. A. Scheetz[1], P. Staszel[7], T. S. Tveter[12], F. Videbæk[1], R. Wada[8], A. Wieloch[4], Z. Yin[9], I. S. Zgura[10]

[1] Brookhaven National Laboratory, Upton, New York 11973, USA
[2] Institut de Recherches Subatomiques and Université Louis Pasteur, Strasbourg, France
[3] Institute of Nuclear Physics, Krakow, Poland
[4] Smoluchkowski Inst. of Physics, Jagiellonian University, Krakow, Poland
[5] Johns Hopkins University, Baltimore 21218, USA
[6] New York University, New York 10003, USA
[7] Niels Bohr Institute, Blegdamsvej 17, University of Copenhagen, Copenhagen 2100, Denmark
[8] Texas A&M University, College Station, Texas, 17843, USA
[9] University of Bergen, Department of Physics, Bergen, Norway
[10] University of Bucharest, Romania
[11] University of Kansas, Lawerence, Kansas 66049, USA
[12] University of Oslo, Department of Physics, Oslo, Norway

Appendix B

Kinematic Variables

In heavy–ion high–energy collisions, the measurable part of an event are the product variables at the time of detection. It therefore helps to define kinematics variables to describe the collision process.

The speed of particles is often comparable to the speed of light, so all kinematics calculations should be performed relativistically. The speed of light is set to one.

The measurable effects of relativity are based on **gamma** (γ) which depends only on the speed of a particle. By definition:

$$\gamma = \frac{1}{\sqrt{1-(\frac{v}{c})^2}} \tag{B.1}$$

γ is responsible for the phenomenon of *length contraction* and *time contraction*.

Consider two observers moving relative to each other at a speed close to the speed of light. Each of them will observe in the other a length contraction by the same factor γ, and time dilation by the same factor γ.

The conservation of momentum and energy law including γ will be:

For Newtonian momentum:

$$p = mv \tag{B.2}$$

For relativistic momentum:

$$p = \gamma mv \tag{B.3}$$

Where m is the mass, v is the speed, γ is the relativistic factor.

The ***transverse momentum p_T*** of a particle is defined as:

$$p_T = \sqrt{p_x^2 + p_y^2} = p\ sin\theta \tag{B.4}$$

Where p_x and p_y are the components of p in the x and y direction, and therefore parallel to the x axis and the y axis respectively.

In a relativistic nucleus–nucleus collision scenario (see 1.3.1) the transverse momenta which are mainly due to the spectator nucleons are concentrated at the projectile rapidities (see B.6), while particles originating from the participant region are observed in a wider region of rapidity.

The non relativistic ***transverse velocity v_t*** is defined as

$$v_t = \frac{p_T}{m} \tag{B.5}$$

The longitudinal variable, the ***rapidity y***, is defined as:

$$y = \frac{1}{2}\, ln\Big(\frac{E + p_z}{E - p_z}\Big) = \frac{1}{2}\, ln\Big(\frac{1 + \beta cos\theta}{1 - \beta cos\theta}\Big) \tag{B.6}$$

Where E is the energy of the particle defined as $E^2 = p^2 + m^2$, p_z is the momentum parallel to beam axis, $\beta \simeq c$ (the definition of β is $\beta = v/c$) and θ is the scattering angle between the beam axis and p.

In a very simplified way one can say that y is a measure of the velocity of the particle and equation B.6 can be written (assuming $c = 1$) as

$$y = \frac{1}{2}\, \ln \frac{1 + v_z}{1 - v_z} = \tanh^{-1}(v_z) \tag{B.7}$$

where v_z is the velocity along the beam direction given by $v_z = p_z \,/\, E$.
In the non–relativistic limit ($v_z \ll 1$) the rapidity will approach the parallel velocity ($y \rightarrow v_z$).

Rapidity y is a *relativistic invariant* quantity. This means that rapidities are additive, like velocities in Galilean transformations.

Equation B.6 can be used for any frame moving in the beam direction. Such frames are f. ex. the laboratory frame or the center of mass frame.
The rapidity of a particle as seen from the laboratory frame is related to the rapidity as

$$y_A^{lab} = y_A^{cm} + y_0 \tag{B.8}$$

In the colliders the target and the projectile move with the same speed in opposite directions so that the cm is at rest in the laboratory frame. In this way all the energy provided by the accelerator system is available for excitation of the colliding nuclei. For a collision between two nuclei of equal size, the relation between the γ values of the beam particles is

$$\gamma_{cm} = \sqrt{\frac{\gamma_{lab} + 1}{2}} \tag{B.9}$$

where $\gamma_{lab} = E_b \,/\, m_N\, c^2$ where m_N is the nucleon mass. γ_{cm} is usually much smaller than γ_{lab}, this makes it advantageous to construct colliders.

For a symmetric collision in a fixed target experiment at relativistic energies, the ***center of mass energy per nucleon–nucleon pair $\sqrt{s_{NN}}$*** is

$$\sqrt{s_{NN}} = \frac{E_b}{\gamma_{cm}} = \frac{E_b}{\sqrt{\frac{1}{2}(\gamma_{lab} + 1)}} \tag{B.10}$$

where E_b is the beam energy. For colliding beams in colliders like RHIC, $\sqrt{s_{NN}}$ is the sum of the two beam energies. For example two 100AGev colliding beams give $\sqrt{s_{NN}} =$ 200 GeV, while a 200 AGev beam on a fixed target gives only $\sqrt{s_{NN}} = 19.4$ GeV.

Another frequently used variable is the ***relativistic transverse mass*** $\boldsymbol{m_T}$

$$m_T = \sqrt{m^2 + p_T^2} \tag{B.11}$$

which is connected with the energy via

$$E = m_T \cosh y \tag{B.12}$$

When it is not possible to measure the particle masses, the data is often given in terms of ***pseudo–rapidity*** $\boldsymbol{\eta}$

$$\eta = \frac{1}{2}\, ln\Big(\frac{p + p_z}{p - p_z}\Big) = -ln\Big(tan\frac{\theta}{2}\Big) \tag{B.13}$$

pseudo–rapidity therefore gives information on how much the particle deviates from z direction, as it is only a function of the scattering angle θ in the laboratory system.

Thus, the relationship between pseudo–rapidity and momentum will be

$$p_z = p_T \sinh \eta \qquad p = p_T \cosh \eta \tag{B.14}$$

The energy is related to pseudo–rapidity and rapidity through

$$E \tanh y = p \tanh \eta \tag{B.15}$$

With $E^2 = p^2c^2 + m^2c^4$. Equation B.15 indicates that for large momenta (high energies) p or vanishing mass m the pseudo–rapidity and the rapidity will converge or alternatively $\eta \to y$ as $p_T \to m_T$. Pseudo–rapidity is then a good approximation to rapidity for light particles and/or particles with high p_T.

Appendix C

Fit Functions

Assuming a thermal source with N particles, the number of particles in the small momentum interval can be written as

$$\frac{d^3n}{dp^3} = \frac{d^3n}{Ep_T dp_T dy d\phi} \tag{C.1}$$

where in the Lorentz frame is convenient to use the kinetic variables transverse momentum p_T, rapidity y and the angle ϕ since the perpendicular variables p_T and ϕ are boost invariant and y is boost additive.

Assuming no explicit dependence on the azimuthal angle ϕ, equation C.1 can be integrated over 2π.

$$E\frac{d^3n}{dp^3} = \frac{d^2n}{2\pi p_T dp_T dy} \tag{C.2}$$

Now the goal is to derive a function which can be used to fit the data. This is done by starting from the partition function in statistical mechanics, assuming a GCE (Grand Canonical Ensemble) and exchange of heat and particles. From that the thermodynamical relationships between pressure, entropy, and particle number per collision, can be calculated. Starting from the conditions of a box filled with noninteracting bosons and fermions it is possible to derive an expression for the differential multiplicity. If one consider collisions at $s_{NN} = \sqrt{200}$ GeV center of mass energies it is possible to write

$$E\frac{d^3n}{dp^3} \sim Ee^{-E/T}, \tag{C.3}$$

where E is the energy of the particle.

Here the fit functions are exponential in p_t and m_t, assuming the fireball is in local thermal equilibrium and considering that in high–energy hadron physics the p_t distribution decreases nearly exponentially. From the previous equation is possible to write the approximation

$$E\frac{d^3n}{dp^3} = Ae^{-p_T/T} \tag{C.4}$$

A relationship between the theoretical model and an exponential fit function in p_t has been established. The fit parameter A is the intersection with the y axis and T is the slope. One now wants to find an expression for A related to the yield. This is done by calculating the absolute yield, the number of particles inside this rapidity region:

$$I_p = \frac{dn}{dy} = \int_0^\infty \frac{d^2n}{dydp_t}dp_t \tag{C.5}$$

Looking at equations C.2 and C.4 it follows

$$\int_0^\infty \frac{d^2n}{dydp_t} = \int_0^\infty 2\pi p_T Ae^{-p_T/T} = 2\pi T^2 A \tag{C.6}$$

Thus

$$A = \frac{N}{2\pi T^2} \tag{C.7}$$

And

$$\frac{d^3n}{dp^3} = \frac{d^2n}{2\pi p_T dp_T dy} = \frac{N}{2\pi T^2}e^{-p_T/T} \tag{C.8}$$

The idea is the same for the m_t exponential:

$$f(m_T) = Ae^{-\frac{m_T}{T}} \tag{C.9}$$

The idea is to use instead the constant A the yield $N = dn/dy$. After integrating the expression of the m_t exponential will be:

$$f(m_T) = \frac{1}{2\pi m_T}\frac{d^2n}{dydm_T} = \frac{1}{2\pi}\frac{N}{T(T+m)}e^{-\frac{m_T-m}{T}} \tag{C.10}$$

The m_T functions can be used to fit in p_T by substituting $m_T = \sqrt{p_T^2 + m^2}$. The last term of equation C.10 is the exponential function to which the corrected spectra from the data are fitted.

Appendix D

B_2 Chart for Different Collision Systems

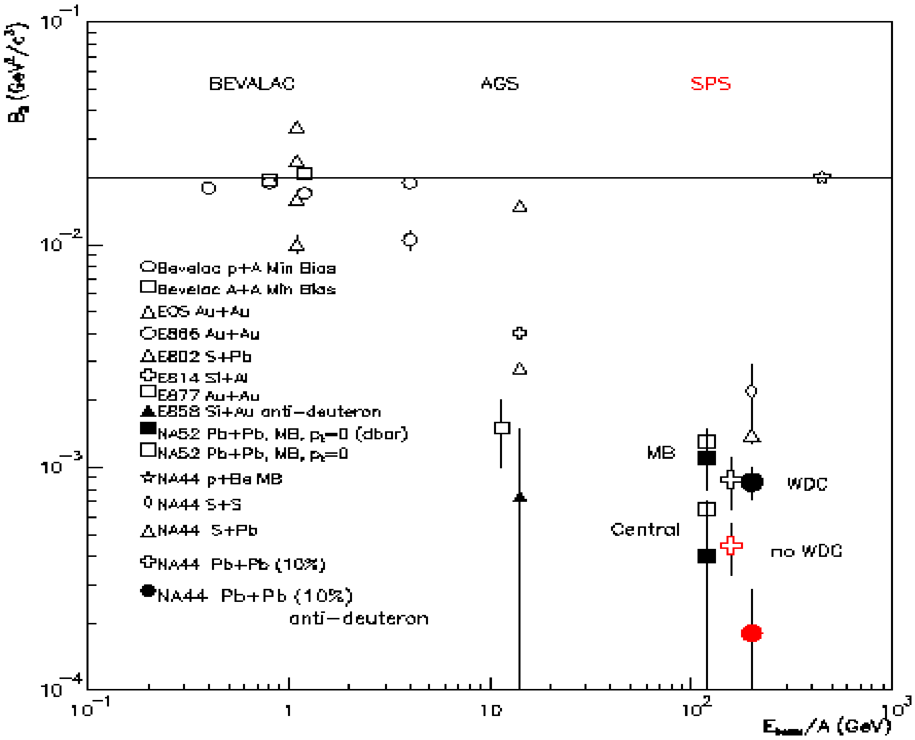

Figure D.1: Comparison of B_2 values for various collision systems [24]. For clarity the SPS Pb+Pb points are shifted slightly in energy.

Appendix E

Data

In the following all runs used for the presented analysis are enumerated.

MRS at 90° : 5895, 5896, 5903, 5904, 5908, 5910, 5914, 5915, 5916, 5924, 5925, 5937, 5938, 5939, 5945, 5946, 5947, 5948, 5952, 5953, 5954, 5956, 5957, 5958.

MRS at 35° : 5388, 5398, 5399, 5407, 5408, 5420, 5432, 5435, 5438, 5468, 5471, 5473, 5474, 5475, 5479.

Appendix F

Acronyms

ADC Analog-to-Digital Converter. Device which converts the information contained in an analog signal to an equivalent digital form.

AGS Alternating Gradient Synchrotron.

ATR AGS To RHIC line.

BBC Beam Beam Counters.

BFS Back Forward Spectrometer.

BNL Brookhaven National Laboratory, located in Long Island, USA.

BRAG Brahms Analysis GEANT.

BRAHMS Broad RAnge Hadron Magnetic Spectrometers.

BRAT BRahms Reconstruction and Analysis toolkit. Analysis framework based on the *ROOT* system. *BRAT* consist of a set of shared libraries, most of which are specific to *BRAHMS* data analysis.

CERN European Organization for Nuclear Research.

DAQ Data Acquisition System. Builds the so called events which in principle are the data read out from the different detector systems.

DC Drift Chamber.

DST Data Summary Tapes. Trees containing all the information for physics analysis.

FFS Front Forward Spectrometer (See figure 3.2).

FS Forward Spectrometer.

GBRAHMS Geant for Brahms, now *BRAG*.

GEANT GEometry ANd Tracking.

HEHI High Energy Heavy Ion group, located at *NBI*, Denmark.

HIJING Heavy Ion Jet INteraction Generator.

HITL Heavy Ion Transfer Line.

HPSS High Performance Storage System. *HPSS* is a hierarchical storage system designed to deal with the massive amounts of data produced by computing systems, and to deal with imbalance of computational vs. I/O capabilities.

MA Multiplicity Array.

MIP Minimum Ionizing Particle.

MRS Mid–Rapidity Spectrometer (See figure 3.2).

NA49 Large TPC experiment at CERN.

NBI Niels Bohr Institute, university of Copenhagen, DK.

PID Particle IDentification.

PMT Photo Multiplier Tubes.

QCD Quantum Chromo Dynamics.

QGP Quark Gluon Plasma.

Rdo Reduced data objects, essentially calibrated *digits*.

RHIC Relativistic Heavy Ion Collider, located at *BNL*, USA.

RICH Ring Imaging ČHerenkov detector.

ROOT Root's Object Oriented Technologies.

SiMA Silicon Multiplicity Array.

SMA Silicon Metal Array.

TMA Tile Multiplicity Array.

TOFW Time Of Flight Wall in MRS.

TPC Time Projection Chamber.

TPM1 Front TPC in the MRS.

TPM2 Back TPC in the MRS.

UrQMD Ultra–relativistic Quantum Molecular Dynamics Model.

VENUS Very Energetic NUclear Scattering.

ZDC Zero Degree Calorimeters.

Bibliography

[1] CLAS Collaboration, arXiv:hep–ex/0307018 (2003).

[2] S. Bethke, *Nucl. Phys. Proc. Suppl.* **121**, 74 (2003)

[3] T.R. Klassen, *Phys. Rev.* **D 51**, 5130 (1995).

[4] John W. Harris, Yale relativistic Heavy Ion Group, World scientific, YRHI-98-13 (1998).

[5] Z. Fodor, S.D. Katz, JHEP 0203, 014 (2002).

[6] P. Braun–Munzinger, D. Magestro, K.redlich and J. Stachel, Phys. Lett. **B 518**, 41 (2001).

[7] Peter H.L. Christiansen PhD Thesis, Niels Bohr Institute, Copenhagen (2003).

[8] F. Videbæk, O. Hansen, *Phys. Rev.* **C 52**, 2684 (1995).

[9] STAR collaboration, C. Adler et al., *Phys. Rev. Lett.* **86**, 4778–4782 (2001).

[10] BRAHMS Collaboration, I. G. Bearden, *Phys. Rev. Lett.* **90**, 102301 (2003).

[11] BRAHMS Collaboration, I. Arsene et al., *Phys. Rev. Lett.* **91**, 072305 (2003).

[12] J. Harris, *Relativistic Heavy ion Physiscs and the Relativistic Heavy Ion Collider*. Prepared for Lake Louise Winter Institute: Quantum Chromo Dynamics, Lake Louise, Alberta, Canada, 15-21 Feb (1998).

[13] J. Rafelski, J. Letessier and A. Tounsi, *Acta Phys. Pol.* **B 27**, 1037 (1996).

[14] Djamel Ouerdane PhD Dissertation in Physics, University of Copenhagen (2003).

[15] J. Rafelsky, *Phys Rep.* **88**, 331 (1982).

[16] F. Antinori et al., *Nucl. Phys.* **A 698**, 118 (2002).

[17] NA49 Collaboration, V. Friese et al., arXiv:nucl-ex/0305017 (2003).

[18] M. Gaździcki and M.I. Gorenstein, *Acta Phys. Pol.* **B 30**, 2705 (1995).

[19] T. Matsui and H Satz, *Phys. Lett.* **B 178**, 416 (1986).

[20] F. Karsh, M.T. Mehr and H. Satz, *Z Phys.* **C 37**, 617 (1988).

[21] R. Hagedorn, *Phys. Rev. Lett.* **276**, 276 (1960).

[22] S. T. Butler and C.A. Pearson, *Phys. Rev.* **129**, 836 (1963).

[23] A. Schwarzschild and C. Zupancic, *Phys. Rev.* **129** 854 (1963).

[24] Allan G. Hansen PhD Dissertation in Physics, University of Copenhagen (2002).

[25] R.Bond, P.J. Johansen, S.E. Koonin and S. Garpman, *Phys. Lett.* **B 71**, 43 (1977).

[26] H. Sato and K. Yasaki, *Phys. Lett.* **B 98**, 153 (1981).

[27] A.Z. Mekjian, *Phys. Rev.* **C 17**, 1051 (1978).

[28] A.Z. Mekjian, *Nucl. Phys.* **A 312**, 491 (1978).

[29] I.Bearden et al., *Phys. Rev. Lett.* **78**, 2080 (1997).

[30] K.Kaimi et al., *Phys.* **C 75**, 619 (1997).

[31] J.Ollitrault, *Nucl. Phys.* **A 638**, 195 (1998).

[32] NA44 Collaboration, I. G. Bearden et al., *Phys. Rev. Lett.* **78**, 2080 (1997).

[33] David Sandberg Master's Thesis, Niels Bohr Institute, Copenhagen (2001).

[34] Polleri et al., *Phys. Lett.* **B 419**, 19 (1998).

[35] Ulrich Heinz and Rüdiger Scheibl, *Phys. Rev.* **C 59**, 1585 (1998).

[36] BRAHMS Collaboration, M. Adamczyk et al., *Nucl. Instr. Meth.* **A 499**, 437 (2003).

[37] E.S. Jakobsen Master's thesis, Niels Bohr Institute, Copenhagen (2001).

[38] Christian Holm Christensen Master's Thesis, University of Copenhagen (2002).

[39] H. Ito PhD thesis, Kansas University (2002).

[40] M. Chiu et al., *Phys. Rev. Lett.* **89**, 012302 (2002).

[41] C. Adler et al., *Nucl. Instr. Meth.* **A 470**, 488 (2001).

[42] P. Staszel, *Drift chambers for BRAHMS experiment at RICH facility*, Internal BRAHMS note.

[43] P. Staszel, *BRAHMS analysis notes 27, 29, 34 and 38*, technical report.

[44] BRAHMS collaboration, F. Videbæk, *Nuclear Phys.* **A 698**, 29c-38c (2002).

[45] R. Karabowicz Master's Thesis, University of Krakow, (2002).

[46] ROOT homepage: *http://root.cern.ch/*

[47] Claus O.E.Jørgensen Master's Thesis, Niels Bohr Institute, Copenhagen (2001).

[48] PHOBOS Collaboration, *Phys. Rev. Lett.* **85**, 3100 (2000).

[49] BRAHMS Conceptual Design Report, *http://www4.rcf.bnl.gov/brahms/WWW/cdr/tracking.ps*

[50] STAR collaboration, *Phys. Rev. Lett.* **89**, 9 (2002).

[51] PHENIX collaboration, *Phys. Rev. Lett.* **89**, 9 (2002).

[52] Eun Joo ABS and MS corrections: *http://pii3.brahms.bnl.gov/ ejkim/brahms/*

[53] I.G. Bearden et al., *Phys. Rev. Lett.* **B 85**, 13 (2000).

[54] S. Nagamia et al., *Phys. Rev.* **C 24**, 971 (1981).

[55] H. H. Gutbrod et al., *Phys. Rev. Lett.* **C 37**, 667 (1976).

[56] R.L. Auble et al., *Phys. Rev.* **C 28**, 1552 (1983).

[57] T.G.Armstrong et al., *Phys. Rev. Lett.* **C 85**, 13 (2000).

[58] A.G. Hansen et al., *Nucl. Phys.* **A 661**, 387c-390c (1999).

[59] C. Adler et al., *Phys. Rev. Lett.* **B 87**, 26 (2001).

[60] C. Struck for the STAR Collaboration (Proceeding Paper), *Anti–nuclei Production and Coalescence at RHIC* (2002).

[61] L.P.Csernai and J.I. Kapusta, *Phys. Rep.* **131**, 223 (1986).

[62] E941 Collaboration, *Phys. Rev.* **C 65**, 014904 (2001).

[63] J. D. Bjorken, *Phys. Rev.* **D 27**, 140 (1981).

[64] J. J. Stachel, *Nuclear Physics* **A 610**, 509c-522c (1996).

[65] PHENIX Collaboration, A. Bazilevsky *Nuclear Physics* **A 715**, 486c-489c (2003).

[66] Peter F. Kolb and U. Heinz, arXiv:nucl-th/0305084 (2003).

[67] Peter F. Kolb and Ralf Rapp, *Physical Rev.* c66, 017901 (2002).

[68] T Abbot et al., *Phys. Rev.* **C 50**, 1024 (1994).